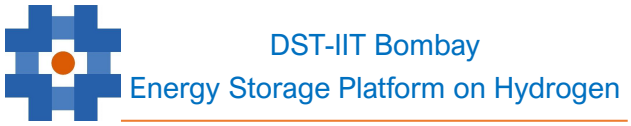

THÈSE DE DOCTORAT EN COTUTELLE

Effect of Adding the Intermetallic $LaNi_5$ and Rare Earth Elements La and Ce on the Hydrogen Storage Properties of TiFe Alloy

THÈSE PRÉSENTÉE À

L'UNIVERSITÉ DU QUÉBEC À TROIS-RIVIÈRES
ET
L'INDIAN INSTITUTE OF TECHNOLOGY BOMBAY

COMME EXIGENCE PARTIELLE DU
DOCTORAT EN SCIENCES DE L'ÉNERGIE ET DES MATÉRIAUX

PAR

MD MERAJ ALAM

AVRIL 2024

Université du Québec à Trois-Rivières

Service de la bibliothèque

Avertissement

L'auteur de ce mémoire, de cette thèse ou de cet essai a autorisé l'Université du Québec à Trois-Rivières à diffuser, à des fins non lucratives, une copie de son mémoire, de sa thèse ou de son essai.

Cette diffusion n'entraîne pas une renonciation de la part de l'auteur à ses droits de propriété intellectuelle, incluant le droit d'auteur, sur ce mémoire, cette thèse ou cet essai. Notamment, la reproduction ou la publication de la totalité ou d'une partie importante de ce mémoire, de cette thèse et de son essai requiert son autorisation.

- To my parents -

- To my brothers and sister -

- To all those who taught me even a single life lesson -

Department of Energy Science and Engineering
Indian Institute of Technology Bombay
Bombay, India-400076

Hydrogen Research Institute
Université du Québec à Trois-Rivières
Trois-Rivières (Québec) G9A 5H7, Canada

Thesis Approval

Certified that the thesis entitled **Effect of adding the intermetallic $LaNi_5$ and rare earth La and Ce on the hydrogen storage properties of TiFe alloy**, submitted by **Md Meraj Alam** to the **Indian Institute of Technology Bombay (India) and Université du Québec à Trois-Rivières (Canada)** has been accepted by the examiners. The student has successfully defended the thesis in the viva-voce examination held on April 30, 2024 and is worthy of consideration for the award of the degree of **Doctor of Philosophy** of the said Institutes.

Prof. Shobit Omar
(External Examiner)
Department of Material Science Engineering
Indian Institute of Technology Kanpur
Kanpur-208016, India.

Prof. Srinivas Seethamraju
(Internal Examiner)
Energy Science and Engineering
Indian Institute of Technology Bombay
Mumbai-400076, India.

Prof. Dasaka Murthy
(Chairperson)
Department of Civil Engineering
Indian Institute of Technology Bombay
Mumbai-400076, India.

Prof. Pratibha Sharma
(Supervisor)
Energy Science and Engineering
Indian Institute of Technology Bombay
Mumbai-400076, India.

Date:
Place: IIT Bombay

Prof. Jacques Huot
(Co-supervisor)
Hydrogen Research Institute
Université du Québec à Trois-Rivières
Trois-Rivières (Québec) G9A 5H7, Canada.
Date:
Place:

Department of Energy Science and Engineering
Indian Institute of Technology Bombay
Bombay, India-400076

Hydrogen Research Institute
Université du Québec à Trois-Rivières
Trois-Rivières (Québec) G9A 5H7, Canada

Certificate of originality

This is to certify that this thesis entitled **Effect of adding the intermetallic $LaNi_5$ and rare earth La and Ce on the hydrogen storage properties of TiFe alloy** submitted by **Md Meraj Alam**, to the Indian Institute of Technology Bombay and Université du Québec à Trois-Rivières, is a record of bona fide research work carried out under our supervisions.

Prof. Pratibha Sharma
(Supervisor)
Department of Energy Science and Engineering
Indian Institute of Technology Bombay
India - 400076.
Date:
Place: IIT Bombay

Prof. Jacques Huot
(Co-supervisor)
Hydrogen Research Institute
Université du Québec à Trois-Rivières
Trois-Rivières (Québec) G9A 5H7, Canada.
Date:
Place:

Abstract

Climate change necessitates the utilization of renewable energies to meet the escalating global energy demand. Hydrogen has emerged as a potential energy carrier owing to its lightweight and high calorific value. However, the challenge lies in the storage and transportation of hydrogen. While gaseous and liquid-state hydrogen storage methods are well-established, they require substantial energy input and specialized containment vessels.

Solid-state hydrogen storage offers a safer and more compact approach to store hydrogen. Metal hydrides (MHs) can store hydrogen reversibly within a 25 to 350 °C temperature range under pressures typically within 100 bar. The binary alloy TiFe stands out as a cost-effective candidate capable of storing hydrogen reversibly under mild pressure conditions at room temperature (RT). However, the first hydrogenation of the alloy, often referred to as activation, is complicated, rendering it prohibitively expensive for many applications. The first description of an effective activation process of TiFe alloy was suggested in Reilly and Wiswall's pioneering work [1]. It requires heating the alloy to more than 400 °C and keeping it at that temperature for an hour, either under a vacuum or at low hydrogen pressure, then cooling it to room temperature and applying a high hydrogen pressure of about 65 bar. If the alloy does not activate within 15 minutes, it is necessary to repeat the process a few times until the alloy activates. Facilitating activation in TiFe alloy by doping, substituting, or adding transition elements have been widely explored. Researchers have also tried mechanical deformation techniques to overcome the challenges of activation. A handful of studies on the TiFe alloy with rare-earth metals as additives has been reported in the literature.

This project aims at providing a detailed insight into the effect of adding the intermetallic $LaNi_5$ and rare earth elements La and Ce on the hydrogen storage properties of TiFe alloy. The choice of La and Ce as rare earth elements was based on their inability to form intermetallic compounds with Ti, Fe, and TiFe, thus, suggesting the likelihood of forming a composite. A composite of $LaNi_5$ and TiFe could prove beneficial not just for activation but also for desorption, thanks to the

ease with which $LaNi_5$ can be activated and its ability to form a reversible hydride at RT. In previous studies, it was found that a minimum of 4 at% Zr was needed for rapid initial hydrogenation in TiFe alloy. To ensure we meet this threshold in our study, we introduced 16 wt% of additives (equivalent to 10 at% $LaNi_5$ and 6.6 at% La or Ce). Since this research aims to investigate the influence of additives on the initial hydrogenation, the primary objective was not to optimize the composition but to determine the presence or absence of an effect.

The objective is to provide a gateway for hydrogen to reach the main matrix TiFe by adding a secondary phase/region made of additives. Thus eliminating the rigorous activation procedure. The present study differs from the earlier investigations as the alloy synthesis was carried out primarily by exploring a new strategy of combining ball milling and arc melting. Firstly, pure TiFe alloy was synthesized by two techniques, namely- arc melting (casting) and ball milling (mechanical alloying, MA). In the next step, additives were incorporated into the pre-synthesized TiFe alloy with short duration milling in order to maintain the composite nature of the materials. The TiFe alloy with additive has also been synthesized by MA the elemental powders mixtures. In total TiFe with additives have been synthesized by three different ways:

- Incorporation of additives La, Ce, or $LaNi_5$ to as-cast TiFe via mechanical milling (MM).
- Incorporation of additives La, Ce, or $LaNi_5$ via MM but to MA TiFe alloy.
- Samples prepared by mixing elemental powders Ti, Fe, and La followed by MA. Similarly, Ti, Fe, and Ce mixed powder underwent MA.

The MA TiFe showed very sluggish kinetics, reaching just 0.23 wt% in 24 hours and still absorbing beyond that. The cast TiFe synthesized by arc melting did not activate under the present experimental conditions of RT under 20 bars hydrogen pressure. However, the same alloy, when mechanically milled (MM-cast TiFe), gets hydrogenated with an absorption capacity of 1.0 wt% in 3 hours. The first hydrogenation of the composites TiFe with additives (La, Ce, $LaNi_5$) were remarkably fast reaching between 1.0 to 1.35 wt% within an hour except two samples which showed slower kinetics.

The synthesis of the alloy played a pivotal role in determining the microstructure and had significant influence over the impact of additives in determining the hydrogenation properties of the TiFe alloy. The incorporation of additives into MA TiFe, through MM, has proven to be less favorable due to its vulnerability to oxidation. Incorporating additives via MM into cast TiFe turned out to be a

promising synthesis method and can be used especially when the melting point of the additives is much lower compared to the main alloy.

Keywords: Hydrogen storage, Metal hydrides, TiFe alloy, Rare earth elements, First hydrogenation, Activation, Mechanical alloying, Mechanical milling.

Résumé

Le changement climatique nécessite l'utilisation d'énergies renouvelables pour répondre à la demande énergétique mondiale croissante. L'hydrogène est devenu un vecteur énergétique potentiel pour les applications fixes et mobiles grâce à sa légèreté et à son haut pouvoir calorifique. De plus, l'hydrogène génère uniquement de l'eau comme sous-produit lors de la libération d'énergie. Cependant, le défi réside dans le stockage et le transport de l'hydrogène. Bien que les méthodes de stockage de l'hydrogène gazeux et liquide soient bien établies, ils nécessitent un apport énergétique important et des réservoirs spécialisées.

Le stockage de l'hydrogène à l'état solide offre une approche plus sûre et plus compacte pour stocker l'hydrogène. Les hydrures métalliques (HM) peuvent stocker l'hydrogène de manière réversible dans une plage de températures de 25 à 350 °C sous des pressions généralement de quelques dizaines de bars. L'alliage binaire TiFe se présente comme un candidat rentable, capable de stocker l'hydrogène de manière réversible sous basse pression à température ambiante. Cependant, la première hydrogénation de l'alliage, souvent appelée activation, est compliquée. Cette complication est principalement attribuée à l'oxydation de l'alliage lors de la synthèse et de la manipulation. Habituellement, un chauffage répété à plus de 400 °C sous une pression de plus de 60 bars d'hydrogène est nécessaire pour activer l'alliage, ce qui le rend d'un coût prohibitif pour de nombreuses applications. Faciliter l'activation dans l'alliage TiFe par dopage, substitution ou ajout d'éléments de transition a également été largement exploré. Les chercheurs ont également essayé des techniques de déformation mécanique pour surmonter les défis d'activation. La littérature sur les propriétés de stockage de l'hydrogène de l'alliage TiFe additionné d'éléments de terres rares est limitée. Ainsi, une analyse plus rigoureuse du système TiFe ajouté aux éléments de terres rares est importante.

Ce projet vise à fournir un aperçu détaillé de l'effet de l'ajout des éléments intermétalliques $LaNi_5$ et des terres rares La et Ce sur les propriétés de stockage d'hydrogène de l'alliage TiFe. Le choix de La et Ce comme éléments des terres

rares était basé sur leur incapacité à former des composés intermétalliques avec Ti, Fe et TiFe, suggérant ainsi la probabilité de former un composite. De plus, La et Ce font partie des métaux des terres rares les moins chers, ce qui a motivé notre attention sur l'étude de ces éléments. Cependant, La forme un hydrure stable, donc un composé de La avec Ni, c'est-à-dire $LaNi_5$, a également été sélectionné comme additif en raison de sa facilité d'activation et de formation d'hydrure réversible à température ambiante. Ainsi, on s'attend à ce qu'un composite de TiFe et de $LaNi_5$ aide non seulement à l'activation mais également à la désorption. Dans des études précédentes, il a été constaté qu'un minimum de 4% massique de Zr était nécessaire pour une hydrogénation initiale rapide dans l'alliage TiFe. Pour garantir que nous respectons ce seuil dans notre étude, nous avons introduit 16% massique en poids d'additifs (équivalent à 10% massique $LaNi_5$ et 6,6% massique La ou Ce). Puisque cette recherche vise à étudier l'influence des additifs sur l'hydrogénation initiale, l'objectif premier n'était pas d'optimiser la composition mais de déterminer la présence ou l'absence d'un effet.

Notre objectif est de fournir une passerelle pour que l'hydrogène atteigne la matrice principale TiFe en ajoutant un secondaire phase/région composée d'additifs pour faciliter l'activation et pour obtenir une meilleure compréhension de l'interaction métal-hydrogène. Éliminant ainsi la procédure d'activation rigoureuse. La présente étude diffère des recherches antérieures dans la mesure où la synthèse de l'alliage a été réalisée principalement en explorant les manières possibles de combiner le broyage mécanique (BM) et la fusion à l'arc. Les alliages synthétisés ont été étudiés pour leurs propriétés d'hydrogénation, de microstructure et de structure cristalline à température ambiante sans activation préalable, comme l'exposition de l'alliage à une température ou une pression élevée. Il a été constaté que l'activation de l'alliage TiFe avec des additifs s'est remarquablement améliorée.

Nous avons noté que le processus de synthèse influençait de manière significative les propriétés de l'alliage TiFe par rapport à l'impact des additifs. L'incorporation d'additifs dans le TiFe mécaniquement allié (MA), par broyage mécanique (BM), s'est avérée moins favorable en raison de sa vulnérabilité à l'oxydation. En revanche, l'incorporation d'additifs par broyage mécanique (BM) dans le TiFe coulé est prometteuse en tant que méthode de synthèse, notamment lorsque le point de fusion des additifs est inférieur à celui de l'alliage principal.

Mots clés: Stockage d'hydrogène, Alliage TiFe, Éléments de terres rares, Première hydrogénation, Activation, Alliage mécanique, Broyage mécanique.

Declaration

I hereby affirm that:

a. The content presented in this thesis is original and has been carried out under the guidance of my supervisors;

b. This work has not been submitted to any other institution to obtain any other degree or diploma, apart from the two institutions mentioned in this thesis;

c. I have adhered to the ethical norms and guidelines while writing this thesis;

d. Whenever I have employed materials (including data, models, figures, and text) from external sources, I have given appropriate credit by citing them within the thesis text and providing comprehensive details in the reference section.

Md Meraj Alam
Roll No.- 164170004 (IITB)
Permanent code- ALAM08089100 (UQTR)

Date:
Place: IIT Bombay

Acknowledgment

While pursuing my PhD, I had the privilege of collaborating with inspiring individuals who collectively created a productive environment. I extend my gratitude to all those who contributed to fostering this stimulating atmosphere, crucial for the successful completion of my project over the years.

I extend my deepest gratitude to Prof. Pratibha Sharma and Prof. Jacques Huot for the opportunity to join their labs at IIT Bombay (India) and Université du Québec Trois-Rivières (UQTR, Canada), delving into the dynamic field of energy and material sciences. Being part of a high-energy, competitive division under their guidance was a remarkable experience. Thank you, dear supervisors, for your encouragement, creative vision, and unwavering support throughout my research. I have gained insights into planning and conducting systematic research and effective collaboration.

I am extremely thankful to Prof. Rangan Banerjee and Prof. Suneet Singh, former and current Head of the Department of Energy Science and Engineering at IIT Bombay, and Prof. Richard Chahine, and Prof. Pierre Benard, former and current Director of the Hydrogen Research Institute (IRH) and doctoral program director Phuong Nguyen-Tri at UQTR. I would like this opportunity to thank former director IIT Bombay, Prof. Devang V Khakhar and Catherine Parissier, VP of Academics and Training at UQTR for the cotutelle agreement and the acceptance of my cotutelle PhD candidacy, facilitating my student exchange program for the joint doctoral pursuit. Special gratitude to my research progress committee (RPC) members at IIT Bombay, Prof. Srinivas Seethamraju and Prof. P. C. Ghosh, for their useful recommendations and motivation during annual progress seminars (APS). Your valuable suggestions and continuous feedback have been instrumental in the successful execution of my research. Acknowledgment also goes to my jury members, Prof. Jacques Goyette and Prof. Jean Hamelin, for their insightful suggestions and valuable inputs during the doctoral examination at UQTR Canada.

I extend my thanks to the former and current members of the DST IIT Bombay energy storage laboratory. Gratitude is extended to Dr. Devendra, Dr. Binayak, Dr. Mahvash, Dr. Meenakshi, Dr. Animesh, Dr. Vineet, Dr. Saurabh, Dr. Dharmendra, Dr. Subhasis, Dr. Tijin, Ms. Ankita, Mr. Ravi, Mr. Nandlal, and Mr. Vishnulal for their insightful discussions. Special appreciation goes to

Dr. Dharmendra and Ms. Ankita for their extensive discussions and collaborative efforts in understanding the field. My best wishes to the new researchers, Mr. Chandramani, Mr. Abhijeet Bihari, Mr. Mohit, Mr. Datta, Mr. Kapil, Ms. Sravani, Ms. Trashna, Mr. Vishnulal K. S, and Ms. Shruthi for their PhD projects. It was a pleasure getting to know the master's students, Mr. Sahil, Mr. Abhijeet, and Ms. Ritika. Great thanks to Prof. Pratibha Sharma and her better half Prof. Manvendra and their nice kids Ms. Kopal and Ms. Laksha.

Special thanks to my colleagues, friends, and seniors, Prof. Salman, Dr. Irfan, Mr. Bilal, Dr. Moiz Khan, Dr. Shakeel, Dr. Haseen, Dr. Danish Equbal, Mr. Kalamuddin, Mr. Harshal, Ms. Shayeri, Ms. Roja, Mr. Pradeep, Mr. Sagar, Mr. Shadab, Mr. Ayyaz, Mr. Sharique, Mr. Mir, Dr. Monis, Dr. Imran, Dr. Shihab, Dr. Vinamra, Mr. Chitresh, Mr. Ashfaq, Dr. Zulfiqar, Mr. Rehan, Mr. Ramiz, Mr. Qasim, Mr. Ahmad, and Mr. Khursheed for their encouragement and creating a friendly environment during my time at IIT Bombay.

Gratitude to my IRH (Hydrogen Research Institute) lab mates, including Dr. Amol, Dr. Salma, Dr. Sakine, Dr. Renato, Dr. Elena, Dr. Vola Raza, Dr. Catherine, Ms. Francia, Ms. Chourouk, Ms. Natalia, Ms. Veronica, Ms. Jacqueline, Mr. Babak, Mr. Vinícius. Special acknowledgment to Dr. Abhishek K. Patel, Dr. JingJing Liu, Dr. Joydev Manna, Ms. Priya Gatti, Dr. Sabrine Boulila, Dr. Noor Dissem, Dr. Hema S. Ilamathi, Dr. Viney Dixit, Mr. Marc-Antoine Page, Dr. Saif Rehman, Dr. Madina, Dr. Sanil, Dr. Midhun, Dr. Aneeshma Peter, Dr. Shweta, Dr. Kiran, Ms. Amita, and Ms. Priyanka Bhatt for making Canada feel like home. The cherished moments we spent together will be remembered.

I acknowledge the Department of Science and Technology, Ministry of Education, Government of India for their financial support through the Ph.D. Teaching Assistantship during my tenure at IIT Bombay. Special thanks to the Canadian Queen Elizabeth II Diamond Jubilee Fellowship (QES) for their financial support during my stay in Canada. I would like to extend sincere thanks to Ms. Genevieve Cote and Ms. Catarina for their assistance during my enrollment in the QES program at UQTR and to Mr. Sébastien Gauthier, Ms. Christine, and Ms. Patricia for thir support thereafter. My special appreciation goes to our lab managers, Ms. Anik, Ms. Marieve, Ms. Agnes from UQTR and Mr. Rahul from IIT Bombay. Thanks to all the administrative staff from IIT Bombay and UQTR for their help.

Heartfelt thanks to my uncle and aunt, Mr. Md Muzaffar Alam, and Mrs. Kehkashan Anjum, and their delightful children, Saadan Anjum and Haiqa Anjum. I am profoundly grateful for the unwavering moral support from my parents, Mr. Md Moiz Uddin, and Mrs. Bibi Shabnam Ara, and for their boundless love. Finally, I would like to show my gratitude to my dear brothers Prof. Meyarul Islam and Md Modassir Alam, my younger sister Sania Shabnam, and all my cousins, especially Md Hasnain and Md Farhaz Alam. This thesis is dedicated with special affection to my parents and siblings.

Contents

Abbreviations and symbols

RT	Room temperature
HT	High temperature
MA	Mechanical alloying
MM	Mechanical milling
BM	Ball milling
AM	Arc melting
BCC	Body centred cubic
FCC	Face centred cubic
HCP	Hexagonal closed packing
LHV	Lower heating value
HHV	High heating value
SPL	Surface passive layer
XRD	X-ray diffraction
SEM	Scanning electron microscopy
SE	Secondary electron
BSE	Back-scattered electron
TEM	Transmission electron microscopy
EDX, EDS	Energy dispersive X-ray spectroscopy
HPT	High pressure torsion
CR	Cold rolling
GR	Groove rolling
PCT, PCI	Pressure composition isotherm
GUI	Graphics user interface
arb. u.	Arbitrary unit
NTP	Normal temperature pressure
a, abs	Absorption
d, des	Desorption
MH	Metal hydride

Mm	Mischmetal
BPR	Ball-to-powder weight ratio
AV	Automatic valve
MV	Manual valve
IITB	Indian Institute of Technology Bombay
UQTR	Université du Québec Trois-Rivières
wt%	Weight percentage
at%	Atomic percent
α-La	Room temperature lanthanum phase
β-La	High temperature lanthanum phase
α-phase	Solid-solution hydride phase
β-phase	Mono-hydride phase
a, c	Lattice parameters
H%	Gravimetric hydrogen capacity
H_2	Molecular hydrogen, hydrogen gas
H	Atomic hydrogen
psi	Pounds per square inch
P_{eq}	Equilibrium pressure, plateau pressure
H/M	No. of hydrogen atom per metal atom
ΔH	Enthalpy change
ΔS	Entropy change
P	Pressure
V	Volume
T	Temperature
R	Universal gas constant
n	Number of moles
h	hour
g	gram
λ	Wavelength of X-ray radiation
d	Inter-planar distance
θ	Bragg angle
B	Second order Virial coefficient
nm	nanometer
Å	Angstrom

List of Figures

List of Tables

CHAPTER 1

Introduction

This chapter emphasizes the need for a hydrogen-based economy over a fossil fuel economy. To achieve such a global energy system, different challenges must be addressed. In this context, hydrogen storage poses a critical scientific and engineering challenge. Various available hydrogen storage techniques have been reviewed and presented with advantages and disadvantages to assess the challenges associated with hydrogen storage. The primary focus is on the storage techniques for hydrogen in the solid state, particularly in the form of metal hydrides. Motivation for the research and objectives have been clearly established. Different applications of the metal hydrides beyond hydrogen storage are also briefly presented. Finally, the formulation of the thesis chapters and their organization is presented.

1.1 Hydrogen as an energy carrier

Energy in its various forms has been an integral part of human civilization. Daily activities like lighting, cooking, running machines, and transportation depend on energy. The total energy requirement continuously increases due to population growth and economic development. According to International Energy Agency, fossil fuels account for 80% of the energy demand globally [2]. Since fossil fuels are limited and our consumption rate is high, it will cater to our needs for a limited period. Moreover, fossil fuels are the leading cause of environmental degradation and a significant contributor to global warming. Hence, global warming, climate change, carbon neutrality, and energy security are the subject of a global debate on energy and its effect on the climate. Many developing countries have formulated net zero emissions by 2050. Conversely, India has set their carbon neutrality goal

by 2070. Therefore, sustainable, clean, cost-effective alternative energy sources are becoming a major concern. Hence, alternative energy solutions are currently the subject of much research and investigation. Considerable research has lately been carried out on energy sources like wind, solar, geothermal, biomass, tidal, nuclear energy, etc. However, these alternative energy solutions are season and location dependent. Nevertheless, they are explored as well.

Hydrogen energy vector has received particular attention. The utilization of hydrogen as a fuel offers distinct advantages compared to conventional fuels, as illustrated in Table 1.1, where a technical comparison of fuel properties is presented. Hydrogen stands out with the highest energy-to-weight ratio (heating value) among fuels, despite its relatively low energy-to-volume ratio. With a higher heating value (HHV) of 141.78 MJ/kg of H_2 and a lower heating value of 120 MJ/kg of H_2, hydrogen demonstrates remarkable energetic characteristics. Properties outlined in the latter part of Table 1.1 emphasize safety considerations. Rapid diffusivity in air, elevated upper flammability limit, and low ignition energy requirement, making hydrogen a unique and advantageous fuel from both safety and utilization perspectives. For this reason, a hydrogen-based energy system is an advantageous option for providing high-quality energy solutions; besides, it is clean as it produces water vapor on combustion and is non-toxic.

Table 1.1: Properties of hydrogen and other conventional fuels [3].

Properties	**Hydrogen**	**Petroleum**	**Methanol**	**Methane**	**Propane**
Boiling point (K)	20.3	350-400	337	111.7	230.8
Liquid density (kg/m^3 @NTP)	71	702	797	425	507
Gas density (kg/m^3 @NTP)	0.08	4.68	-	0.66	1.87
Heat of vaporization (kJ/kg)	444	302	1168	577	388
Higher heating value, HHV (MJ/kg)	141.6	46.7	22.7	55.5	50.3
Lower heating value, LHV (MJ/kg)	120.0	44.38	18.0	50.0	45.6
LHV (liquid) (MJ/m^3)	8960	31170	16020	21250	23520
Diffusivity in air (cm^2/s)	0.63	0.08	0.16	0.20	0.10
Lower flammability limit in air (vol%)	4	1	7	5	2
Upper flammability limit in air (vol%)	75	6	36	15	10
Ignition temperature in air (°C)	585	222	385	534	466
Ignition energy (MJ)	0.02	0.25	-	0.30	0.25
Flame velocity (cm/s)	270	30	-	34	38

Despite being the most abundant element found in the universe, molecular hydrogen is not easily accessible on Earth since the majority of it is bonded to the oxygen in the water. Hydrogen is widely utilized in the industry as a crucial component in manufacturing ammonia, which is used in fertilizer, with annual output nearing 75 million tons in 2018 [4]. The majority of industrial H_2 is produced through steam reforming of methane, and the chemical reaction is illustrated as follows:

$$CH_4 + 2H_2O(g) \longrightarrow CO_2(g) + 4H_2(g) \tag{1.1}$$

The CO_2 emissions are quite significant because of the threat that global warming poses to today's society. Alternatively, water can be split (through electrolysis) to produce clean H_2 using the following equation:

$$2H_2O(l) \longrightarrow 2H_2(g) + O_2(g) \tag{1.2}$$

If the electricity utilized to power the reaction originates from sources of renewable energy like wind or solar, it is designated as clean H_2. Using clean H_2 as a low carbon fuel to phase out fossil fuels gradually is known as hydrogen economy, a concept introduced in 1970 [5]. Hydrogen is unique compared to other energy storage technologies because it can be used for almost all facets of the contemporary energy system, including transportation, heating, and large-scale, long-term grid storage [6, 7]. Indeed, hydrogen as an energy carrier has been proposed as a suitable route and a promising way to solve global energy and environmental problems. However, the primary challenge lies in the storage and transportation of hydrogen, especially for onboard applications.

1.2 Ways of storing hydrogen

Hydrogen storage refers to the methods and techniques used to store hydrogen gas for transportation or other uses. There are several ways to store hydrogen, including as a gas, a liquid, or in chemical compounds such as metal hydrides or carbon nanotubes [8]. The most common method for hydrogen storage is as a compressed gas in high-pressure tanks. Still, liquid hydrogen storage and storage in solid hosts are also being researched as potential alternatives. Classification of different hydrogen storage techniques is illustrated in Fig. 1.1.

1.2.1 Pressurized storage

Pressurized gaseous hydrogen storage is the most common method for storing hydrogen fuel for transportation. Hydrogen is stored in high-pressure tanks at pressures ranging from 35 to 700 bar (500 to 10,000 psi) in this method. There are four types of commercially available tanks—designated as type I, II, III, and IV [9]. Type I tanks are made from steel and can withstand pressures ranging from

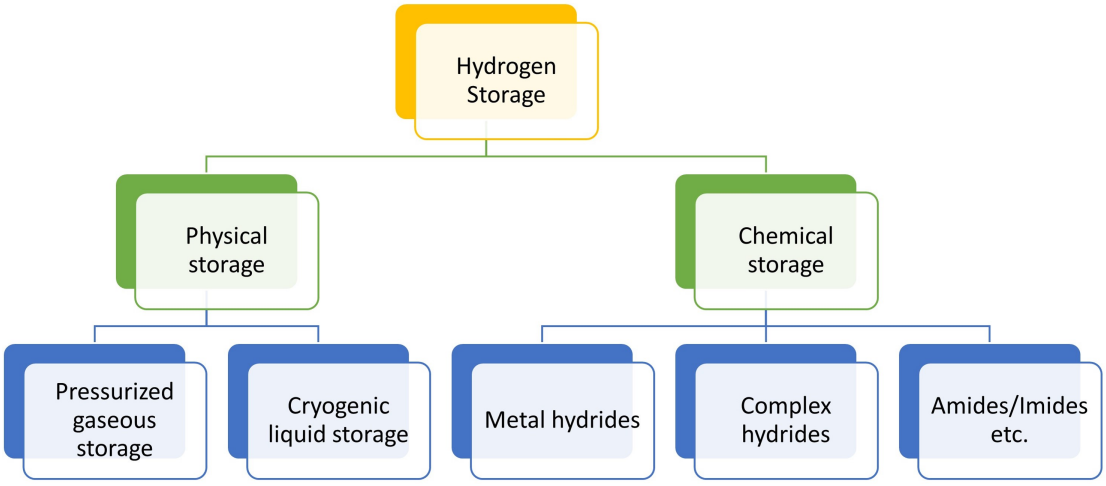

Figure 1.1: Classification of hydrogen storage techniques

200-300 bar, but they are quite heavy. In the rest steel is replaced by composite materials and stability is provided by carbon fibre meshing that can withstand pressures up to 700 bar and are lightweight.

The main advantage of pressurized gaseous storage is that it is relatively simple and efficient. The main disadvantage is that pressurized storage requires a large volume for storing a given amount of hydrogen as the density of hydrogen gas is 0.08 kg/m^3 at NTP ($\approx$ 23 kg/m^3 at 350 bar and $\approx$ 40 kg/m^3 at 700 bar). Moreover, the high-strength alloys or composite materials required for manufacturing type III and IV vessels, and the associated cost of these vessels tend to be expensive. Additionally, ensuring the integrity of these cylinders over time and throughout various operating conditions requires rigorous testing, maintenance, and safety measures to meet stringent safety standards while maintaining durability.

1.2.2 Cryogenic liquid storage

Cryogenic liquid storage of hydrogen refers to storing hydrogen as a liquid at very low temperatures, typically below -253 °C. At these temperatures, hydrogen is in a liquid state and can be stored in special insulated containers known as Dewar tanks. One of the main advantages of cryogenic liquid storage is that it has a much higher volumetric density ($\approx$ 70 kg H_2/m^3). This makes it more practical for transportation as it takes up less space. Also, liquid hydrogen is easily handled and can be transported through tankers using ISO containers.

The main disadvantage of cryogenic liquid storage is that it requires significant energy to cool the hydrogen to its liquid state and maintain it at that temperature. About 20-30% of the total energy content of the stored hydrogen is needed for its liquefaction. The storage tanks and transport containers must be well insulated

to prevent the hydrogen from evaporating. Despite effective insulation, liquid hydrogen gradually absorbs heat from the environment, leading to its conversion into gas over time. To mitigate pressure buildup, it becomes essential to release this gas. Boil-off losses are estimated at around 4% per day for tanks with a storage volume of 50 m^3, though larger tanks exhibit small losses (0.2% for 100 m^3 tank) [10]. Therefore, insulation and cooling systems add to the overall cost and complexity of the storage system. Cryogenic liquid storage in Dewar tanks is mainly used in industrial and scientific applications where the cost of hydrogen is of minimal concern and the hydrogen is utilized within a short time like rocket propulsion.

Other hydrogen storage methods, like liquid organic hydrogen carriers (LOHC) and storage in solid form, are being researched as potential alternatives to pressurized gaseous storage to improve the volumetric and gravimetric density of hydrogen storage.

1.2.3 Solid state storage

Solid-state hydrogen storage refers to storing hydrogen in a solid form, typically in chemical compounds such as metal hydrides. The main advantages of storing hydrogen in a metal hydride are the high hydrogen volumetric densities (sometimes higher than the liquid hydrogen storage density of 70 kg H_2/m^3) and the possibility to absorb and desorb hydrogen with a slight change of hydrogen pressure [10]. Solid-state storage is relatively safe and stable, as the hydrogen is stored in a chemical form that is less likely to leak or explode.

The main disadvantage of solid-state storage is that absorbing and releasing hydrogen from the storage material can be slow and require a significant amount of energy. The energy required during desorption is dependent on the enthalpy of de-hydriding of that particular metal or alloy. For practical purposes, MHs having an enthalpy change in the range of 15-24 kJ/(molH) is favorable, which translates to the requirement of 10-15% of the total stored energy [9]. However, the same amount of energy is released during hydrogen absorption, which to some extent can be stored and utilized during desorption. Thus, it is possible to reduce the energy requirement. Additionally, the storage materials can be expensive and have limited lifetimes.

Metal hydrides are the most studied and promising solid-state storage materials; they have high hydrogen volumetric densities and are relatively safe and stable. Research on solid-state storage is ongoing, and the technology still needs to be mature.

1.3 The metal hydrogen systems

The metal reacts with hydrogen under a certain temperature and pressure to form a metal hydride. The reaction between metal and hydrogen is a complex heterogeneous gas-solid reaction. The overall reaction can be expressed in a simplified form:

$$\mathrm{M(s)} + \frac{\mathrm{n}}{2}\mathrm{E(g)} \rightleftharpoons \mathrm{ME_n(s)} + \Delta\mathrm{Q} \tag{1.3}$$

where M denotes metal, E denotes hydrogen isotopes (H, D, and T), and ΔQ is the heat of the reaction. The forward reaction, i.e., metal hydride formation, is exothermic, whereas the backward reaction, i.e., the de-hydriding reaction, is endothermic. However, the reaction takes several steps, each with its own physical significance. The metal-hydrogen reaction takes place through a physisorption followed by a dissociative chemisorption. After the hydrogen atom is chemisorbed on the metal surface, it diffuses to the bulk forming a hydride phase. In 1932, Lennard-Jones proposed a one-dimensional potential energy diagram for the dissociative adsorption of a hydrogen molecule on the metal surface shown in Fig. 1.2 [11]. The curve leveled as II in the figures represents the potential energy of a hydrogen molecule as a function of distance from the surface. The zero reference is taken when the molecule is at an infinite distance from the surface, as there is no interaction between the metal and hydrogen. The curve leveled as I is the potential energy curve as a function of distance for a hydrogen atom. It can be seen from Fig. 1.2 that the hydrogen atom possesses a finite amount of potential energy even at an infinite distance from the surface. The potential energy difference between the H_2 molecule and H-atom is equal to the dissociation energy of the hydrogen molecule (436 kJ/mol-H_2) [12]. As the H_2 molecule comes closer to the metal surface, there is a small potential well representing the physisorption of the molecule on the surface. This is caused by the van der Walls force of attraction and is characterized by a low heat of adsorption in the 0-40 kJ/mole H_2 range. This leads to a physisorbed state of the hydrogen at around one molecular hydrogen radius distance (approx 0.2 nm) from the metal surface.

The potential energy of the molecule increases as it moves closer to the surface due to repulsion. Eventually, the potential energy of the H_2 molecule and that of the H-atom will intersect. It is the activation barrier between the physisorbed and chemisorbed states. The hydrogen molecule must overcome the activation barrier to dissociate the H-H bond and form the metal-hydrogen bond.

Consider the intersection at a potential energy greater than zero compared to gas phase H_2 as in Fig. 1.2 (a). The height of the dissociation determines

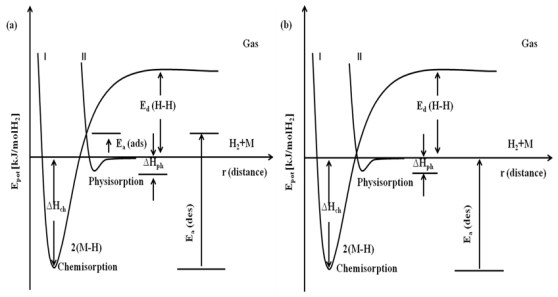

Figure 1.2: Schematics of Lennard-Jones potential energy diagram for metal hydrogen interaction (a) non-activated adsorption, (b) activated adsorption [13].

the activation barrier, and surface elements determine how high the activation barrier is. Only those H_2 molecules whose energy exceeds the activation barrier can dissociate in this case. This is considered non-activated.

Fig. 1.2 (b) shows dissociation is activated when the intersection occurs close to zero potential energy. Upon dissociation, the hydrogen atoms find a potential energy minimum corresponding to the hydrogen atoms bound to the metal surface (chemisorption). The relative strength between H-H and M-H bonds determines the nature of chemisorption. The process is said to be exothermic if the H-M bond is stronger than the H-H bond and endothermic if the H-H bond is more potent. Through the chemisorption process, the hydrogen atoms penetrate the first few metal atomic layers into the subsurface; this mechanism is adsorption, and then hydrogen diffuses into the bulk of the metal.

1.3.1 Thermodynamics of metal hydrides

The state of a simple thermodynamic system in equilibrium can be defined by two independent, intensive properties known as state-postulate. In this context, the metal-hydrogen system has an associated pressure-composition-temperature (PCT) relationship, their most important technical characteristic. A PCT diagram summarizes these properties conveniently, of which an idealized version is presented in Fig. 1.3 [14]. It comprises a series of isotherms that show how the equilibrium pressure (P_{eq}) varies with hydrogen concentration (H/M) in the solid. The PCT comprises three distinct regions and is detailed in the following paragraphs.

Hydrogen dissolves in the metal, causing the isotherm to ascend steeply initially. This single-phase solid-solution region is the α phase. It is ideal that an isotherm in a solid-phase region obeys Sievert's law, which states that hydrogen concentration in the solid phase is proportional to the square root of the equilibrium pressure:

$$H_{solid} = KP^{(1/2)} \tag{1.4}$$

when the pressure (or chemical potential) of H_2 increases, the hydrogen concentration increases until the condensation transformation occurs, causing nucleation and growth of hydride at higher concentrations known as β phase. The phase transition occurs in the metal lattice at the expense of the α phase and is characterized by a plateau in the isotherm. Ideally, a flat plateau with hydrogen absorption without much change in pressure should be observed because the degree of freedom in this region is unity. The α and β phases co-exist in this region. At the terminal point of the α and β co-existing region, the isotherm again rises steeply with the increasing hydrogen pressure, marking the conversion of co-existing two-phase region to an entire single β phase region. An alloy or metal can exhibit multiple plateaux if it can form more than one distinct hydride phase. Generally, the heat of the solution depends on the concentration of hydrogen. An expression for infinite dilution is presented in equation 1.4. The situation of high concentration will now be illustrated (α and β co-existing region in Fig. 1.3). According to the phase rule, the pressure should remain invariant below the critical temperature in this region. The Van't Hoff law provides the equilibrium pressure (P_{eq}) at the α to β phase transition region and is given by:

$$\ln(P_{eq}/P_o) = (-\Delta H/RT) + (\Delta S/R) \tag{1.5}$$

where P_{eq} = Plateau pressure or equilibrium pressure, P_o = Atmospheric pressure, ΔH = Enthalpy of formation/dissociation, ΔS = Entropy of formation/dissociation, T = Temperature, R = Universal gas constant, $(\Delta H/R)$ = Slope of Van't Hoff plot, and $(\Delta S/R)$ = Intercept of Van't Hoff plot.

A metal hydride must first satisfy the thermodynamic requirements of enthalpy and entropy of formation/dissociation for its operating temperature and hydrogen pressure to be suitable for practical applications. In-depth treatment of the thermodynamics of metal-hydrogen systems can be found in the literature [14, 15, 16, 17, 18, 19, 20, 21].

First-principles calculations for ΔH still need to be improved for ternary alloys. However, it is possible to apply semi-empirical models to specific systems to gain helpful insight into the formation of hydrides. Miedema's model and the semi-empirical band structure model are two of the most common models.

Let us take the AB alloy; hydrogenation will generally not result in the breakdown; instead, it will produce a ternary hydride as a reaction product.

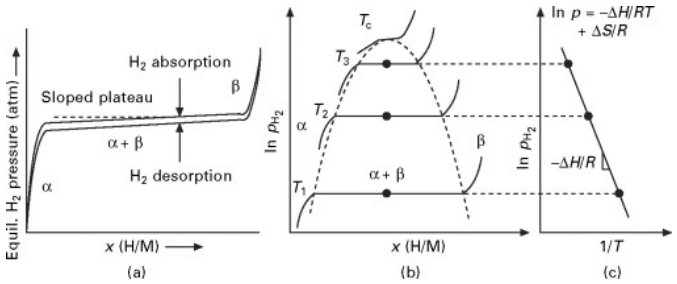

Figure 1.3: An ideal PCT of a metal-hydrogen system and corresponding Van't Hoff plot [14].

$$AB_n + xH_2 = AB_nH_{2x} \tag{1.6}$$

The semi-empirical relationship between the heat of the formation of a ternary hydride can be expressed as follows:

$$\Delta H(AB_nH_{2x}) = \Delta H(AH_x) + \Delta H(B_nH_x) - \Delta H(AB_n) \tag{1.7}$$

The relation 1.7 is called Miedema's rule of reversed stability. Thus, Miedema's rule is less stable alloys form more stable hydrides. Details can be found in the references [18, 22].

1.3.2 Activation (First hydrogenation)

Depending on the formation process of a particular metal or alloy, the external solid surfaces are usually covered with oxides of varying thicknesses, corrosion and hydroxyl layers, collectively termed the surface passivation layer (SPL) [17]. The SPL acts as a barrier, delaying hydrogen absorption/desorption processes making practical applications of metal hydrides very challenging. The waiting period before hydrogen absorption initiation is termed the incubation time, ranging from minutes to days. Prolonged incubations are undesirable, necessitating pre-treatment.

All industrial methods of manufacturing metals and alloys will be affected in this manner. The SPL must be broken because hydrogen is forced through the initial layer during the initial hydrogenation. Therefore, an activation process becomes essential to eliminate SPL. This activation process or first hydrogenation is usually conducted at high temperatures and hydrogen pressures. Common methods involve vacuum exposure at high temperatures or purging with inert gas to remove pre-adsorbed species, a process known as degassing. Degassing can be

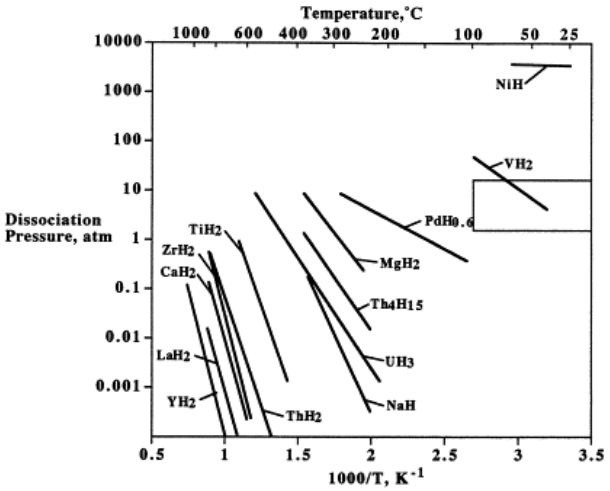

Figure 1.4: Van't Hoff lines (desorption) for elemental hydrides. Box indicates 1–10 atm, 0–100 °C ranges [24].

monitored via weight loss (gravimetric system) or pressure decrease (volumetric system) [23].

Activation should be considered an important factor in the design of a tank system. The tank must be designed for a range of temperatures and pressures greater than the working conditions. In contrast, filling the tank with activated metal hydrides is difficult since activated alloys are generally more susceptible to air contamination. Given that activation is time-consuming and adds to costs, there is a push to explore methods that reduce incubation time and enable first hydrogenation at lower temperature and pressure, eliminating the need for activation.

1.4 Family of intermetallic compounds

Most of the naturally occurring elements of the periodic table can form hydrides under suitable conditions. However, Fig 1.4 demonstrates that the dissociation pressures and temperatures of most of the materials are unsuitable for practical purposes (0-100 °C and 1-10 bar of hydrogen pressure). Although vanadium satisfies these requirements, its reversible hydrogen capacity is insufficient. Hence, the development of alloys is necessary to fulfill the precise requirements of a particular practical application. Most intermetallic compounds for hydrogen storage are formed by alloying a metal that readily forms stable hydrides (A) with another element that do not form stable hydrides (B). Several types of intermetallics can be categorized according to their stoichiometry, including the AB (TiFe), AB_5 ($LaNi_5$, $CaNi_5$), AB_2 ($ZrMn_2$, ZrV_2), and A_2B (Mg_2Ni), etc.

1.4.1 AB_5 family

This class of alloy has an abundance of literature, primarily due to the interesting chemical properties of this alloy class. The fact that the A and B sites can be substituted relatively easily allows a wide variety of AB_5 compounds to be synthesized. Site A can be a lanthanide, calcium, yttrium, or zirconium, but mischmetal is often used in industrial applications [25]. Generally, mischmetal refers to a mixture of rare earth elements composed of varying naturally occurring proportions. Most B sites are composed of nickel, although substitutions with Sn, Al, Pt, Rh, and Si are common [26, 27, 28, 29, 30]. Various hydrogen storage properties can be controlled by substituting on the A and B sites, including plateau pressure, slope, hysteresis, resistance to cycling, and contamination. Unfortunately, improving one property often leads to the deterioration of another. Therefore, multiple substitutions are one of the active research fields in AB_5 alloys.

1.4.2 AB_2 family (Laves phases)

The intermetallic family is derived from the Laves phase structure. It consists of three structures namely, hexagonal $MgZn_2$ (C14), cubic $MgCu_2$ (C15), and hexagonal $MgNi_2$ (C36). With Ti and Zr on site A and different combinations of 3d atoms at B-site, we can obtain potential AB_2 family [31, 32, 33, 34]. Zr-based AB_2 family are attractive due to good hydrogen storage capacity, faster kinetics, longer life, etc. But they suffer from the hydrides being too stable and susceptible to impurities [35, 36, 37, 38]. Many factors affect their stability, like differences in electronegativity, valence electron concentration, packing density, and geometry. However, the usefulness of these concepts for predicting new alloys is limited [39]. Optimal hydrogen storage properties are achieved by employing multicomponent systems [40, 41, 42].

1.4.3 BCC solid solutions

Unlike an intermetallic compound, a solid solution alloy does not need a stoichiometric composition and may designed in a random stoichiometry. The Most popular bcc solid solutions are Ti–V–Mn, Ti–Cr–V, and Ti–Cr–Mn systems [43, 44]. However, studies have also been reported on Ti, Zr, V, and Pd-based alloys. This class of bcc solid solutions exhibits two plateaux: the first plateau is composed of very stable mono-hydride that does not desorb under practical conditions; the second plateau is composed of di-hydride is responsible for the reversibility. Reversible capacity is the ability to absorb-desorb at practical conditions. Therefore,

it is not desirable to have two plateaux. Besides, the first hydrogenation (activation) is also difficult for this class of metal-hydrides. Usually, heat treatment at elevated temperatures of 300-750 °C is required to activate the alloy, which is undesirable for practical applications [45]. Two challenges for utilizing bcc solid alloys for hydrogen storage are to destabilizing the mono-hydride (to improve reversible capacity) and making the activation possible at room temperature.

1.4.4 A_2B family

The A_2B alloys are typically formed by combining an alkali earth metal (A) with a transition metal (B). Mg_2Ni and Mg_2Fe are the two most common and reversible magnesium-based A_2B alloys. Mg_2Ni forms Mg_2NiH_4 at an elevated temperature of 300 °C under 2 MPa. It can store a large amount of hydrogen (3.6 wt%). Ti_2Ni alloys are another essential A_2B alloy that has received significant attention. However, the major disadvantage of this class is a high desorption temperature [46, 47].

1.4.5 AB family

Due to their lightweight and high-volumetric capacities, AB-type alloys are highly sought-after materials for developing intermetallic hydrides. At a temperature of 120 °C and pressure of 10 bar, TiNi can absorb up to 1.2 wt% of hydrogen. However, obtaining TiNi in powder form can be difficult as the alloy is very tough, and hydrogen absorption can be hindered by surface oxide formation. Nevertheless, composite alloys comprising TiNi can be generated using mechanical alloying without forming undesirable phases.

One of the well-known alloys in this class is TiFe, which can reversibly absorb up to 1.86 wt% of hydrogen [24]. The binary alloy TiFe demonstrated remarkable hydrogen sorption properties, showcasing its ability to readily absorb and release hydrogen at room temperature under moderate hydrogen pressure. However, the first hydrogenation of the alloy, often referred to as activation is complicated.

1.5 Applications of metal hydrides

Metal hydrides were first used in nuclear reactors as moderators because hydrogen slows down neutrons with minimal absorption [48]. Apart from the obvious hydrogen storage, metal-hydrides can be used for a variety of applications pointed out as follows and illustrated in Fig. 1.5:

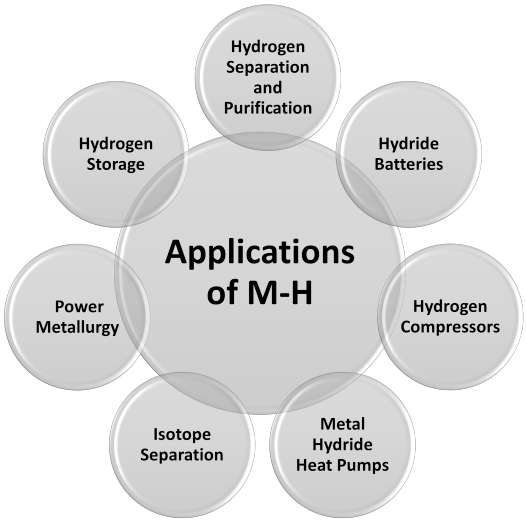

Figure 1.5: Various applications of metal hydrides

- *Thermal energy storage*: According to equation 1.3, the formation of a metal hydride is an exothermic reaction. Moreover, a metal hydride has a heat of formation about 10 times higher than that of a typical latent heat of salts, thus they may be used to store thermal energy.

- *Hydrogen compressors*: Based on the Van't Hoff equation 1.5, hydrogen pressure increases exponentially, which is why metallic hydrides can be used for hydrogen compression.

- *Metal-hydride heat pump*: Hydrogen gas flows freely between two hydrides with different thermal stabilities in a metal-hydride heat pump. This type of heat pump can also be used for cooling and refrigeration. The Van't Hoff plots of two hydrides are the best method for understanding the principle of the hydride heat pump.

- *Rechargeable batteries*: In rechargeable Ni-MH batteries, metallic hydrides serve as the negative electrode in accordance with the following equation:

$$(\mathrm{l/n})\mathrm{M} + \mathrm{H_2O} + \mathrm{e^-} \rightleftharpoons (\mathrm{l/n})\mathrm{MH}_n + \mathrm{OH^-} \tag{1.8}$$

  Nickel hydroxide acts as the positive electrode, undergoing the reaction below to form nickel oxyhydroxide.

$$\mathrm{Ni(OH)_2} + \mathrm{OH^-} \rightleftharpoons \mathrm{NiOOH} + \mathrm{H_2O} + \mathrm{e^-} \tag{1.9}$$

  to form the oxyhydroxide of nickel. The overall cell reaction is then:

$$(\mathrm{l/n})\mathrm{M} + \mathrm{Ni(OH)_2} \underset{\text{discharge}}{\overset{\text{charge}}{\rightleftharpoons}} (\mathrm{l/n})\mathrm{MH}_n + \mathrm{NiOOH} \tag{1.10}$$

- *Isotope separation*: Deuterium and tritium are separated from hydrogen using metallic hydrides because the hydride forming thermal stabilities of protides differ from deuterides or tritides. Generally, protides of metals are more stable than the corresponding deuterides or tritides.

- *Hydrogen separation and purification*: Hydrogen is selectively absorbed by hydride-forming metals and alloys. This way, hydrogen can be removed from gas mixtures and free from impurities. Using such a technique for separation poses the most severe problem of poisoning the hydride alloy with other gases present in the hydrogen gas.

- *Powder metallurgy*: During the formation of hydrides, metals typically expand rapidly, resulting in powdered hydrides; following the removal of hydrogen, the metal will be finely powdered. Metal powders such as Ti, Th, Zr, etc., have been prepared with this method for subsequent compaction into the desired shape.

1.6 Research issues (Motivation)

Of all the binary alloy solid-state hydrogen storage materials, TiFe alloy is one of the most promising. It can absorb and desorb hydrogen reversibly at ambient temperature and is made with relatively low-cost elements [1, 24]. This alloy has reasonably good storage capacity and fast kinetics. It could be used for a wide range of applications, such as stationary as well as mobile and portable applications, fuel cell submarines, ships, etc.

As stated earlier, a primary impediment is that the alloy's first hydrogenation, also called activation, is difficult [1]. This difficulty arises due to surface oxidation during synthesis and handling of the alloy. The first description of an effective activation process of TiFe alloy was suggested in Reilly and Wiswall's pioneering work [1]. It requires heating the alloy to more than 400 °C and keeping it at that temperature for an hour, either under a vacuum or at low hydrogen pressure, then cooling it to room temperature and applying a high hydrogen pressure of about 65 bar. If the alloy does not activate within 15 minutes, it is necessary to repeat the process a few times until the alloy activates. This increases the cost of the hydride and makes it less competitive compared to other hydrogen storage methods. Since then, a multitude of studies have used this activation procedure [24, 49, 50]. Several alternative techniques have also been explored to overcome this first hydrogenation limitation. Techniques such as doping, adding, or substituting a part of the TiFe alloy with other elements have been investigated. Adding and/or substituting small amounts of elements could be from transition metals [51, 52, 53] and rare earth elements [54, 55]. Mechanical deformation could also enhance the first hydrogenation [56, 57, 58, 59, 60].

Numerous studies have been reported on TiFe alloy added with transition elements. However, the number of investigations on adding rare earth elements to TiFe alloy for hydrogenation has been very limited. Therefore, a more rigorous analysis of this system is important. The readers are referred to a detailed literature review presented in Chapter 2.

1.7 Research objectives

In this project, we investigated the effect of adding rare earth elements La and Ce as well as an intermetallic $LaNi_5$ on the hydrogen sorption properties of TiFe alloy. The choice of La and Ce as rare earth elements was based on their inability to form intermetallic compounds with Ti, Fe, and TiFe, thus suggesting the likelihood of forming a composite. Notably, La and Ce are among the least expensive rare earth metals, which motivated our focus on investigating these elements. However, La forms a stable hydride, so a compound of La with Ni ($LaNi_5$) was also selected as an additive owing to its easy activation and formation of reversible hydride at room temperature [61]. Thus, it is expected that a composite of TiFe and $LaNi_5$ would not only help in providing a gateway for hydrogen via $LaNi_5$ reaching the main matrix TiFe but also help in reversible desorption. Additionally, for hydrogen storage applications TiFe is more cost-effective than $LaNi_5$.

The main objective of this research is to gain a fundamental understanding of metal-hydrogen interactions by exploring how La, Ce, and $LaNi_5$ additives influence the hydrogen sorption behavior of the TiFe alloy. By adding a secondary phase/region made of additives to the main TiFe phase, a gateway for hydrogen reaching the primary matrix is possible. This may lead to synergetic effects of fast and easy first hydrogenation. The aim and objectives of the project could be stated as follows:

- Elimination of rigorous activation procedure- achieve ease in first hydrogenation.
- Possible synergetic effects due to the combination of TiFe and additives on metal-hydrogen interaction.
- The main objective of this project is to investigate the overall effects on hydrogen storage properties of TiFe alloy with a series of rare earth addition.

In previous studies, it was established that a minimum of 4 at% of additive was required to achieve rapid initial hydrogenation in TiFe alloy [51, 52, 62, 63, 64, 65, 66, 67, 68, 69, 70, 71, 72, 73]. In order to be sure that this threshold is met in the present investigation, we opted to introduce 16 wt% of additives (corresponds to 10 at% of $LaNi_5$ and 6.6 at% of La or Ce). Since this research aimed to investigate the influence of additives on the initial hydrogenation, the primary objective was not to optimize the composition but to determine the presence or absence of an effect. Hence, a relatively high loading of additives was chosen for this purpose.

The present study differs from earlier investigations as the alloy synthesis was carried out primarily by exploring a new strategy of combining ball milling and

arc melting. Since the synthesis of the alloy plays a pivotal role in determining the microstructure and consequently impacting the alloy's properties. Therefore, the additives in our study were introduced by the following processes different from the reported studies:

1. A short-duration ball milling of already synthesized TiFe with additives was performed to maintain the composite nature of the alloy. The process is referred to as mechanical milling (MM). The synthesized TiFe was either be by arc melting or ball milling.

2. By ball milling the mixture of Ti, Fe, and the additives to achieve the TiFe alloy with additives instead of synthesizing by arc melting. The process is known as mechanical alloying (MA).

1.8 Thesis organization

The rest of the thesis is structured as follows. Chapter 2 describes the state-of-the-art literature review. Chapter 3 focuses on the experimental details- materials and methods. Chapter 4 deals with the preliminary studies on the synthesis and hydrogen sorption of pure TiFe alloy. Chapters 5, 6, and 7 present the investigation on TiFe with additives synthesized by various combinations of arc melting and ball milling. Finally, chapter 8 concludes the findings of this thesis work highlighting the major contributions and outlining potential avenues for future research.

CHAPTER 2

Literature survey

A state-of-the-art literature review is presented in this chapter. Section 2.1 presents the basics of TiFe alloy with its crystal structure and phase diagram. Section 2.2 reviews the literature on the effect of mechanical deformations on the crystal structure, microstructure, and hydrogen sorption properties. These mechanical deformations could be achieved by ball milling, cold rolling, groove rolling, and equal channel angular pressing to name a few. Section 2.3 deals with the studies reported on TiFe alloy with the addition and substitution of various elements from the periodic table. Finally, the identified research gap is highlighted in the concluding remarks section 2.4.

2.1 Basics of TiFe alloy

2.1.1 Crystal structure of TiFe alloy

With a Pearson symbol of cP2 and a Strukturbericht designation of B2, the equiatomic TiFe alloy has a CsCl-cubic crystal system prototype structure. It corresponds to the Pm-3m (No.221) space group [74] having lattice parameter values ranging from 2.953 Å to 2.983 Å [69, 75] with the atomic positions of Fe at the (1a) site (0, 0, 0) and Ti at the (1b) site (0.5, 0.5, 0.5), respectively [76, 77]. Since different kinds of atoms are present at the crystal's corners and center, the crystal system is not a true body-centered cubic (BCC). It is interpreted as two primitive cubic sub-lattices where each corner atom of one sub-lattice is positioned at the center of the other sub lattice, as illustration in Fig. 2.1(a). A TiFe unit cell contains two atoms, twelve tetrahedral interstices, and six octahedral interstices.

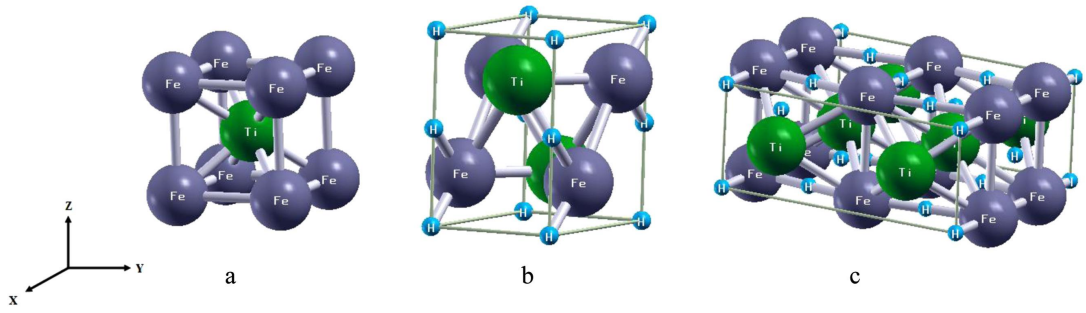

Figure 2.1: (a) The CsCl-cubic system of bulk TiFe, (b) the orthorhombic $P222_1$ FeTiH, (c) the orthorhombic C*mmm* $FeTiH_2$, gray, green and blue spheres represent Fe, Ti and H atoms, respectively [80].

In a tetrahedral interstice, two titanium atoms (Ti) and two iron atoms (Fe) surround each other, giving the configuration Ti_2Fe_2. As a result of containing two types of elements, TiFe alloys possess two octahedral configurations. A Ti_4Fe_2 interstice is formed when four Ti atoms and two Fe atoms surround an octahedron interstice.

While TiFe exhibits a CsCl-type structure corresponding to Pm-3m (221) space group, TiFeH and $TiFeH_2$ possess an orthorhombic structure characterized by the $P222_1$ (space group 17) [78] and C*mmm* (space group 65) [79], respectively. In TiFeH, hydrogen occupies an octahedral site (2a) surrounded by four Ti and two Fe atoms, as illustrated in Fig. 2.1(b). In contrast, $TiFeH_2$ features two kinds of octahedral H-sites: one (2a and 2c) resembling the coordination with TiFeH, and another (4e) enclosed by four Fe and two Ti atoms, depicted in Fig. 2.1(c).

2.1.2 Phase diagram of Ti-Fe

Based on the phase diagram shown in Fig. 2.2, it is apparent that the equilibrium binary Ti-Fe system is a complex alloy system. This system consists of two invariant chemical compounds (TiFe and $TiFe_2$), four invariant reactions, and four solid solutions in the Ti-rich region (αTi) and (βTi) and the Fe-rich region (αFe) and (γFe). The peritectic reaction at 1317 °C is vital because it forms TiFe from molten liquid and $TiFe_2$ at the maximum Fe concentration of 50.3 at% (Eq. 2.1). The minimum Fe concentration that could form TiFe is at 47.5 at% during eutectic reaction at 1085 °C. It should be noted that the composition range for the formation of TiFe is very narrow.

$$\mathrm{L} + \mathrm{TiFe_2} \underset{1317\,^\circ\mathrm{C}}{\overset{\text{Peritectic}}{\rightleftharpoons}} \mathrm{TiFe} \tag{2.1}$$

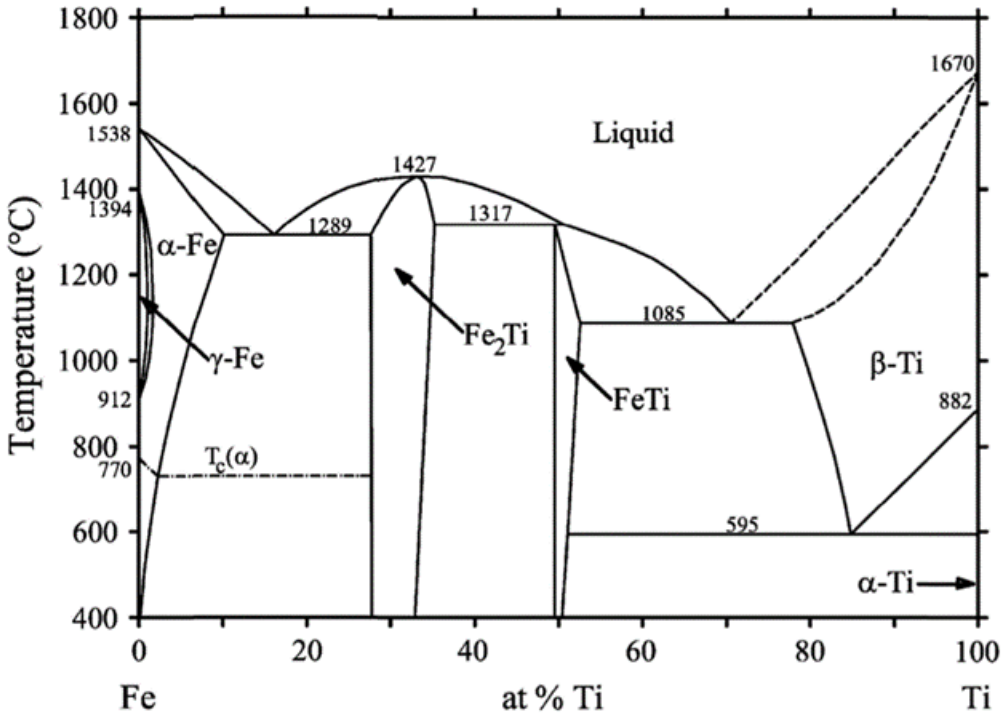

Figure 2.2: Phase diagram of Ti-Fe [81, 82].

2.2 Effect of mechanical deformations

It has been extensively researched how alloying can modify the microstructural features of TiFe alloy to improve hydrogenation. Moreover, mechanical deformations is also shown to improve hydrogenation. Mechanical deformation techniques, by creating accessible nucleation sites for hydrogenation in TiFe, have been explored widely [56, 57, 59, 83, 84, 85, 86, 87, 88]. Such deformations can be achieved by ball milling (BM) [56, 57, 89, 90], groove rolling (GR) [58], cold rolling (CR) [60], and high-pressure torsion (HPT) [58, 59].

Aoyagi *et al.* investigated the hydrogen sorption properties of FeTi & Mg_2Ni alloys, which typically require activation treatment, and $LaNi_5$ & $TiFe_{0.8}Mn_{0.2}Zr_{0.05}$ alloys, which are typically activation-free [56]. The alloys were subjected to ball milling in an inert gas atmosphere. Subsequently, the ball-milled powders were hydrogenated with or without exposure to air. The findings demonstrated that milling of these alloys in an inert gas atmosphere reduces the powder size and creates new surfaces, which are effective for hydrogen absorption without pre-activation.

Hotta *et al.* examined the activation of TiFe alloy synthesized by mechanical alloying from elemental powers [89]. The alloy absorbed 1.3 wt% hydrogen and required a heat treatment at 573 K before activating at room temperature under 150 bar hydrogen pressure. Abe and Kuji published a study on MA TiFe with

post-annealing at 773 K, exploring its hydrogen absorption properties [90]. They achieved a maximum hydrogen storage capacity of 1.25 wt% at a pressure of 50 bar of hydrogen. Instead of synthesizing TiFe from elemental powders, Emami *et al.* milled a commercial TiFe alloy which absorbed 1.5 wt% hydrogen at room temperature without the rigorous activation process [57].

Edalati *et al.* observed the absorption of 1.7 wt% hydrogen at room temperature in TiFe alloy that underwent high-pressure torsion (HPT) processing without pre-activation [59]. The HPT-treated TiFe alloy displayed a heterogeneous microstructure consisting of nanograins, coarse-grains, amorphous-like phases, and disordered phases. These structural characteristics were accompanied by a Vickers hardness of 1050 Hv. The observed increase in diffusivity may contribute to the activation of TiFe alloy subsequent to HPT processing. Furthermore, the formation of nanograins through HPT processing and the partial amorphization and disordering of surface oxides might serve as two additional possible factors contributing to the activation phenomenon.

In a separate investigation, Edalati *et al.* documented the first hydrogenation mechanism of the HPT processed TiFe alloy [91]. Following HPT, surface segregation occurred, leading to the formation of Fe-rich islands and cracks. These Fe-rich islands are proposed to serve as catalysts for hydrogen dissociation, while the cracks and boundaries between nanograins acted as gateways for hydrogen transport through the oxide layer. The accelerated atomic diffusion resulting from HPT is responsible for the surface segregation and facilitated hydrogen transportation. The study demonstrated that the severe plastic deformation brought about by HPT accelerates the rate of hydrogenation by modifying the surface properties, and catalytically activating the hydrogen storage materials under ambient conditions. The activation induced in nanostructured TiFe alloy by HPT persisted even after extended storage in ambient air for months.

In another study, Edalati *et al.* employed groove rolling (GR) to investigate the hydrogenation of TiFe alloy [58]. The groove-rolled sample exhibited a heterogeneous microstructure characterized by the presence of subgrains with a high density of dislocations and cracks. In contrast to the HPT-processed sample, no surface segregation was observed in the groove-rolled sample. These findings suggest that surface segregation is not a prerequisite for activation through plastic deformation. Instead, the formation of subgrain boundaries, grain boundaries, and cracks serves as the primary mechanism for facilitating hydrogen transport across the oxide layer. Hydrogen absorption in the coarse-grained annealed sample was below 0.2 wt%, while the groove-rolled sample absorbed 0.3 wt%, 1.0 wt%, 1.4 wt%, and 1.7 wt% of hydrogen in the first, second, third, and fourth

hydrogenation cycles, respectively. The HPT-processed sample, which contained nanograins, consistently absorbed 1.72 wt% of hydrogen in all hydrogenation cycles. Both the groove-rolled and HPT-processed samples demonstrated activation, and the samples remained activated even after prolonged exposure to air.

In their study, Zaluski *et al.* investigated the effect of the milling environment on the final structure of pre-synthesized TiFe alloy and the mechanical alloying of elemental powders Ti and Fe [85, 86, 92, 93, 94, 95]. Their research findings can be categorized into three key aspects: (a) If the oxygen content resulting from both the material and the milling environment exceeded 3.0 at%, it formed amorphous TiFe, predominantly consisting of a single-phase material with a small quantity of TiFe nanocrystals. Furthermore, when the oxygen content surpassed 5.0 at%, a Ti-rich amorphous phase developed, accompanied by embedded particles of unreacted iron. (b) Milling the pre-synthesized TiFe alloy under similar oxygen content conditions resulted in the selective oxidation of titanium, causing the material to disintegrate into TiO and α-Fe. (c) In cases where the vial was not opened during the process, and the milling of elemental powders Ti and Fe was conducted for a predetermined duration of intermetallic formation, the oxygen content remained below 3.0 at%. This condition led to the growth of the interfacial β-Ti(Fe) phase. It ultimately led to an increased average iron concentration in the β-Ti(Fe) phase and the formation of nanocrystalline TiFe alloy. The activation of the nanocrystalline TiFe was found to be significantly easier.

2.3 Effect of substitution/addition

Facilitating activation in the TiFe alloy by adding or substituting other transition elements have been widely explored ([51, 52, 53, 62, 67, 72, 73, 96, 97, 98, 99, 100] and references therein). Jain *et al.* reported activation at room temperature with a moderate pressure of 40 bar by Zr, Ni, and Zr_7Ni_{10} doping to TiFe. The doped TiFe activated readily at room temperature favoring the Zr addition over Ni doping [51]. Lv *et al.* studied hydrogen storage properties of $Ti_{0.95}FeZr_{0.05}$, $TiFe_{0.95}Zr_{0.05}$, and $TiFeZr_{0.05}$ alloy compositions at room temperature under 2 MPa of hydrogen. They reported that a minute composition alteration impacts microstructure and hydrogen storage behaviors. The Ti-substituted alloy showed faster kinetics, while Fe-replaced absorbed the maximum H_2 among the three compositions [62].

A recent study on Hf addition to TiFe synthesized by arc melting observed that a minimum of 8 wt% Hf is needed to achieve ease in first hydrogenation, but the kinetics was slow, reaching 1.2 wt% H_2 in 8 hours. Furthermore, 16 wt% Hf to TiFe showed fast kinetics corresponding to a maximum hydrogen capacity

of 1.5 wt% in less than 90 min [67]. Bououdina *et al.* investigated the effect of Ni on the hydrogen sorption properties of TiFe alloy synthesized by ball milling [101]. It was observed that the Ni added TiFe readily absorbed hydrogen without any pre-activation. Ball milling had the effect of generating fresh surfaces of TiFe particles in the micrometer range, coated by refined nickel grains. These grains acted as catalytic centers for the dissociation of hydrogen molecules. The resulting material exhibited increased resistance to air for an extended period.

Few studies on adding and substituting elements from s and p-blocks of the periodic table to TiFe were also reported [72, 73, 102, 103]. To the best of our knowledge, the number of investigations on adding rare earth elements to TiFe alloy for hydrogenation has been very limited [54, 55, 69, 104, 105, 106, 107, 108, 109, 110, 111, 112, 113].

The hydrogen storage properties of TiFe + 4.5 wt% Mm (misch metal) alloy was investigated by Bronca *et al.* [112]. The alloy exhibited rapid activation at room temperature without requiring any thermal treatment. The researchers proposed an activation mechanism in which the Mm inclusions caused differential expansion while hydriding, leading to the formation of cracks within the TiFe matrix. This differential expansion was attributed to the preferential absorption of hydrogen by the Mm. Consequently, these cracks provided new surfaces free of oxides, enabling hydrogen to penetrate into the bulk TiFe material. Ma *et al.* examined the hydrogen storage properties of $FeTi_{1.3}$ + x wt% Mm (x = 0.0, 1.5, 3.0, 4.5, 6.0) alloys [104]. The findings demonstrate a significant enhancement in the activation characteristics of a FeTi alloy when modified with excess Ti and a small quantity of Mm. The modified alloys exhibit notable hydrogen absorption after a short incubation period at room temperature without prior thermal treatment. Moreover, the hydrogen storage properties of the modified alloys show variations depending on the Mm content and reaction temperature.

Wang *et al.* investigated the hydrogen storage characteristics of lanthanum-added TiFe alloys with compositions Ti_xFe + y wt% La (x = 1.0–1.2; y = 0–5) [54]. They found that the over-stoichiometry of Ti and the addition of La improved the activation behavior of TiFe alloy. The alloys fully activated after a few cycles, and initial hydrogenation showed incubation times from 1 hour to 15 minutes as the proportion of La increased. They also reported the formation of stable hydrides TiH_x and LaH_x. To explain the activation behavior, they proposed three possible mechanisms: (a) the secondary phases Ti and/or La preferentially hydride into TiH_x and LaH_x, causing the formation of microcracks due to volume expansion. Consequently, a new oxide-free surface becomes available for the hydrogenation of the TiFe compound; (b) formation of the TiH_x and LaH_x phases that acts as a fast

diffusion channel for H atoms to get transferred from the Ti or La surface to TiFe. In this mechanism, H_2 dissociation is facilitated by the metallic inclusions (Ti, La), leading the H atoms to jump into the subsurface layers of the TiFe matrix; (c) in the third possible mechanism, the interface plays an important role. Hydriding/dehydriding through TiFe-Ti or TiFe-La interface facilitates the transfer of H atoms from the secondary phase to the main matrix TiFe. They emphasized that further study is needed to investigate which mechanism dominates the La-TiFe system.

In another study, Leng *et al.* investigated Ce addition in $TiFe_{0.9}Mn_{0.1}Ce_x$ (x = 0, 0.02, 0.04, 0.06) alloys [55]. They found that the time for full activation decreased with increasing Ce content. The composition $TiFe_{0.9}Mn_{0.1}Ce_{0.06}$ reached 1.05 wt% within 2 hours in the first absorption and a total capacity of 1.70 wt% after repeated cycles at 80 °C. Gosselin *et al.* investigated the enhancement of the initial hydrogenation of TiFe by incorporating yttrium [69]. The compositions examined consisted of TiFe + x wt% Y, where x = 4, 6, and 8. Through electron microscopy analysis, it was determined that all alloys exhibited a multiphase structure, characterized by a TiFe matrix phase containing less than 0.4 at% of yttrium, along with a secondary phase rich in yttrium. As the yttrium content (x) increased, both the chemical compositions of the matrix and the secondary phase underwent changes. Notably, the alloy with 8 wt% Y exhibited the most rapid kinetics.

Li *et al.* conducted a study to investigate the impact of a small amount of yttrium (Y) on the hydrogen storage properties of $Ti_{1.1-x}Y_xFe_{0.8}Mn_{0.2}$ alloys (x = 0, 0.02, 0.04, 0.06, 0.08) synthesized through induction melting [106]. As the Y content gradually increased, the excess Y was observed to precipitate as a distinct phase. The addition of Y led to an improvement in the activation property of the alloy at room temperature. Among the tested specimens, the $Ti_{1.08}Y_{0.02}Fe_{0.8}Mn_{0.2}$ alloy exhibited excellent performance at room temperature with a hydrogen absorption capacity of 1.84 wt%. Han *et al.* synthesized an alloy through induction melting, with a composition of $Ti_{1.1-x}Zr_{0.1}Y_xFe_{0.6}Ni_{0.3}Mn_{0.2}$ (x = 0-0.08) [105]. By incorporating the rare earth element Y to partially substitute Ti in TiFe alloys, the activation properties and hydrogen absorption/desorption kinetics were significantly enhanced. The findings revealed that the as-cast alloy consisted of a Ni-rich TiFe primarily phase, with a minor phase of $ZrMn_2$, along with a Y-rich phase. The addition of Y notably increased the phase boundary and refined the crystallization, resulting in a substantial reduction in the activation incubation period of the cast alloy. Moreover, at a Y content of 0.02, the alloy exhibited a maximum hydrogen absorption capacity of 1.70 wt% at 70 °C. Ali *et al.* found a

Cu_2Y intermetallic phase while studying $Ti_{0.95}Y_{0.05}Fe_{0.86}Mn_{0.05}Cu_{0.05}$ alloy [110]. The presence of the Cu_2Y intermetallic phase and the interfaces between the secondary phase and the alloy matrix led to enhanced activation and dissolution kinetics during the interaction of hydrogen with the alloy powder.

Shang *et al.* reported the effect of Pr on the hydrogenation storage behavior of $Ti_{1.1-x}Fe_{0.7}Ni_{0.1}Zr_{0.1}Mn_{0.1}Pr_x$ (x = 0-0.08) alloys synthesized by induction melting [107]. The generation of the Pr segregated phase led to the TiFe grain refinement and the lattice expansion of the TiFe cell. The grain refinement and the presence of Pr increased the nucleation rate, enhancing the hydrogenation kinetics. Another study by the same group on the effect of Sm on the hydrogen sorption on $Ti_{1.1-x}Fe_{0.6}Ni_{0.1}Zr_{0.1}Mn_{0.2}Sm_x$ (x = 0-0.08) observed the formation of Sm_3H_7 phase [108].

Although $LaNi_5$ has been extensively studied as an intermetallic compound for hydrogen storage, its application as the primary alloy is limited due to its low capacity. Moreover, for hydrogen storage applications TiFe is more cost-effective than $LaNi_5$. A powder mixture consisting of 50TiFe-50$LaNi_5$ compacted at 500 MPa was investigated by Bratanich *et al.* [114]. Under 6 MPa hydrogen pressure, the compacted mixture gets activated at room temperature without undergoing preliminary thermal or vacuum treatments. When powders are pressed, they become dispersed and create fresh surfaces in addition to generating inter-phase bonds. A crucial role was played by the catalytic qualities of the interphase bond and the fresh intermetallic surfaces protected from oxidation by the contacts. Zhang *et al.* reported the activation of a compound synthesized by mechanical alloying (duration 1 h) of TiFe and $LaNi_5$ intermetallics in the ratio 9:1 [115]. Small $LaNi_5$ particles on comparatively large TiFe particles were observed in TEM. As suggested by the authors, the necessary catalytic activation for H_2 dissociation and path from the surface to the interior of TiFe is provided by the small $LaNi_5$ particles.

2.4 Closing remarks on literature

Tables 2.1 and 2.2 provide a comprehensive summary of selected literature studies, categorized based on the synthesis process, which investigated the improvement of hydrogenation in TiFe alloys through the addition of rare earth and transition metals, respectively. It can be observed that the TiFe alloy with additives synthesized by induction melting generally shows a hydrogen absorption capacity close to that of pure TiFe alloy i.e., $\approx$ 1.9 wt%. TiFe alloy with additives synthesized by mechanical alloying shows lower hydrogen absorption capacity. Samples synthe-

sized by arc melting shows hydrogen storage capacity in between induction melted and ball milled samples. A handful of studies on the TiFe alloy with additives synthesized by mechanical alloying or milling has been reported in the literature [101, 115, 116, 117, 118].

Table 2.1: A summary of studies from the literature that explored the use of rare earth metals in enhancing the hydrogenation of TiFe alloy.

Synthesis process	**Composition**	**Absorption (wt%), conditions**	**PCT, thermodynamics**	**Remarks**	**Ref.**
RF levitation melting	$Ti_{1.1}Fe$ + 5 wt% La	1.84 (1 h), RT, 60 bar	20, 30, 65 °C ΔH_d = 26.7 kJ/mol ΔH_a = -24.8 kJ/mol	No change in thermodynamics	[54]
Induction melting	$TiFe_{0.90}Mn_{0.10}Ce_{0.06}$	1.05 (2 h), 80 °C, 40 bar	25 °C	Capacity recovery after 150 cycles at 350 °C	[55]
Induction melting	$Ti_{1.1-x}Y_xFe_{0.8}Mn_{0.2}$ (x = 0-0.08)	1.14 to 1.84 with x, 100 °C, 40 bar	ΔH_d = 30.0 to 25.6 kJ/mol with x	Y-precipitate	[106]
Induction melting	$Ti_{1.1-x}Zr_{0.1}Y_xFe_{0.6}Ni_{0.3}Mn_{0.2}$ (x = 0-0.08)	1.45 to 1.82 with x, 150 °C, 30 bar	ΔH_d = 26.2 to 33.8 kJ/mol with x	Minor $ZrMn_2$ phase, Y-rich phase	[105]
Induction melting	$Ti_{1.1-x}Fe_{0.7}Ni_{0.1}Zr_{0.1}Mn_{0.1}Pr_x$ (x = 0-0.08)	1.4 to 1.6 with x, 150 °C, 30 bar	ΔH_a = -23.3 to -31.8 kJ/mol with x	Desorb 0.4 wt% at 40 °C, 1.17 wt% at 100 °C	[107]
Induction melting	$Ti_{1.1-x}Fe_{0.6}Ni_{0.1}Zr_{0.1}Mn_{0.2}Sm_x$ (x = 0-0.08)	1.4 to 1.6 with x, 150 °C, 30 bar	ΔH_a = -21.3 to -27.8 kJ/mol with x	Desorb 0.4 at 40 °C, 0.9 wt% at 100 °C	[108]
Induction melting	$Ti_{1.3}Fe$ + 4.5 wt% Mm	1.71, RT, 20 bar	RT	Minor Ti_2Fe and Ti phases, Channel-like configurations after hydrogenation	[119]
Induction melting	$Ti_{1.3}Fe$ + 4.5 wt% Mm	1.90, 100 °C, 20 bar	100 °C		[119]
Induction melting	$Ti_{1.4}Fe$ + 4.5 wt% Mm	1.85, 100 °C, 20 bar	100 °C		[119]
Induction melting	$Ti_{1.5}Fe$ + 4.5 wt% Mm	1.17, 100 °C, 20 bar	100 °C		[119]
Induction melting	$Ti_{1.3}Fe$ + x wt% Mm (x = 0.0, 1.5, 3.0, 4.5, 6.0)	RT, 40 bar	25, 45, 60 °C	Short incubation period at RT	[104]
Arc melting	TiFe + 4.5 wt% Mm	1.6, 21 °C, 60 bar	27 °C	Mm dispersed as spherical inclusions	[112]
Arc melting	$TiFeY_{0.04}$	1.2 (18 h), RT, 25 bar	-	No pre-activation, Y-rich phase	[69]
Arc melting	$TiFe_{0.9}Cr_{0.1}Y_{0.05}$	1.4, 30 °C, 30 bar	ΔH_d = 35.4 kJ/mol	Pre-heating at 200 °C,	[109]
Arc melting	$TiFe_{0.9}Mn_{0.1}Y_{0.05}$	1.5, 30 °C, 30 bar	ΔH_d = 31.2 kJ/mol	α-Y phase, YH_3	[109]
Not clear from the article	$TiFe_{0.86}Mn_{0.1}Y_{0.1-x}Cu_x$ (x = 0.01-0.09)	1.89 to 1.80 with x, 20 °C, 50 bar	ΔH_d = 20.8 to 19.2 kJ/mol	α-Y, CuY, and Cu_4Y phases	[110]
	$Ti_{0.95}Y_{0.05}Fe_{0.86}Mn_{0.05}Cu_{0.05}$	1.85, 20 °C, 46 bar	20, 30, 45, 60 °C	Cu_2Y phase	[111]

Table 2.2: A summary of studies from the literature that explored the use of transition metals in enhancing the hydrogenation of TiFe alloy.

Synthesis process	**Composition**	**Absorption (wt%), conditions**	**PCT, thermodynamics**	**Remarks**	**Ref.**
Arc melting	$Ti_{0.95}FeZr_{0.05}$	1.3 (6 h), RT, 20 bar	RT	Completely reversible	[62]
Arc melting	$TiFe_{0.95}Zr_{0.05}$	1.5 (6 h), RT, 20 bar	RT	Completely reversible	[62]
Arc melting	$TiFeZr_{0.05}$	1.4 (4 h), RT, 20 bar	RT	Completely reversible	[62]
Arc melting	$TiFeHf_{0.04}$	1.2 (8 h), RT, 20 bar	RT	No pre-activation	[67]
Arc melting	$TiFeHf_{0.09}$	1.5 (1 h), RT, 20 bar	RT	No pre-activation	[67]
Arc melting	$TiFeZr_{0.04}$	1.6 (0.5 h), 40 °C, 20 bar	40 °C	Desorb 1.2 wt%,	[52]
Arc melting	$TiFe_{0.90}Cr_{0.10}$	1.5, 30 °C, 30 bar	ΔH_d = 34.2 kJ/mol ΔS_d = 110 J/mol-K	-	[109]
Arc melting	$Ti_{0.95}FeV_{0.06}$	1.1 (0.5 h), 54 °C, 2 bar	-	Pre-heating to 427 °C	[53]
Arc melting	$TiFe_{0.50}Co_{0.50}$	1.1, RT, 30 bar	80, 100, 120 °C ΔH_d = 42.3 kJ/mol ΔS_d = 123 J/mol-K	Pre-activation at 200 °C with 30 bar H_2	[120]
-	$TiFe_{0.80}Ni_{0.20}$	1.3	ΔH = 41.2 kJ/mol ΔS = 119 J/mol-K	Very low plateau pressure (0.1 bar)	[24]
Induction melting	$TiFe_{0.90}V_{0.05}$	1.88, 25 °C, 25 bar	25 °C	Annealed 1 week at 1000 °C	[121]
Induction melting	$TiFe_{0.90}V_{0.10}$	1.96, 25 °C, 25 bar	25 °C	Annealed 1 week at 1000 °C	[121]
Induction melting	$TiFeMn_{0.05}$	1.55, 25 °C, 58 bar	25, 55, 85 °C		[122]

Table 2.2 continued from previous page

Synthesis process	Composition	Absorption (wt%), conditions	PCT, thermodynamics	Remarks	Ref.
			$^{1}\Delta H_d$ = 28.2 kJ/mol	^{1}- First plateau	
			$^{1}\Delta S_d$ = 105 J/mol-K		
			$^{2}\Delta H_d$ = 35.3 kJ/mol	^{2}- Second plateau	
			$^{2}\Delta S_d$ = 139 J/mol-K		
Induction melting	$TiFe_{0.90}Mn_{0.10}$	1.6 (100 h), 25°C, 40 bar	8, 22, 45 °CC	-	[123]
			ΔH_a = -21.8 kJ/mol		
			ΔS_a = -89 J/mol-K		
			ΔH_d = 30.3 kJ/mol		
			ΔS_d = 110 J/mol-K		
Induction melting followed by 30 min mechanical milling	$TiFe_{0.90}Mn_{0.10}$	1.4 (15 h), 25°C, 40 bar	8, 22, 45 °CC	-	[123]
			ΔH_a = -23.8 kJ/mol		
			ΔS_a = -93 J/mol-K		
			ΔH_d = 30.3 kJ/mol		
			ΔS_d = 105 J/mol-K		
Mechano-chemical synthesis	$TiFeZr_{0.04}$	1.10, 22 °C, 370 bar	22 °C	Pre-activation at 300 °C, Desorb 0.66 wt%	[71]
	$TiFeCu_{0.04}$	1.46, 22 °C, 400 bar	22 °C	Pre-activation 300 °C, Desorb 0.86 wt%	[71]
Mechanical Alloying	$TiFeCr_{0.08}$	1.0, 22 °C, 60 bar	22 °C	No dihydride phase	[72]
	$TiFeNb_{0.04}$	1.88, RT, 60 bar	ΔH_a = -23.2 kJ/mol	Second plateau absent	[70]
			ΔH_d = 25.3 kJ/mol		

CHAPTER 3

Experimental details

The experimental details are broadly classified into four sections. Section 3.1 describes the materials and techniques used to synthesize the required alloy compositions. Section 3.2 presents the way and modes in which ball milling, arc melting, and a combination of both are used to synthesize those alloys. Alloy characterization was done analytically using the X-ray diffraction (XRD) technique, scanning electron microscopy (SEM), and energy dispersive spectroscopy (EDX) as discussed in section 3.3. Finally, hydrogen sorption measurements were accomplished via Sievert's apparatus and the method is explained in section 3.4.

3.1 Materials and methods

All the pure elements, Ti, Fe, La, and Ce, were procured from Alfa-Aesar. Commercial $LaNi_5$ powder was purchased from Angstrom Power. The elements' purity level, particle size, and physical state are presented in Table 3.1. The crystallographic data of the elements and alloys used in this study are presented in appendix A.1.

Table 3.1: Elements and their physical state.

Elements	**Particle type**	**Particle size (mm)**	**Purity level (%)**
Ti	Sponge	3-19 mm	99.95
Fe	Granules	1-2 mm	99.98
La	Powder	-40 mesh (ampuled under Ar)	99.7
Ce	Ingot	Irregular (in mineral oil)	99.8
$LaNi_5$	Powder	Commercial	Commercial

In the present study, Ti and Fe powder were mixed in stoichiometric compositions with 16 wt% of La or Ce or $LaNi_5$. The said composition is hereinafter referred to as nominal composition. Tables 3.2, 3.3, and 3.4 depict the nominal compositions of the alloys by wt% as well as at%. The high weight percent of the additive was deliberately chosen to see the effect of the additive on microstructure and hydrogenation and to compare it with similar studies where Zr and Hf were added [51, 52, 62, 67].

Table 3.2: Nominal composition in terms of wt% and at% for TiFe + 16 wt% La.

Elements	**Ti**	**Fe**	**La**	**Confirmation**
atomic wt (g/mol)	47.867	55.845	138.905	-
weight of element (g)	1.163	1.357	0.480	3.000 (for 3g sample)
wt%	38.770	45.230	16.000	100.000
at%	46.682	46.680	6.639	100.000

Table 3.3: Nominal composition in terms of wt% and at% for TiFe + 16 wt% Ce.

Elements	**Ti**	**Fe**	**Ce**	**Confirmation**
atomic wt (g/mol)	47.867	55.845	140.116	-
weight of element (g)	1.163	1.357	0.480	3.000 (for 3g sample)
wt%	38.770	45.230	16.000	100.000
at%	46.708	46.706	6.659	100.000

Table 3.4: Nominal composition for TiFe + 16 wt% $LaNi_5$ sample in terms of wt% and at%.

Elements	**Ti**	**Fe**	**La**	**Ni**	**Confirmation**
atomic wt (g/mol)	47.867	55.845	138.905	58.693	-
weight of element (g)	1.163	1.357	0.154	0.326	3.000 (for 3g sample)
wt%	38.770	45.230	5.140	10.860	100.000
at%	47.974	43.972	2.009	10.045	100.000

3.1.1 High precision scientific balance

Weighing elements and alloy powder was done in a high-precision scientific balance with a maximum measurement capacity of 220 g with a precision of 0.1 mg. Calibration of the balance should be done before measurement to ensure correct weighing. Depending upon the type of balance, calibration can be done manually with known standard weigh blocks, or it can be done automatically. The precision balance used in the present study is an automatic calibration type.

3.1.2 Ball milling (BM)

Based on loading capacity, ball milling could be a laboratory or industrial technique. Laboratory BM can be planetary, rotary, or vibratory type. Alloy formation happens through the mechanical action of repeated fracture and welding. Ball milling involves many parameters, such as:

- Ball to powder weight ratio (BPR)
- Milling time
- Milling speed
- Ball and vial material type

Different types and sizes of balls and vials are available. Selection of a particular kind depends upon the hardness and the starting particle size of the material to be milled. Generally, BM is used to synthesize equilibrium and non-equilibrium alloy phases (usually at room temperature), such as:

- Supersaturated solid-solutions
- Nano-crystalline phases
- Metastable crystalline phases
- Amorphous alloys

Although BM is easy to use at a laboratory scale, the range of parameters as pointed out earlier is huge, which poses the following challenges:

- The comparison between studies from different types of BM is quite difficult.
- The relationship between the laboratory and industrial scale is not apparent. But optimization of milling parameters could give a direction to industrial apparatus.

The present study used a Spex high energy mill 8000M/D vibrating type (Spex® SamplePrep, Metuchen, NJ, USA). The vial in the clamp forms an eight-shape motion with 1060 cycles per minute [124, 125]. A representative image of the milling machine and the milling crucible and balls is shown in Fig. 3.1.

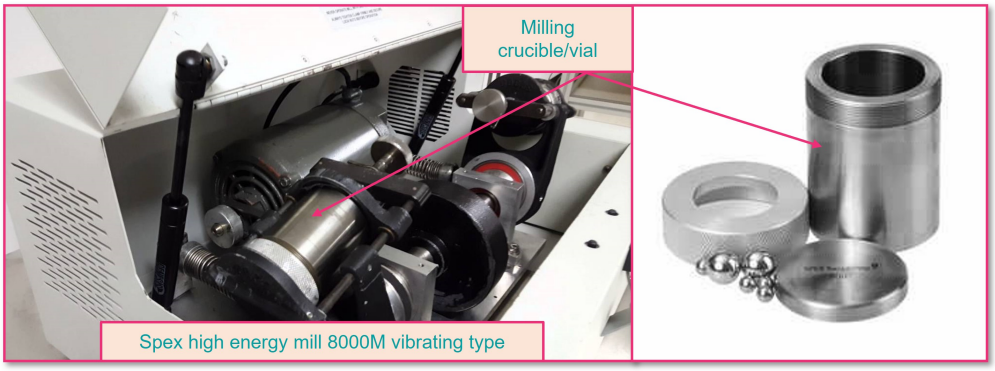

Figure 3.1: A representative image of the milling machine and the milling crucible and balls.

3.1.3 Electric arc melting

The electric arc melting furnace is of Centorr Associates Inc. USA, as shown in Fig. 3.2. It consists of a movable electrode attached to the stinger, a water jacket, a glass chamber, a copper crucible, an auxiliary power and coolant supply unit, and a vacuum pump with manifolds. The chamber has an entire 360° viewing area through Pyrex glass and is made of water-cooled brass on the top and bottom. When in use, the melt can be viewed clearly with the help of protective eye shields by obstructing the electric arc radiation. The material is filled in the copper crucible housed in the furnace chamber.

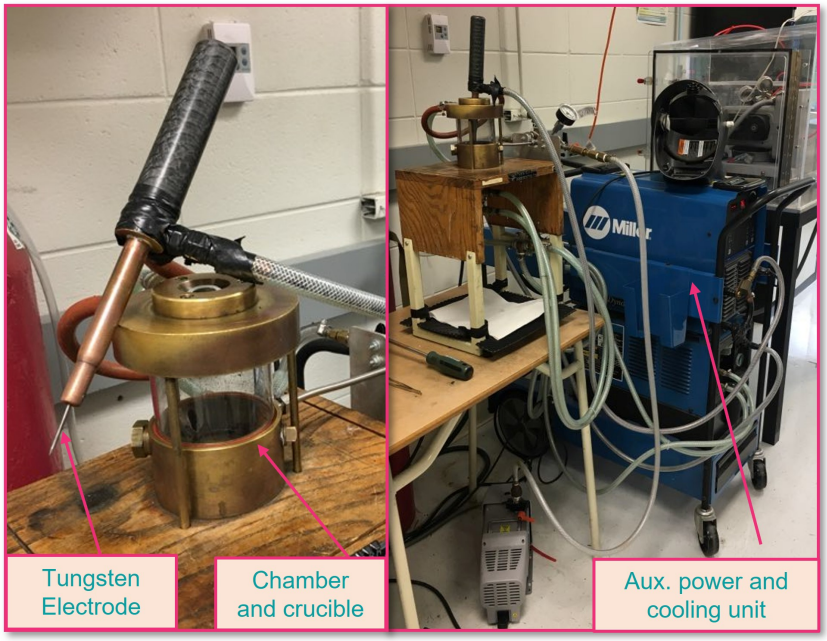

Figure 3.2: A laboratory scale electric arc melting furnace.

The furnace chamber is clamped firmly in place. The order of 0.1 Torr (mbar) vacuum is achieved with a vacuum pump to remove the atmospheric air after

loading the material. The chamber is evacuated and filled with argon gas to maintain an inert atmosphere. The auxiliary power supply and cooling unit are connected to the arc melting furnace with power cables and a water manifold. A pump enables the flow of coolant to the different components, such as the stinger, water jacket chamber, chamber top, and chamber base. An arc discharge is established inside the furnace by applying direct current (DC) to the electrode. Heating is achieved via this electric arc struck between the tungsten electrode and metals placed in the hearth. The stinger located at the top enables the movement of the welding arc at the user's will.

3.2 Alloy synthesis

Firstly, pure TiFe alloy was synthesized by two routes, namely- arc melting (casting) and ball milling (mechanical alloying, MA). Ball milling parameters were optimized to get the TiFe solid solution. In the next step, TiFe alloy with additives were synthesized by milling, casting, or combining both.

3.2.1 Synthesis of pure TiFe

Approximately 3 g of Ti-Fe stoichiometric mixture was inserted in a hardened steel crucible with hardened steel balls. The ball-to-powder weight ratio was 10:1. An argon atmosphere was maintained by closing the crucible inside a glove box. The ball milling was performed using a Spex 8000M/D high-energy mill vibrating type where the vial in the clamp undergoes an eight-shape motion at 1060 cycles per minute [124, 125]. During the sample preparation, a small amount of sample was taken out at regular intervals to monitor the structural evolution of the mixture. The sampling was done inside a glove box to avoid air exposure. As the goal of this process was to synthesize the TiFe intermetallic by milling raw elements, it is thereafter called mechanical alloying (MA).

The stoichiometric TiFe alloy was also synthesized by arc melting. An inert argon atmosphere was maintained in the arc furnace during melting. The solidified pellet was turned over and remelted at least three times to ensure homogeneity. Finally, the button-shaped pellet was hand crushed in a hardened steel mortar and pestle inside a glove box to get the TiFe powder (as-cast TiFe).

3.2.2 Inclusion of additives via mechanical milling (MM) to TiFe alloy synthesized by arc melting

The as-cast TiFe powder was mixed with the additives La, Ce, or $LaNi_5$. The powder mixture was filled in a hardened steel vial and balls in a 10:1 ball-to-powder weight ratio (BPR). The mechanical milling (MM) was performed in the same SPEX high energy 8000M/D milling machine.The milling duration was restricted to 15 minutes to preserve the composite nature of the material. Moreover, prolonged milling has been reported to affect hydrogen sorption kinetics negatively [88, 126]. The synthesized alloys TiFe + 16 wt% La, TiFe + 16 wt% $LaNi_5$, and TiFe + 16 wt% Ce are respectively designated MM (La-cast TiFe), MM ($LaNi_5$-cast TiFe), and MM (Ce-cast TiFe). The as-cast TiFe without additives was also mechanically milled and designated MM-cast TiFe. Fig. 3.3 depicts the alloy synthesis procedure in a flowchart.

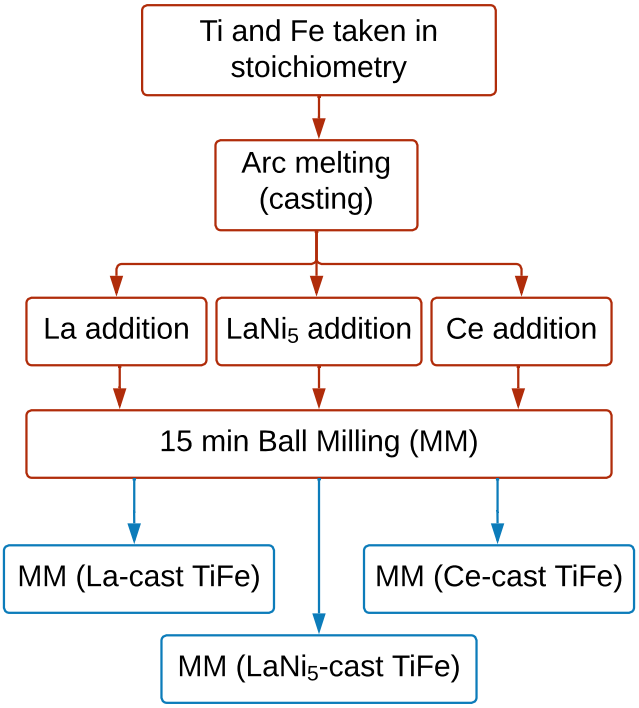

Figure 3.3: Flowchart showing process followed for synthesis of cast TiFe with additives by MM.

3.2.3 Inclusion of additives by mechanical milling (MM) to TiFe alloy synthesized by mechanical alloying (MA)

Fresh samples were prepared by mixing MA TiFe with additives and mechanically milling them. The mechanical milling (MM) procedure is as followed above. For simplicity, the synthesized samples (MA TiFe + 16 wt% La), (MA TiFe + 16 wt% Ce), and (MA TiFe + 16 wt% $LaNi_5$) are denoted as MM (La-MA TiFe), MM (Ce-MA TiFe), MM ($LaNi_5$-MA TiFe), respectively. Fig. 3.4 depicts the alloy synthesis procedure in a flowchart.

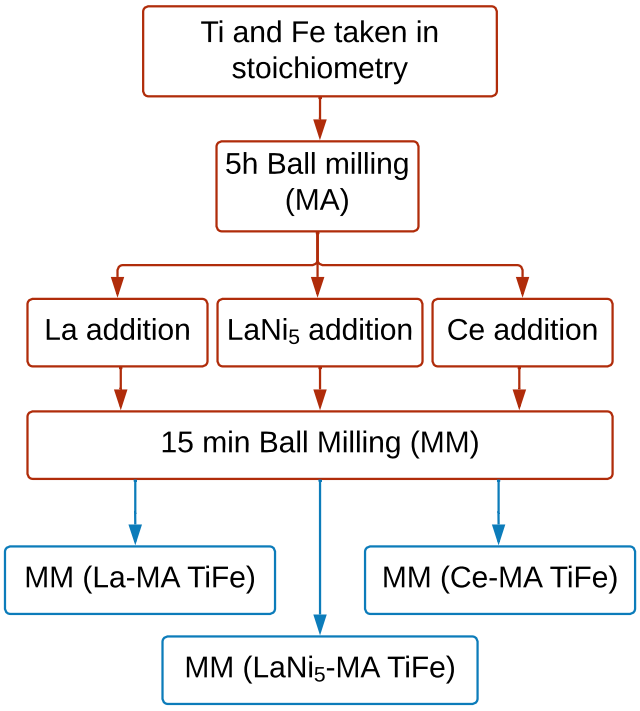

Figure 3.4: Flowchart showing process followed for the synthesis of MA TiFe added with additives by MM.

3.2.4 Synthesis of rare earth added TiFe via mechanical alloying (MA) only

Samples were also prepared by mixing and mechanically alloying elemental powders (Ti + Fe + 16 wt% La) and (Ti + Fe + 16 wt% Ce) denoted as MA TiFe-La and MA TiFe-Ce respectively, from the above-ascertained duration as in mechanical alloying (MA). Fig. 3.5 depicts the mechanical alloying procedure in a flowchart. Table 3.5 shows all the resultant alloys from various mode of synthesis that undergoes subsequent studies.

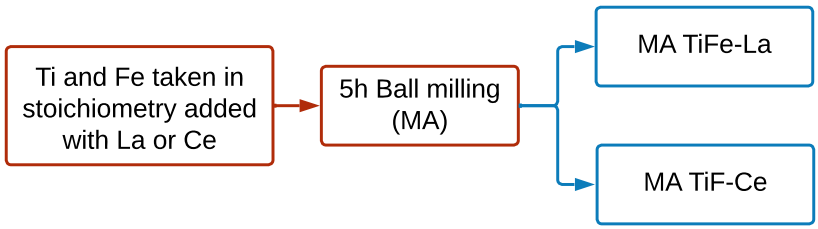

Figure 3.5: Flowchart showing process followed for synthesizing mechanically alloyed (MA TiFe-La and MA TiFe-Ce) samples.

The intermetallic compound $LaNi_5$ added TiFe was not synthesized by mechanical alloying only route. Because the long duration milling (5 h) will result in the formation of metastable phases, investigation on such samples will be difficult for two reasons. Synthesizing the same metastable phases is not possible. Consequently, the hydrogen sorption results will be non-reproducible.

Table 3.5: All the synthesized alloy combinations.

With La	**With Ce**	**With $LaNi_5$**	**For comparison**
MA TiFe-La	MA TiFe-Ce	-	MA TiFe
MM (La-MA TiFe)	MM (Ce-MA TiFe)	MM ($LaNi_5$-MA TiFe)	Cast TiFe
MM (La-cast TiFe)	MM (Ce-cast TiFe)	MM ($LaNi_5$-cast TiFe)	MM-cast TiFe

3.3 Alloy characterization

3.3.1 Scanning electron microscopy (SEM)

Scanning Electron Microscopy (SEM) is a type of electron microscopy that creates images by scanning a focused beam of electrons over the surface of a sample. The electrons interact with the atoms of the sample, producing signals such as secondary electrons (SE), back-scattered electrons (BSE), Auger electrons, etc. (refer to Fig. 3.6), which are then detected by suitable detectors to create an image of the surface topography and composition of the sample surface. Fig. 3.7 is a diagram showing the essential components of a scanning electron microscope:

- Electron source: A filament or an electron gun generates a beam of electrons.
- Column: The beam of electrons is then accelerated and focused into a small, tightly focused beam by the column.
- Sample stage: The sample is mounted on a stage and positioned in the path of the electron beam.

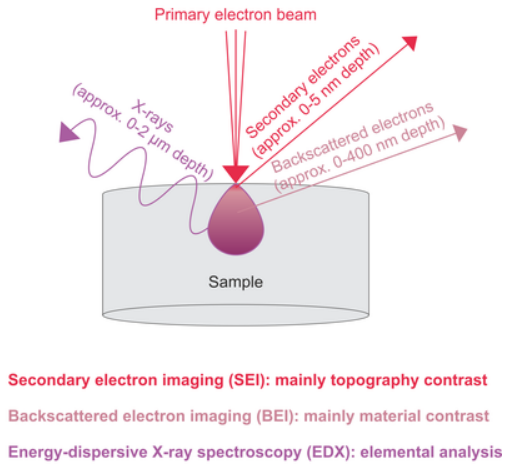

Figure 3.6: "Interaction volume" of electron beam configuration [127].

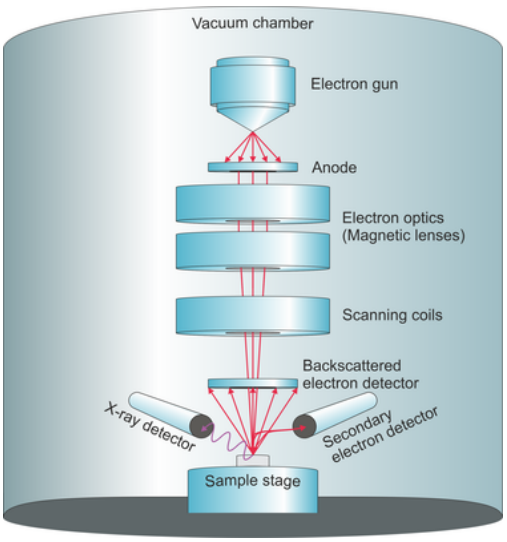

Figure 3.7: Schematic of a scanning electron microscope [128].

- Electron detector: The electron detector collects secondary electrons from the sample, which converts the electrons into an electrical signal.
- Image processing system: The electrical signal from the electron detector is processed by the image processing system to create an image of the sample surface.
- Monitor: The final image is displayed on a monitor for viewing.

SEM can observe the surface topography, composition, and morphology of a wide range of materials at high resolutions. It makes a valuable tool for material science, biology, and many other fields.

3.3.2 Energy dispersive X-ray spectroscopy (EDX)

Chemical composition analysis is often conducted using EDX. The process is commonly referred to as EDX or EDS. It is a fast and convenient way to obtain information on the elemental composition of a sample. The method relies on the principle of characteristic X-rays. Every element exhibits a distinctive X-ray emission spectrum due to its unique atomic structure. It is often used in combination with other analytical techniques, such as scanning electron microscopy (SEM) or transmission electron microscopy (TEM), to provide complementary information on the sample structure and composition. In addition to determining nominal bulk compositions, it can also map areas, lines, and points.

In the present study, scanning electron microscopy (SEM) and energy dispersive spectroscopy (EDX) was carried out using a Jeol JSM-5500 electron microscope (JEOL, Peabody, MA, USA) coupled with an Oxford EDX detector (Abingdon, UK). An image of the apparatus is shown in Fig. 3.8.

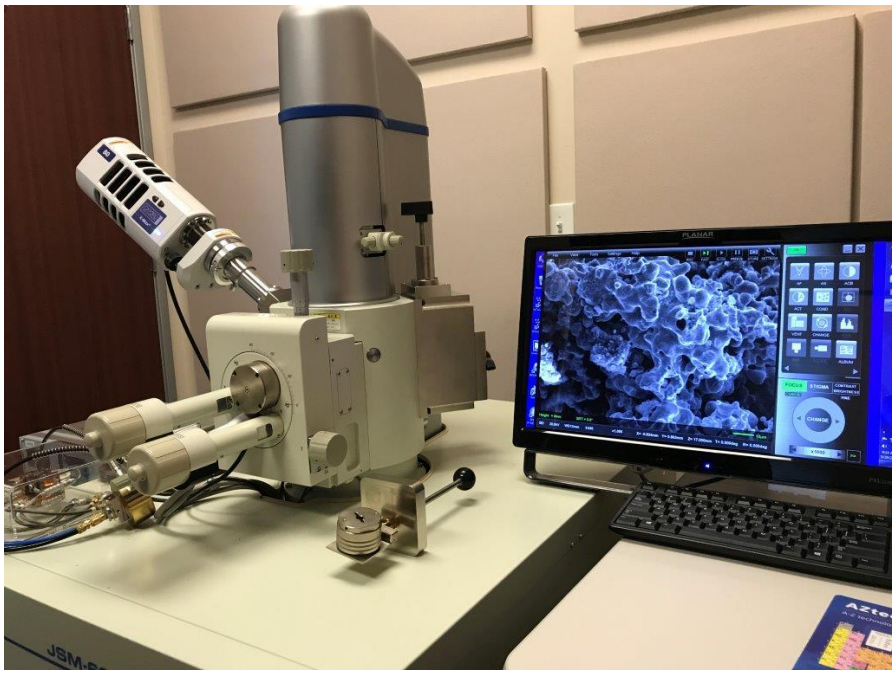

Figure 3.8: A representative image of the SEM apparatus used.

3.3.3 X-ray diffraction (XRD)

X-ray Diffraction (XRD) is a non-destructive analytical technique used to study the crystal structure of materials. The XRD is based on a fundamental principle called Bragg's law, which governs the constructive interference of X-rays scattered by atoms in a crystal lattice. It is expressed mathematically as:

$$n\lambda = 2d_{hkl} \sin \theta_{hkl} \tag{3.1}$$

where n is the order of the diffraction peak (i.e., 1st order, 2nd order, etc.), λ is the wavelength of the X-rays, d is the distance between adjacent planes of atoms in the crystal lattice (interplanar distance), and θ is the angle between the incident X-ray beam and the plane of atoms (Bragg angle).

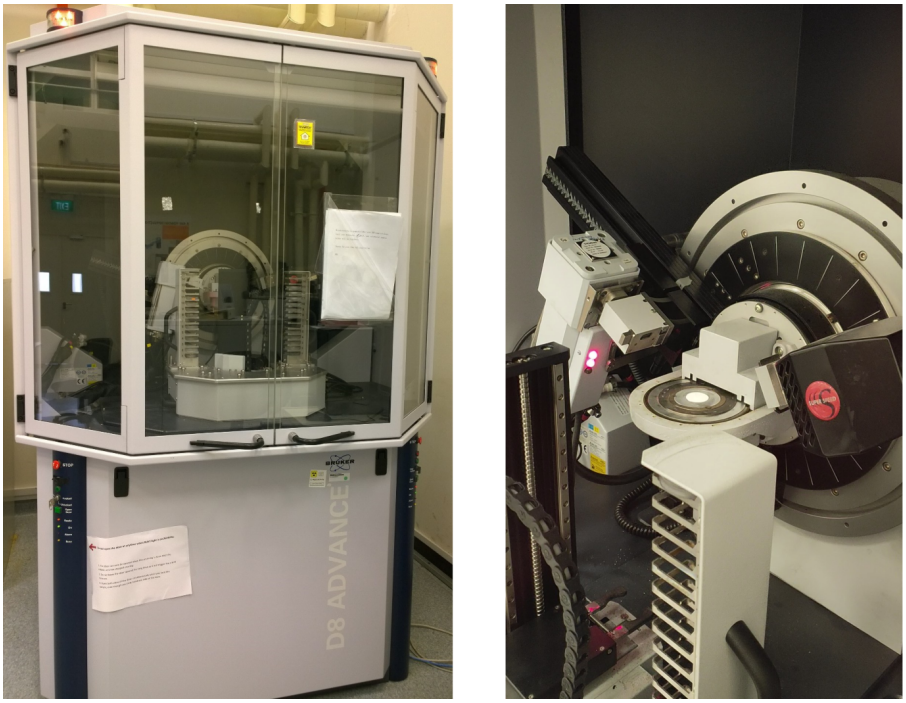

Figure 3.9: A representative image of a Bruker D8 Focus XRD machine.

The XRD experiment involves directing a beam of X-rays at a sample, which then scatters the X-rays in different directions. A detector detects scattered X-rays. According to Bragg's law, when atoms scatter X-rays of a specific wavelength in a crystal lattice at a particular angle, the path difference between the scattered rays reflected by adjacent planes of atoms will be an integer multiple of the wavelength. This results in constructive interference and produces a diffraction peak in the XRD pattern.

The intensity of the diffracted X-rays is plotted as a function of the diffraction angle in a graph known as a diffraction pattern. The diffraction pattern contains peaks at specific angles corresponding to the atoms' spacing in the crystal lattice. Bragg's law is important because it provides a simple way to determine the crystal structure parameters. By measuring the diffraction angles and using Bragg's law equation, one can obtain information about the crystal structure of materials, including the unit cell dimensions, relative amounts of different phases in the

sample, the position of atoms in the lattice, and other properties. This information can be used to identify unknown materials, study the effect of processing and other treatments on the crystal structure of the material.

X-ray diffraction (XRD) in the present study was registered using a Bruker D8 Focus apparatus (Bruker, Madison, WI, USA) with Cu Kα radiation (λ = 1.54 Å), a representative image of the same is shown in Fig. 3.9. The diffractometer is configured in reflection mode and Bragg-Brentano geometry. Using Topas software and the fundamental parameters approach, the crystal structure parameters were determined by performing Rietveld refinement on the diffraction patterns [129].

3.4 Hydrogen sorption measurements

Two methods, gravimetric and volumetric measurements, can be used to determine the hydrogen sorption in metal hydrides. A gravimetric technique utilizes the change in the mass of the sample following hydrogenation or de-hydrogenation to estimate the amount of hydrogen stored. A micro-balance with high precision is required in this method to measure the change in mass accurately. Several factors can affect measurement accuracy, including temperature changes, gas pressure changes, and mechanical vibrations, among others.

Volumetric measurement is based on Sievert's method sometimes called Sievert's technique. The apparatus comprises a calibrated volume known as standard cell interconnected to a sample volume (sample cell) through an isolation valve. A pressure transducer connected to measure the pressure. The schematic of a simplistic Sivert's apparatus is illustrated in Fig. 3.10.

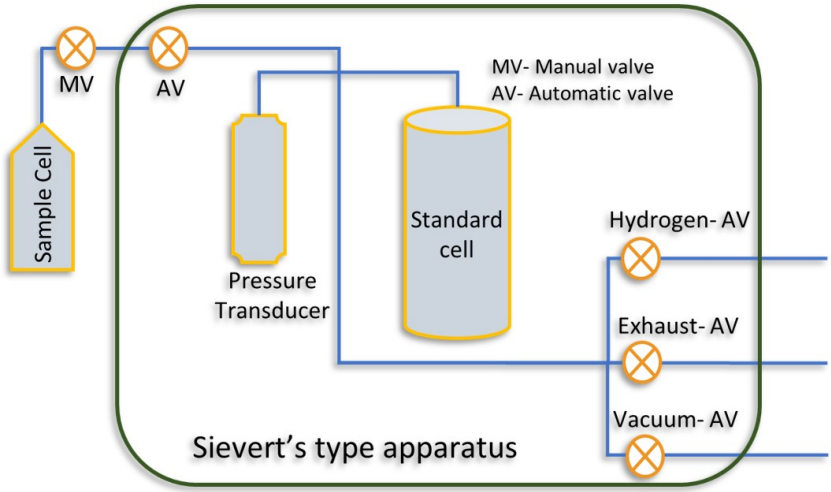

Figure 3.10: Schematic of a typical Sievert's apparatus.

In this type of apparatus, the change of pressure in a calibrated volume upon

hydrogenation/de-hydrogenation directly gives the amount of hydrogen evolved in the reaction. The number of gas molecules absorbed/desorbed can be determined by applying the real gas equation of state. In the present investigation the equation of state (EOS) used to determine the amount of hydrogen was Virial equation up to second-order Virial coefficients given by:

$$PV = nRT(1 + nB/V) \tag{3.2}$$
$$\Delta n = \frac{2V\Delta P}{RT(1 + nB/V)}$$

where P = Pressure of hydrogen at any given instant, ΔP = Pressure difference for which the absorption/desorption is determined, V= Hydrogen filled volume, n= Number of moles of hydrogen at pressure P, Δn = Number of moles of hydrogen absorbed/desorbed for ΔP, R = Universal gas constant, T = Absolute temperature of the system, B = Second order Virial coefficient, which varies with temperature.

3.4.1 Sievert's apparatus

Direct solid-gas reactions between bulk metals and hydrogen gases can lead to the formation of metal hydrides. Hydrogenation kinetics and pressure composition isotherms (PCT) were determined using an automatic Sievert's apparatus. The Sievert's apparatus used in the investigation included both a simplistic version and one with a differential pressure gauge. Fig. 3.11 depicts the simplistic Sievert's apparatus used. The Sievert's apparatus with a schematic of the valve operation for the differential pressure gauge is depicted in Fig. 3.12. The system displays essential components such as hydrogen reservoirs, different valves, and pressure and temperature sensors. Two tubing lines, designated for the sample and reference sample, are connected to the hydrogen supply via valves V3 and V4, respectively. Additionally, a vacuum pump, controlled by valve VS, is utilized for evacuation, while valve V2 facilitates the evacuation to atmospheric pressure. The differential gauge is employed to gauge the disparity between the sample and reference lines, which correlates with the quantity of hydrogen absorbed in the sample.

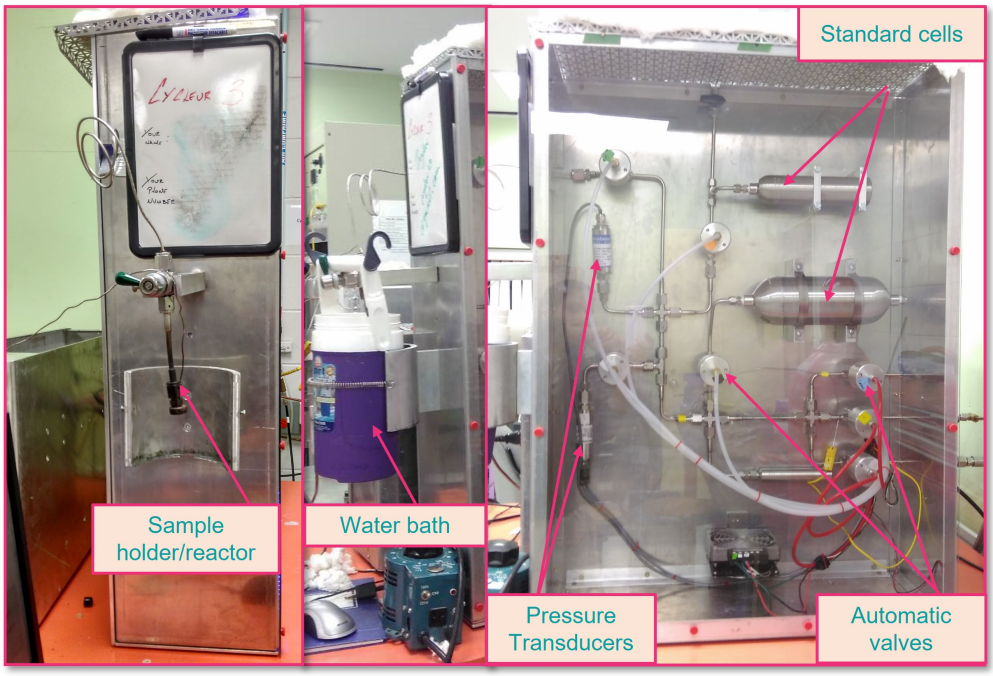

Figure 3.11: An automatic homemade Sievert's apparatus (Simplistic).

The equipment is operated using LabVIEW software, which offers extensive functionality. The homepage, illustrated in Fig. 3.13, presents numerous options for conducting different hydrogen absorption/desorption characterizations, including hydrogen kinetics, desorption kinetics, cycling, and PCT analyses.

3.4.2 Activation kinetics measurement

A few grams of the synthesized sample, without exposure to air, were inserted into the stainless-steel sample holder/reactor. Prior to commencing any hydrogen sorption measurements, the sample is subjected to a dynamic vacuum pressure of less than 10 kPa for a minimum of 1 hour. This procedure effectively removes any adsorbed gases associated with the sample's surface and facilitates a thorough cleaning process. All the hydrogenation measurements were carried out at room temperature in a water bath. The activation was performed under 20 bar for absorption and 0.05 bar (5 kPa) for desorption hydrogen pressure. The step-wise measurement of kinetics in the apparatus is outlined as follows:

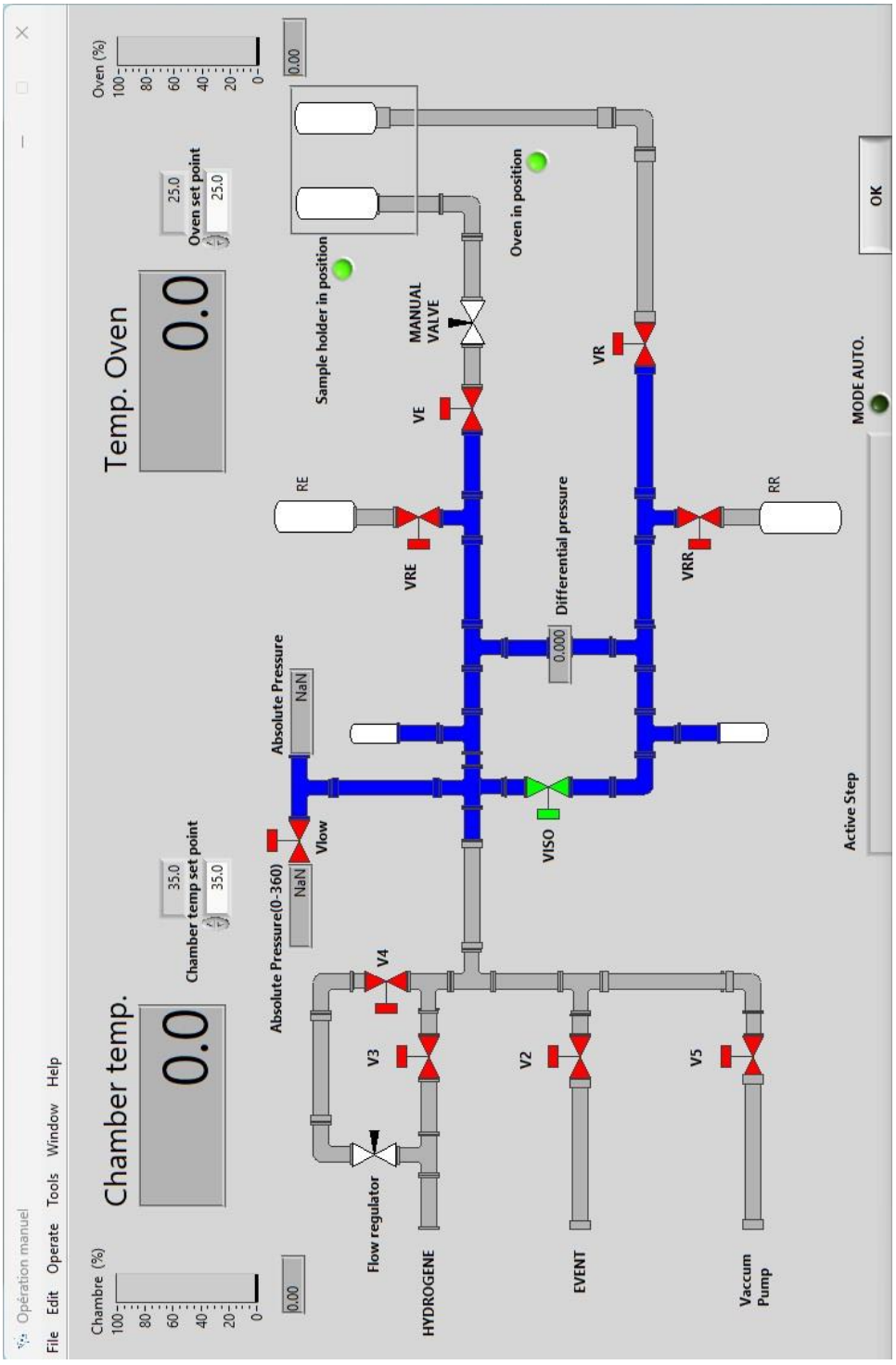

Figure 3.12: Valve operation interface (Differential pressure gauge based Sievert's apparatus).

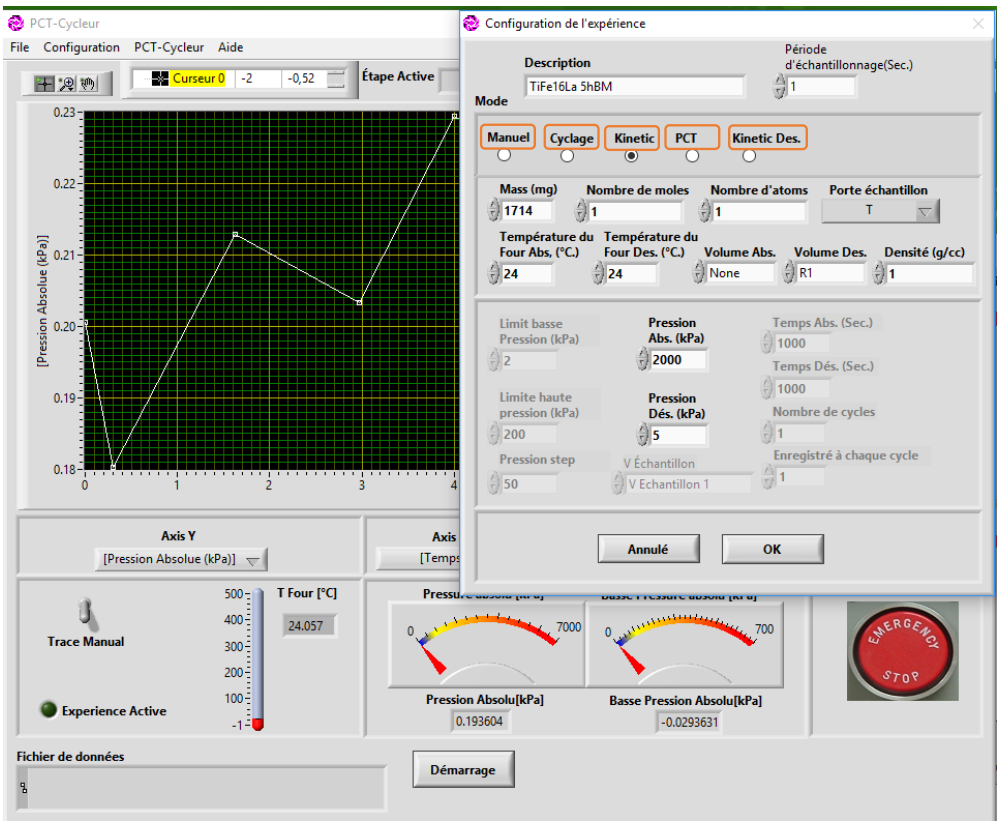

Figure 3.13: GUI of the homepage.

Procedure for dynamic vacuum:

1. Launch the software "PCT-Cycleur" on the computer connected to the system.

2. Select "Aide" in the GUI interface it will open the valve operation interface (Opération manuel). Ensure that all valves are closed (indicated by red).

3. Sequentially open valves V2, VISO, VR, and VE by clicking (changing their status to green) to initiate evacuation of system pressure, aiming to achieve a reading below 120 kPa on the absolute pressure gauge.

4. Once the absolute pressure gauge registers below 120 kPa, close valve V2 by clicking on it (changing its status to red).

5. Open valve V5 to create a vacuum in the tubing, and wait until the vacuum pressure displayed by the absolute high-pressure gauge drops below 10-5 kPa. This step ensures the removal of any foreign gases or air from the system, effectively cleaning the tubing.

6. Once the vacuum pressure falls below 5 kPa, close valve V5 by clicking on it (changing its status to red). Then, open valve V4 to pressurize the

system with hydrogen. Wait until the absolute high-pressure gauge reading approaches approximately 100 kPa.

7. Repeat steps 5 and 6 two more times to ensure thorough cleaning of the system, that is displacing any remaining foreign gases or air outside and effectively cleaning it.

8. Open valve V5 to create a vacuum inside the system.

9. When the absolute high-pressure gauge reading drops below 5 kPa, manually open valve MV to subject the sample powder to dynamic vacuum.

10. Record the time at which valve MV was opened and allow the sample to undergo dynamic vacuum for 1 hour.

11. After one hour, close valve MV and click on valve V5 to close it. At this point, the sample is prepared and ready for the experiment.

Auto kinetic mode procedure:

1. Navigate to the GUI homepage and select the "Kinetic" mode from the available options.

2. Input the experimental parameters, including the mass of the sample, absorption temperature, absorption pressure, and the desorption parameter details. Once all parameters have been entered, click on the "OK" button.

3. The system prompts the user to input a file name and specify the desired location for saving the measurements. Once the details are provided, the user clicks on the "OK" button to proceed with saving the data.

4. Initiate automatic measurements by selecting the start command "Demarrage."

5. A message box appears to confirm the closure of manual valve (MV). Proceed by manually closing the valve MV and click "Oui" (Yes) to confirm. Now the machine goes on automatic mode.

6. The machine evacuates the system to 30 kPa by opening the valves V5, VISO, VR, VE.

7. Now the program closes valves V5 and VE, while prompting to open Manual valve MV (while V2 and V3 remains already closed). Proceed by opening Manual valve MV and clicking "Oui".

8. Now the system opens valve V4 to fill hydrogen till P2 in the system through flow regulator. P2 is automatically calculated to pressurize the primary system volume V2 using the ideal gas equation at a constant temperature, ensuring that the set absorption pressure P1 (= 20 bar in this case) is achieved when valve VE is opened to commence absorption by releasing hydrogen into the sample holder volume.

9. Now the valve V4 closes and absorption temperature attainment duration starts. If the sample holder temperature falls within the tolerance limit of the absorption set temperature, the machine proceeds to step 11 immediately. Otherwise, an additional 60-second increment will be added until the sample holder temperature reaches the set value within the tolerance limit.

10. Valve VE opens leading to the interaction of hydrogen with the sample and hydrogen absorption starts. The experimental data, comprising parameters such as P2, P1, T, delta P, H wt%, etc., are continuously recorded over time at the default interval of 10 seconds, or at a user-defined interval if specified.

11. Wait until achieving activation followed by saturation of hydrogen capacity. Once the hydrogen capacity is saturated, click on the "Arrêt" or "Stop" command to halt the absorption measurements.

12. Next, the system automatically closes valve VE and opens valve V5 to establish the desorption pressure, which is set to 5 kPa in this instance.

13. The desorption process commences by opening valve VE, and experimental data, including parameters such as P2, P1, T, delta P, H wt%, etc., are recorded over time at the default interval of 10 seconds (or as set by the user).

14. Wait until the desorption process reaches saturation, then press the "Emergency stop" button to terminate the experiment. At this stage, the machine automatically closes all valves and returns the system to manual mode.

CHAPTER 4

Hydrogenation of TiFe alloy

There are various ways to synthesize alloys from elemental compositions, such as melting the elemental mixture in a furnace or mechanically milling them in a ball mill. Other techniques, such as physical vapor deposition, chemical vapor deposition, etc., could also be used. As explained earlier, ball milling (BM) can be used to synthesize alloy phases from the solid-state route. The present chapter deals with structural evolution and hydrogenation of TiFe alloy synthesized by ball milling from elemental compositions and arc melting.

4.1 Crystal structure

Fig. 4.1 shows the crystal structure evolution of the Ti-Fe mixture during ball milling. After 2.5 h of milling, the intensities of Ti and Fe peaks decreased, but there was no evidence of another phase. However, after 5 h of milling, the peaks of Ti and Fe disappeared, and new peaks appeared, corresponding to a single-phase TiFe structure. No noticeable peak intensities or broadness change was observed from 5 to 20 hours. The diffraction patterns of the samples ball milled for 5, 10, 15, and 20 h are essentially identical. This indicates that a milling duration of 5 h is adequate to complete the TiFe intermetallic formation under the present synthesis conditions. As the crystallite size is already at the nanoscale level, as will be seen later, there is no further reduction of the crystallite size, and the system reaches a steady state. Thus, the TiFe alloy synthesis is considered to be complete after 5 h of milling. The XRD of TiFe synthesized by arc melting (as-cast) is included in Fig. 4.1 for comparison with ball-milled samples. The high background at angles

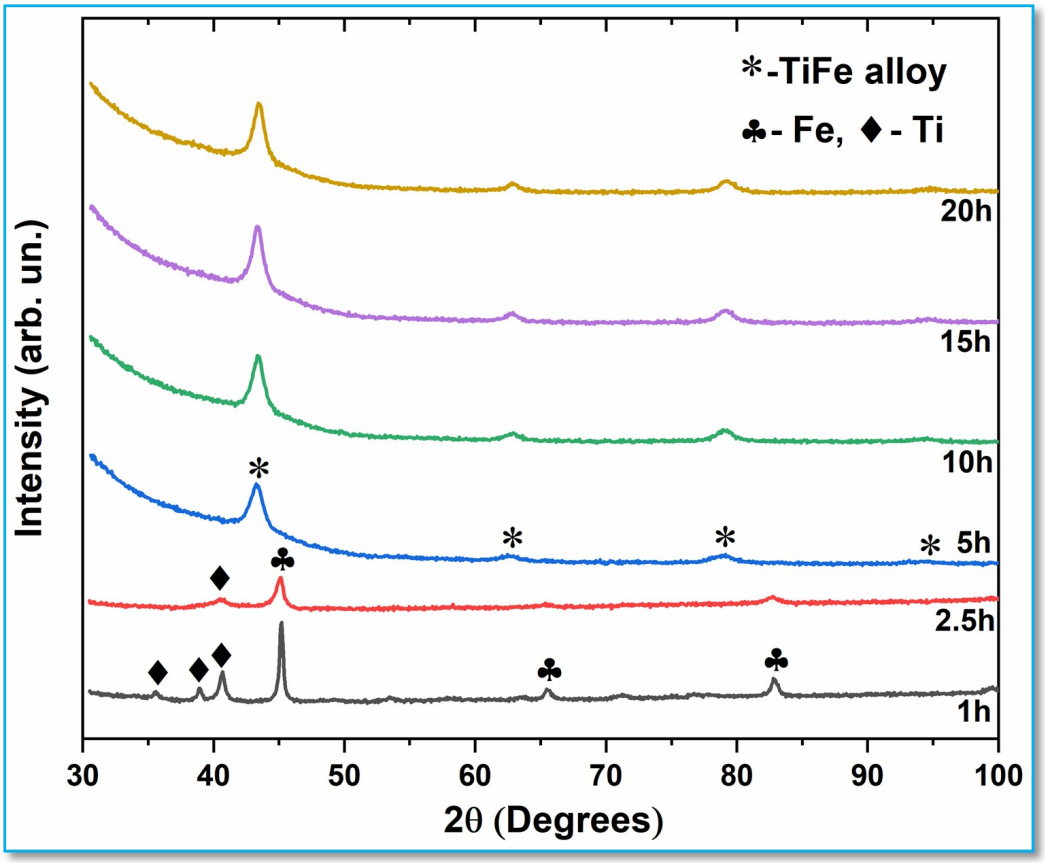

Figure 4.1: X-ray diffraction (XRD) patterns of the elemental powder mixtures Ti-Fe up to 20 hours of ball milling.

lower than 40° is due to the slit size. We used a relatively big slit size in order to have higher intensities of the Bragg peaks.

4.2 Hydrogen sorption kinetics

Fig. 4.2 depicts the first hydrogenation kinetics of cast TiFe and MA TiFe samples. Hydrogenation was carried out at room temperature with an initial hydrogenation pressure of 20 bar.

It can be observed that even after 12 hours, the as-cast TiFe did not activate under the present activation conditions. On the other hand, the mechanically alloyed (MA) TiFe shows extremely slow activation kinetics reaching just 0.23 wt % in 24 hours. It should be noted that no repeated heat treatment or high pressure was applied as suggested in the pioneering work of Reilly and Wiswall, which is effective, but the process is rigorous [1].

No or extremely slow activation kinetics at room temperature confirms the studies reported in the literatures [51, 52, 62, 67]. The following two chapters

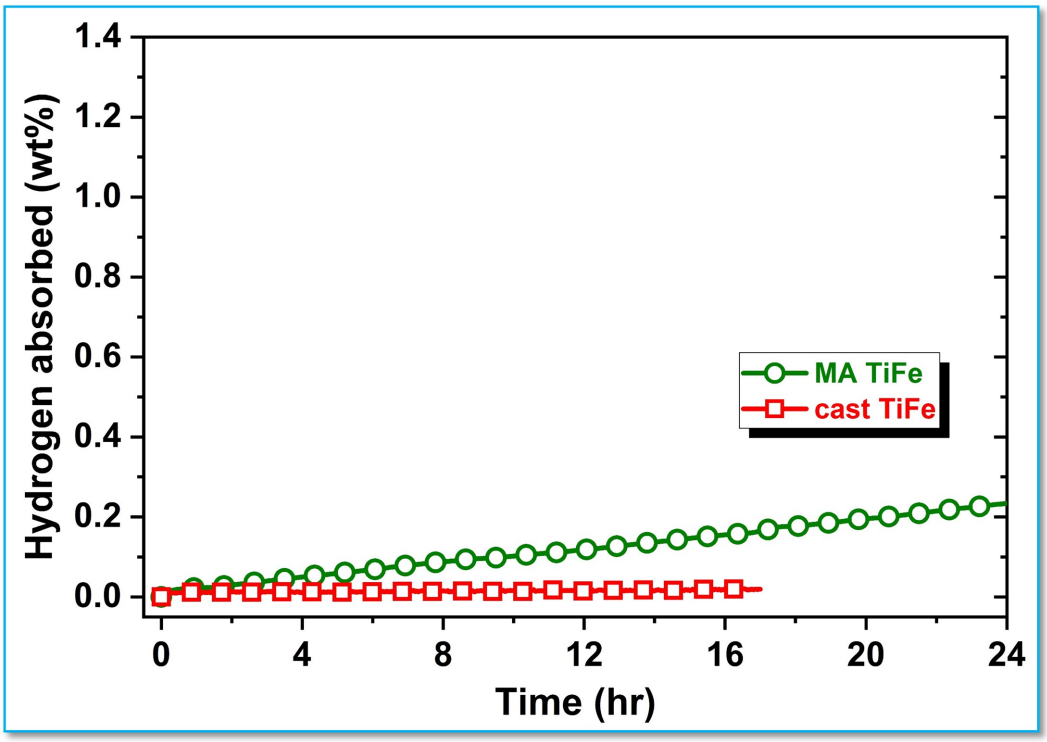

Figure 4.2: First hydrogenation behavior of cast TiFe and MA TiFe alloys.

will show how the already synthesized MA TiFe and cast TiFe behave when mechanically milled (MM) with the intermetallic $LaNi_5$ and rare earth additives. In addition to mixing additives to already synthesized TiFe by MM, we also investigated the Ti-Fe-La and Ti-Fe-Ce mixture mechanically alloyed, as presented in the last chapter.

CHAPTER 5

Hydrogenation of cast TiFe milled with additives

This chapter provides detailed insight into the effects of adding an intermetallic $LaNi_5$ and rare earth La and Ce on the hydrogen storage properties of cast TiFe alloy. The synthesis of cast TiFe with additives is described in section 3.2.2. For simplicity, the resultant alloys are denoted as MM (La-cast TiFe), MM (Ce-cast TiFe), and MM ($LaNi_5$-cast TiFe). The samples were then subjected to a hydrogen pressure of 20 bar at room temperature. Structural characterization before and after hydrogenation were carried out in order to gain insight into the structure-properties relation.

5.1 Morphology and microstructure

Fig. 5.1 shows the morphology of as-synthesized MA TiFe, cast TiFe, and cast TiFe added with additives. The as-cast TiFe has a flat surface and sharp edges resulting from crushing with the mortar and pestle. Those sharp edges became rounded through mechanical milling in the MM-cast TiFe sample. Milling with an additive (La, Ce, or $LaNi_5$) produces a much smaller particle size. Mechanical alloying (MA) of Ti and Fe powders resulted in fine powder. Fig. 5.2 shows the backscattered electron (BSE) image of TiFe with additives and the corresponding EDX color mapping. In color mapping, bright area shows high abundance of the element while dark area represents low abundance. The color mapping reveals that Ti and Fe are evenly distributed, while the additive is primarily in the bright regions.

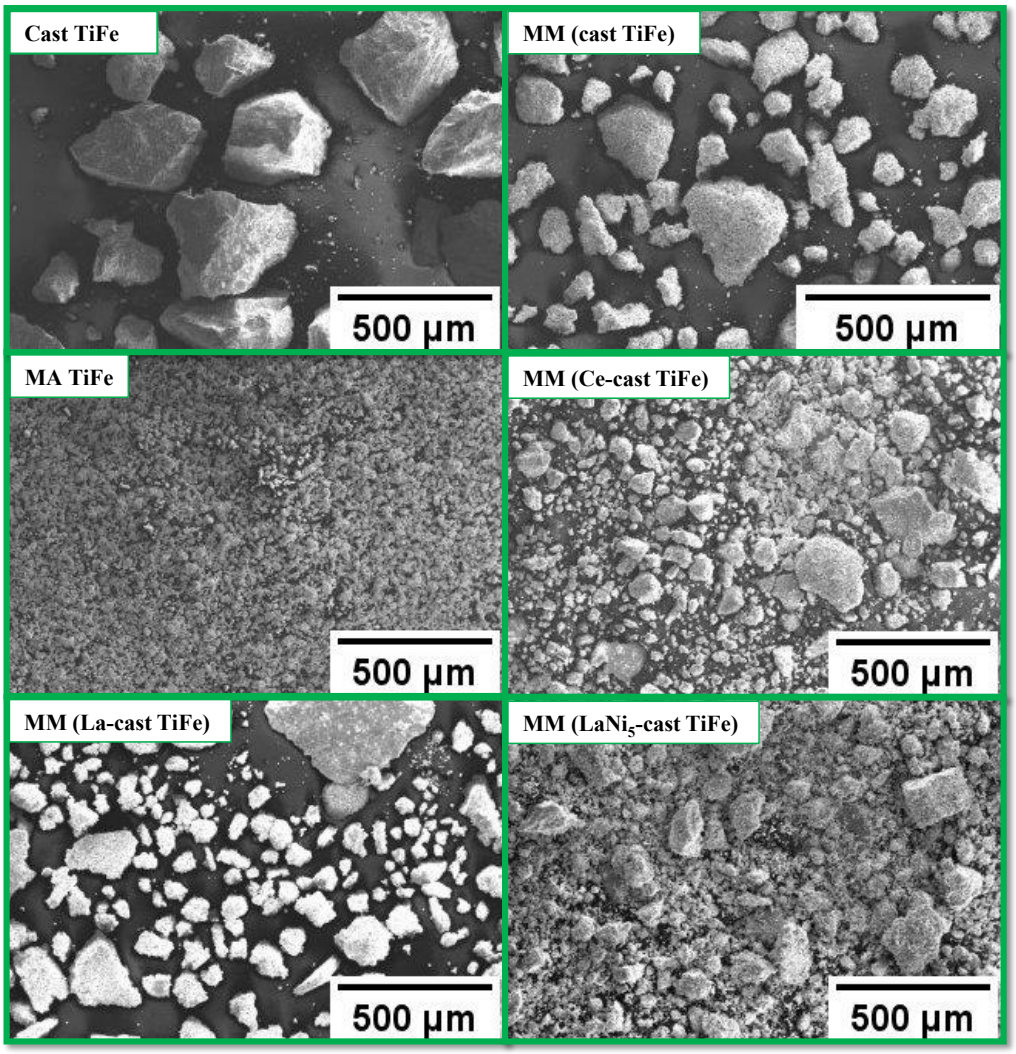

Figure 5.1: SEM morphology of cast TiFe, MM-cast TiFe, MA TiFe, and cast TiFe with additives in an as-synthesized state.

Table 5.1 presents the chemical composition of the regions determined using Energy Dispersive Spectroscopy (EDX). For all samples, the bulk abundance of Ti is slightly higher than the nominal value, while the iron abundance is lower. The abundance of the additive is somewhat higher. As the relative abundance of La and Ni is very close to the stoichiometry $LaNi_5$, we could exclude a systematic error. The reason for this situation is unclear, but an investigation with different milling times may provide some clues for the mechanism. The additives are primarily in the bright region. The Ti and Fe in these regions have the same atomic abundance. Therefore, we may conclude that what is seen is the TiFe phase. It should also be mentioned that for the $LaNi_5$ additive, the ratio of La/Ni in the bright region is also close to the stoichiometry $LaNi_5$. This means that the additive did not decompose, and no La-Ni-Ti-Fe phase has been formed.

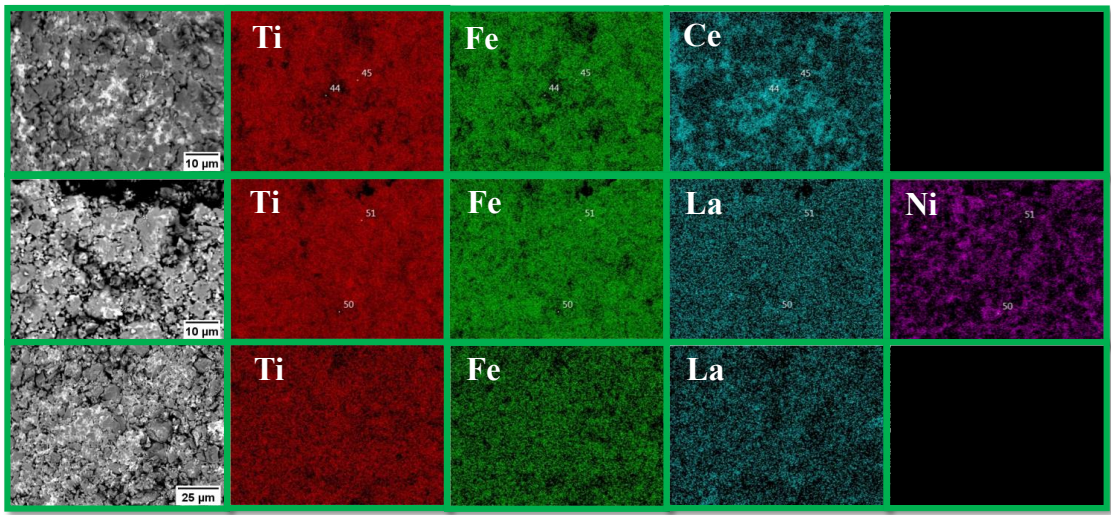

Figure 5.2: BSE image of cast TiFe with additives in an as-synthesized state along with the EDX color mapping. The bright area shows a high abundance of the element.

Table 5.1: EDX chemical composition of as-synthesized cast TiFe with additives in at%. The uncertainty on the measurement is ±1 at%.

Samples	Elements	Nominal composition	Bulk composition (Surface analysis)	Grey region (Point analysis)	Bright region (Point analysis)
MM (Ce-cast TiFe)	Ti	46.7	47.8	50.1	13.0
	Fe	46.7	45.1	48.0	12.0
	Ce	06.6	7.0	1.9	75.0
MM ($LaNi_5$-cast TiFe)	Ti	44.0	43.5	49.1	7.8
	Fe	44.0	40.2	47.7	8.4
	La	02.0	2.6	0.4	14.2
	Ni	10.2	13.8	2.8	69.7
MM (La-cast TiFe)	Ti	46.7	47.6	49.7	15.8
	Fe	46.7	43.8	48.8	11.1
	La	06.6	8.6	1.9	73.1

Fig. 5.3 shows the microstructure of TiFe with additives in an as-synthesized state. The alloys consist of two distinct regions, as evidenced by the backscattered electron images: the primary matrix grey region and a bright region. This means the additives are located in small areas over the large TiFe region because the bright part is made of additives. The area fraction of the bright region was measured using ImageJ software employing global thresholding. The randomly selected image offers an adequate field of view to represent the bulk value accurately. The calculated area fraction is presented in Table 5.2. It can be observed that the area fraction calculated from imageJ is slightly higher than the nominal value, but the difference is insignificant.

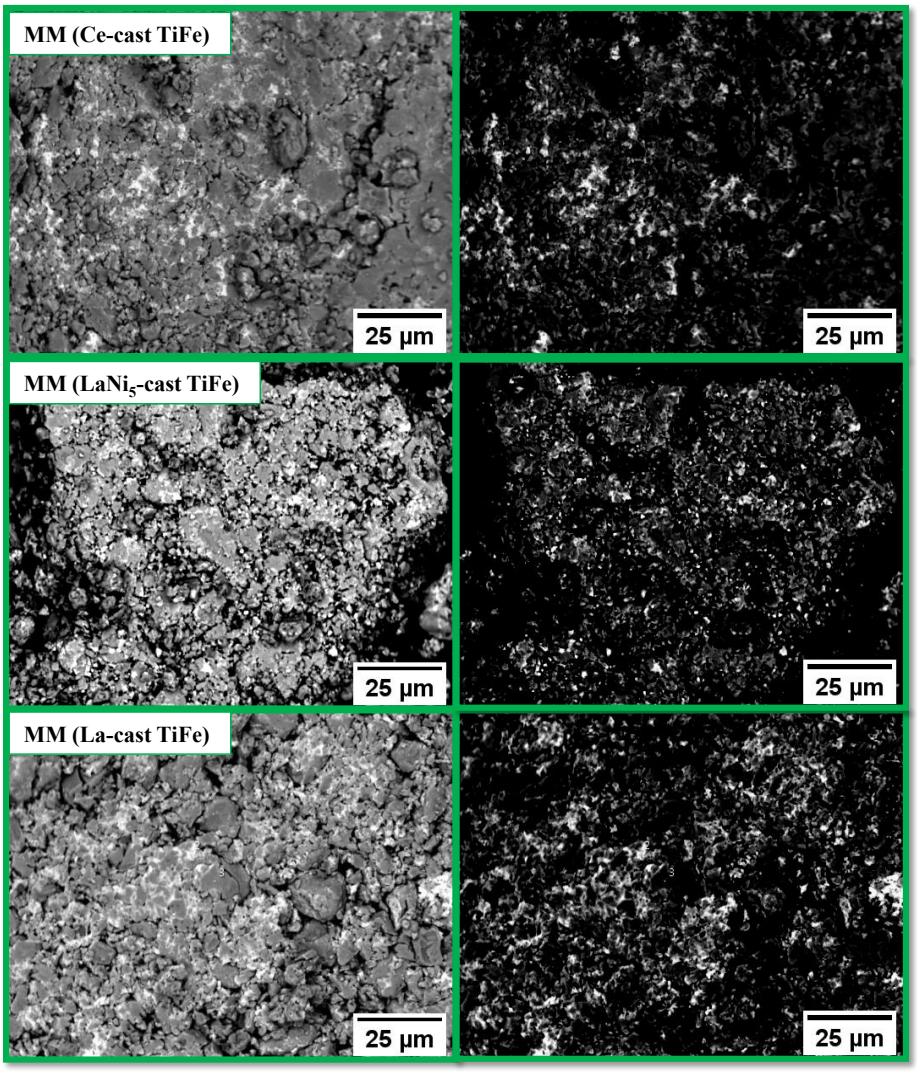

Figure 5.3: BSE images of cast TiFe with additives along with the bright region marked by isoData thresholding using ImageJ software.

Table 5.2: Area fraction of the grey regions (TiFe) as measured from the ImageJ software. The uncertainty on the value is ± 1%.

Samples	**Nominal wt% of TiFe**	**Nominal area % of TiFe**	**Area % of TiFe calculated from ImageJ**
MM (Ce-cast TiFe)	84	85	86
MM ($LaNi_5$-cast TiFe)	84	87	88
MM (La-cast TiFe)	84	83	85

5.2 Crystal structure

Fig. 5.4 shows the samples' X-ray powder diffraction patterns in the as-synthesized state. All the ball-milled alloys show broad peaks, in contrast to the as-cast TiFe pattern. The broadening of the peaks signifies a reduction of crystallite size and/or the presence of microstrains. The presence of the TiFe phase (CsCl-type structure, space group Pm-3m) is confirmed for all samples. In the case of MM (La-cast TiFe), small peaks belonging to a high-pressure La phase (β-La, space group Fm-3m) are seen. This is possible as it is well known that high energy-milling could produce metastable phases [130]. The MM (Ce-cast TiFe) pattern has peaks indicating the presence of cerium oxide rather than Ce (cerianite, CeO_2, fluorite-type structure, space group Fm-3m). The MM ($LaNi_5$-cast TiFe) diffraction pattern shows the peaks of $LaNi_5$ (space group P6/mmm).

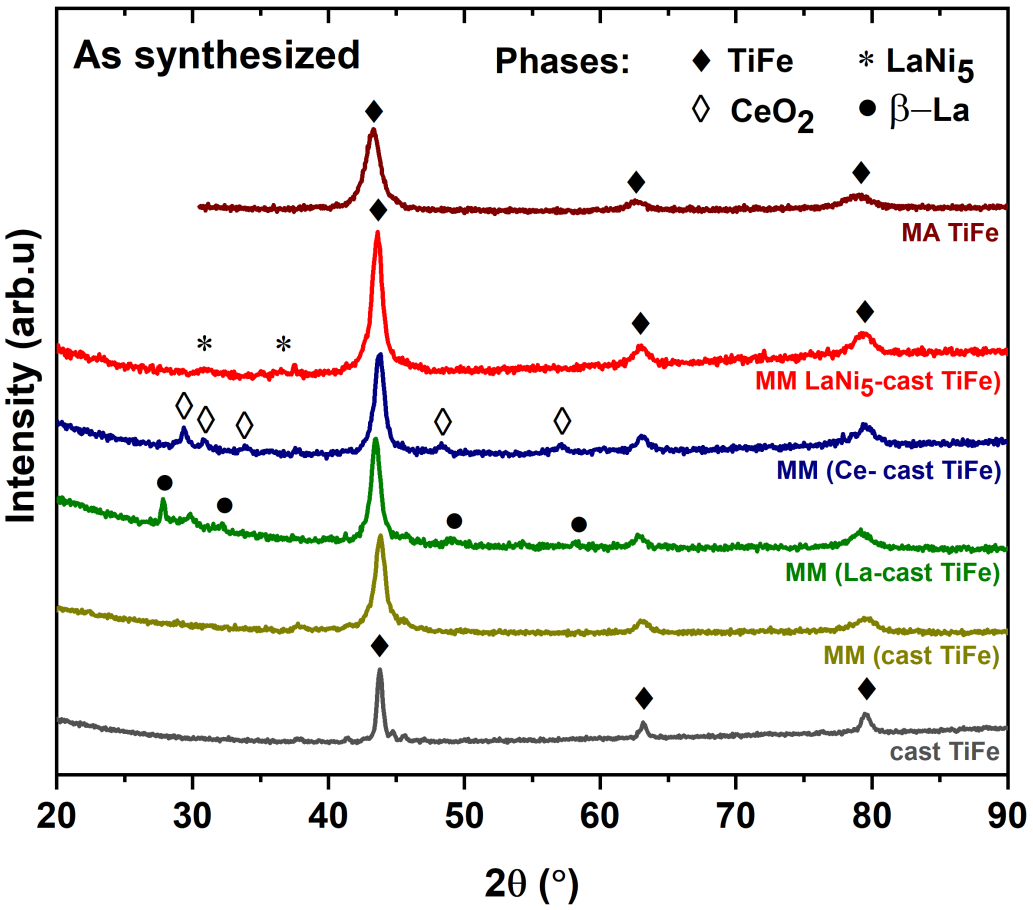

Figure 5.4: XRD patterns of cast TiFe, MM-cast TiFe, MA TiFe, and cast TiFe with additives in an as-synthesized state.

Rietveld refinement was performed on all the X-ray diffraction patterns to determine the phase composition and crystal structure parameters. They are presented in Table 5.3. The phase abundances of additives are systematically smaller

than the nominal values. This may be due to the broad peaks that could not be adequately deconvoluted from the background. The mechanical deformation by ball milling reduces the crystallite size of the TiFe phase. Except for La, the crystallite size of the additives CeO_2 and $LaNi_5$ are below 10 nm and are comparable to the main phase TiFe. Besides the reduction of crystallite size, milling has the effect of reducing microstrains.

Table 5.3: The crystal structure parameters of the cast TiFe, MM-cast TiFe, MA TiFe, and cast TiFe with additives in an as-synthesized state. Numbers in parentheses represent errors on the last significant digit.

Samples	Phase	Phase abundance (wt%)	Lattice parameters (Å)	Cell volume (Å^3)	Crystallite size (nm)	Microstrain (%)
As-cast TiFe	TiFe	100	2.9781(6)	26.41(1)	16.7(7)	0.32(5)
MM-cast TiFe	TiFe	100	2.9809(1)	26.49(3)	6.15(1)	0.10(3)
MA TiFe	TiFe	100	2.9839(1)	26.57(4)	5.39(1)	1.32(7)
MM (Ce-cast TiFe)	TiFe	90.0(8)	2.9891(1)	26.71(3)	8.5(3)	0.96(8)
	CeO_2	10.0(8)	5.4464(5)	161.56(4)	6.9(6)	-
MM ($LaNi_5$ -cast TiFe)	TiFe	90.5(2)	2.9796(1)	26.45(4)	7.1(3)	0.57(1)
	$LaNi_5$	9.5(2)	a = 4.978(1) c = 4.020(1)	86.3(5)	6.2(2)	-
MM (La-cast TiFe)	TiFe	91.0(5)	2.9831(1)	26.55(4)	9.2(4)	0.85(9)
	β-La	09.0(4)	5.669(4)	182.2(4)	32(6)	-

5.3 Hydrogen sorption kinetics

Fig. 5.5 shows the first hydrogenation kinetics (activation) of samples at room temperature with an initial hydrogen pressure of 20 bar. The cast TiFe synthesized by arc melting did not activate under these experimental conditions. However, the same alloy, mechanically milled (MM-cast TiFe), gets hydrogenated with an absorption capacity of 1.0 wt%. The remarkable improvement in the activation of MM-cast TiFe can be attributed to the reduction of crystallite size and addition of defects due to milling. With additives, the hydrogenation is more complete and faster when it is Ce reaching 1.2 wt% in less than 6 h. The La addition to the cast TiFe enabled activation, albeit with slower kinetics and reduced capacity absorbing 0.9 wt% in 12 h. Adding $LaNi_5$ to TiFe gave fast activation kinetics but with a slightly lower capacity of 0.9 wt% in less than 6 h. Interestingly, mechanical milling with or without the additives resulted in the activation of cast TiFe alloy. Except for the MM (La-cast TiFe), the first hydrogenation kinetics of all the mechanically milled (cast TiFe, Ce-cast TiFe, and $LaNi_5$-cast TiFe) samples are fast. The enhancement in activation kinetics of MM (cast TiFe, Ce-cast TiFe, and $LaNi_5$-cast TiFe) samples are comparable to the studies reported on Zr, Zr_7Ni_{10}, and Hf as additive [51, 52, 62, 67].

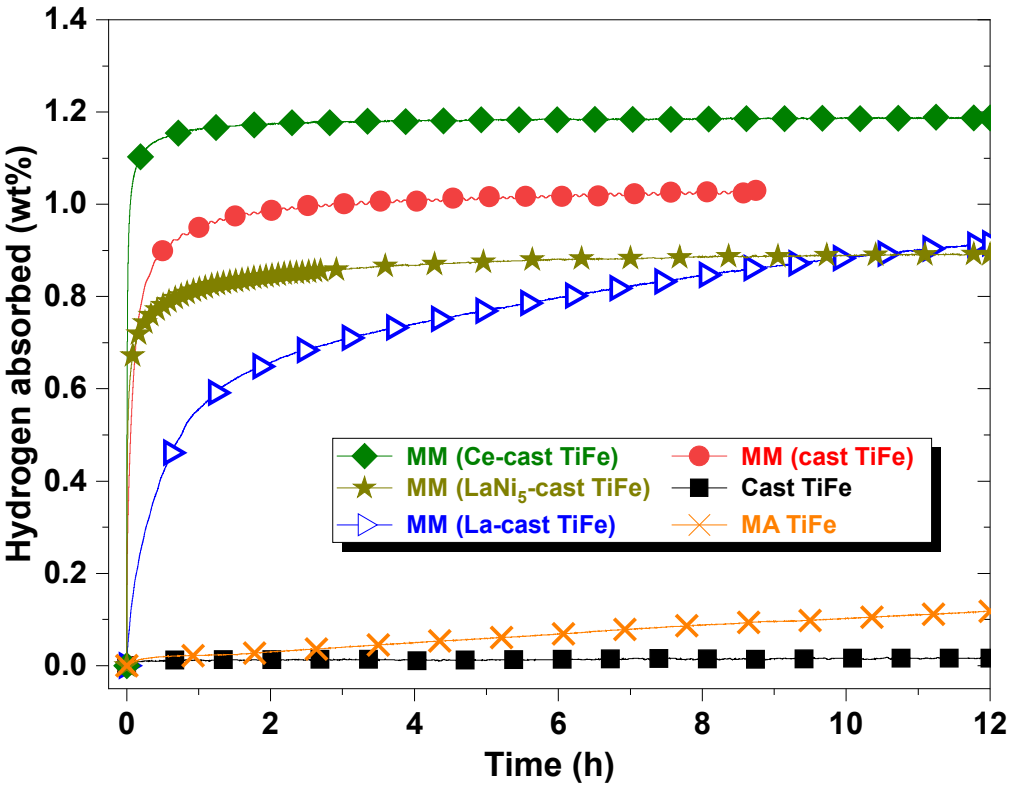

Figure 5.5: Activation of pure TiFe and cast TiFe with additives.

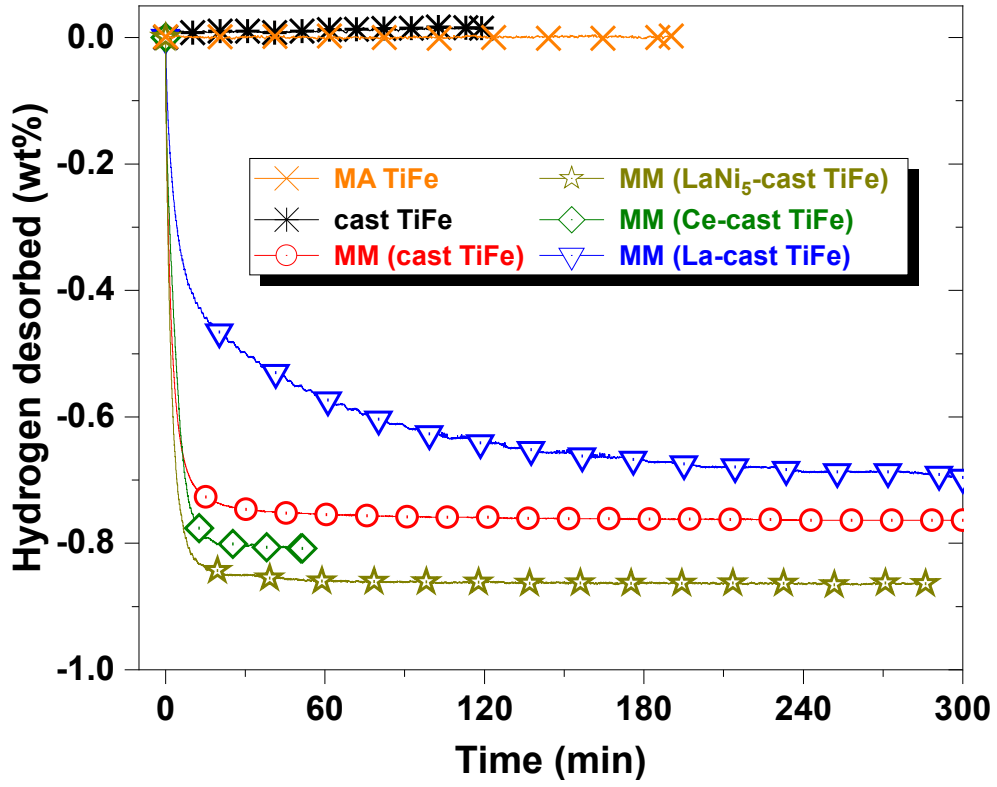

Figure 5.6: Desorption kinetics of MM-cast TiFe and cast TiFe with additives.

Fig. 5.6 illustrates the hydrogen desorption kinetics with an initial hydrogen pressure of 5 kPa at room temperature. Interestingly, the $LaNi_5$ added TiFe sample desorbed totally, and there was a negligible loss in the reversible desorption capacity. The Ce added TiFe, which showed a maximum absorption capacity of 1.2 wt%, desorbed only 0.8 wt%. Incomplete desorption was also observed in mechanically milled cast TiFe. The X-ray diffraction of the de-hydrided samples was carried out to understand the loss of capacity.

5.4 Crystal structure of de-hydrided state

Fig. 5.7 shows the de-hydrided samples' X-ray powder diffraction patterns. TiFe peaks in all the samples show that the main phase was completely de-hydrided. In addition to TiFe peaks, MM (Ce-cast TiFe) and MM ($LaNi_5$-cast TiFe) compounds show peaks of CeO_2 and $LaNi_5$, respectively. The diffraction pattern of the MM (La-cast TiFe) sample shows peaks of TiFe and LaH_3. LaH_3 does not desorb even at 250 °C, as reported by Zhao *et al.* [131], though a transition from LaH_3 to $LaH_{2.3}$ was observed at 440 °C in a study by Zhu *et al.* [132]. Thus, LaH_3 being stable, did not desorb at the present experimental conditions. Considering that the theoretical hydrogen capacity of LaH_3 is 2.1 wt%, for a 10 wt% fraction calculated from Rietveld, it will contribute to 0.21 wt% of the total capacity registered in the activation. This value agrees well with the difference between absorption (0.9 wt%) and desorption (0.7 wt%). The reason for incomplete desorption in samples MM-cast TiFe and MM (Ce-cast TiFe) are still unclear.

The crystal structure parameters of the activated samples were evaluated by the Rietveld refinement of the diffraction patterns, and the results are presented in Table 5.4. The deconvolution of the secondary phase abundance in the de-hydrided state is difficult because of the low abundance of the secondary phase and the important peak broadness. The crystal structure parameters are similar to the ones obtained for the as-synthesized samples except for the microstrain values and the crystallite size of LaH_3 compared to La. After hydrogenation, the microstrain significantly changed for the MM (La-cast TiFe) and MM ($LaNi_5$-cast TiFe) samples. Upon hydrogenation there is a swelling of the unit cell and thus create decrepitation and/or some additional internal stress. When the sample is dehydrided this stress is released, and we see a reduction of microstrain. Conducting an in-situ XRD or synchrotron XRD during sorption could provide valuable insights into the mechanisms behind the incomplete desorption observed in MM-cast TiFe and MM (Ce-cast TiFe). Incomplete desorption is probably the reason why microstructure did not change for the MM-cast TiFe and MM (Ce-cast TiFe).

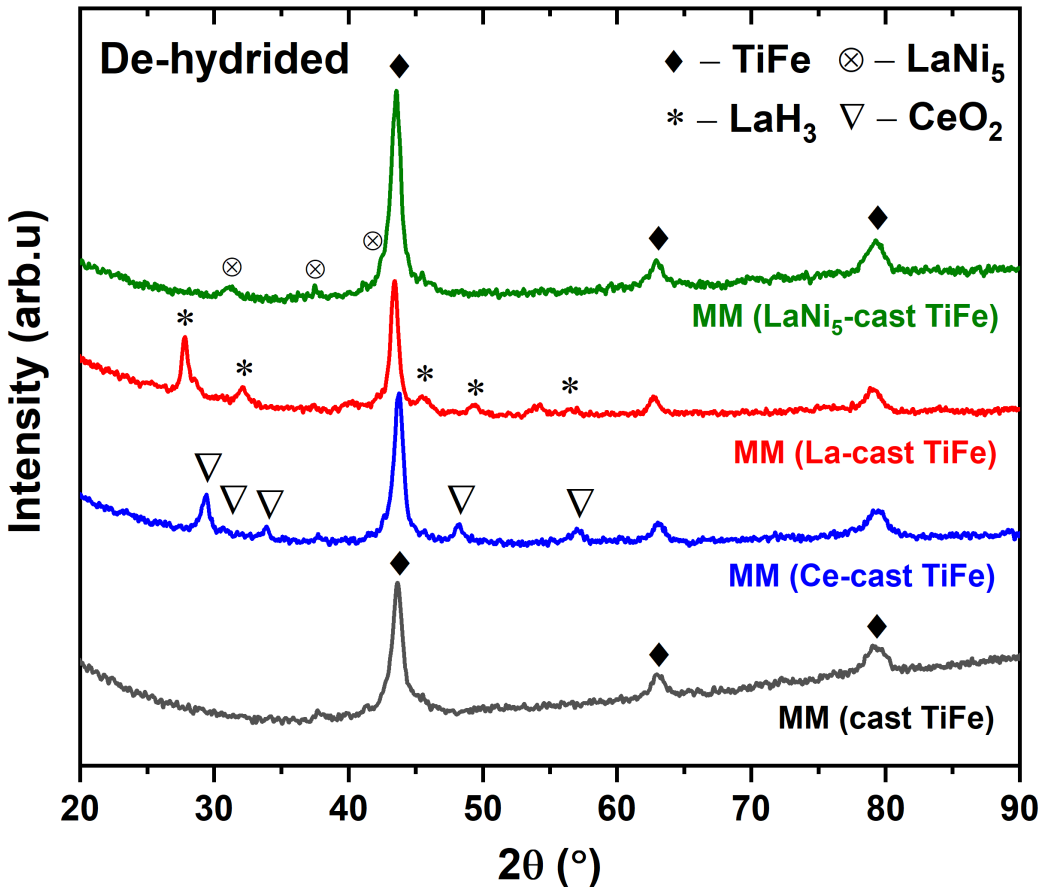

Figure 5.7: XRD patterns of MM-cast TiFe and cast TiFe with additives after de-hydrogenation.

Table 5.4: The crystal structure parameters of the MM-cast TiFe and cast TiFe with additives after de-hydrogenation. Numbers in parentheses represent errors on the last significant digit.

De-hydrided	Phase	Phase abundance (wt%)	Lattice parameters (Å)	Cell volume (Å^3)	Crystallite size (nm)	Microstrain (%)
MM-cast TiFe	TiFe	100	2.9861(2)	26.63(4)	5.8(2)	0.10(5)
MM (Ce-cast TiFe)	TiFe	87.6(1)	2.9902(7)	26.74(2)	8.2(3)	0.73(9)
	CeO_2	12.4(1)	5.4464(1)	161.56(1)	9.1(6)	-
MM ($LaNi_5$-cast TiFe)	TiFe	90.5(2)	2.9789(1)	26.44(4)	6.8(3)	-
	$LaNi_5$	9.5(2)	a = 4.967(1)	85.1(5)	5.9(2)	-
			c = 3.984(1)			
MM (La-cast TiFe)	TiFe	90(2)	2.9895(1)	26.72(3)	9.1(4)	0.10(3)
	LaH_3	10(2)	5.680(4)	183.3(3)	10.1(5)	-

Findings of this chapter are compiled in Table 5.5 to compare with the literature reported results presented in Tables 2.1 and 2.2. The activation kinetics of MM (cast TiFe, Ce-cast TiFe, and $LaNi_5$-cast TiFe) samples show enhancements that are comparable to those observed in studies with Zr, Hf, and Cr as additives [52, 62, 67, 71, 72]. However, under the current experimental conditions, the activation of the MM (La-cast TiFe) sample appears relatively slower. Yet, it shares

similarities with the findings reported by Gosselin et al. for yttrium-added TiFe alloy [69] and Zeaiter et al. for Mn-added TiFe [123].

Table 5.5: Findings of this chapter compiled to compare with the literature-reported results.

Synthesis process	**Samples**	**Absorption (wt%) @ RT & 20 bar**	**Desorption (wt%) @ RT & 5 kPa**
TiFe by arc melting	MM (Ce-cast TiFe)	1.2 (1 h)	0.80 (1 h)
followed by 15 min	MM (La-cast TiFe)	1.0 (20 h)	0.70 (5 h)
mechanical milling	MM ($LaNi_5$-cast TiFe)	0.9 (6 h)	0.87 (1 h)
with additives	MM-cast TiFe	1.0 (3 h)	0.77 (1 h)

5.5 Summary

The effect of intermetallic $LaNi_5$ and rare earth La and Ce on the hydrogen storage properties of TiFe alloy has been investigated. The addition was performed through short-duration ball milling to maintain the composite nature of the materials. Based on the findings of this study, the following conclusions can be drawn:

- The short milling duration facilitated the composite formation of TiFe with the additives without resulting in the formation of new phases.
- SEM revealed the presence of two distinct regions in the alloys: the primary matrix TiFe region and a secondary region containing the additives.
- The inclusion of additives to TiFe led to a significant improvement in the first hydrogenation.
- The hydrogenation was more complete when the additive was Ce and completely reversible when the additive was $LaNi_5$.
- The kinetics of TiFe with lanthanum was slow, and the formation of stable LaH_3 was observed.
- Mechanical milling with or without the additives resulted in the activation of the TiFe alloy.

CHAPTER 6

Hydrogenation of MA TiFe milled with additives

The present chapter unfolds the milling effect in conjunction with additives La and Ce and an intermetallic $LaNi_5$ on the hydrogen storage properties of pre-synthesized TiFe alloy. The TiFe alloy was pre-synthesized by the mechanical alloying (MA) process and the synthesized TiFe was then milled with the additive for short-duration of 15 minutes. The synthesis process is described in detail in section 3.2.3. For simplicity, the resultant alloys are denoted as MM (La-MA TiFe), MM (Ce-MA TiFe), and MM ($LaNi_5$-MA TiFe). The samples were then subjected to a hydrogen pressure of 20 bar at room temperature.

6.1 Microstructure

Fig. 6.1 shows the morphology of MA TiFe with additives in an as-synthesized. The MA TiFe alloy with additives subjected to mechanical milling display irregularly shaped plate-like structures with an average particle size below 150 μm. Fig. 6.2 presents back-scattered electron (BSE) images along with energy-dispersive X-ray spectroscopy (EDX) color mapping of the TiFe alloy with additives. The EDX confirms the presence of all the elements in the samples. Notably, it is observed from the color mapping that the additive is not uniformly distributed throughout the sample. Instead, it is segregated as indicated by the presence of distinct bright region similar to what was observed in the previous chapter.

The bulk as well as point elemental composition mapping is carried out by EDX and is presented in Table 6.1. As measured, the Ti and Fe composition is

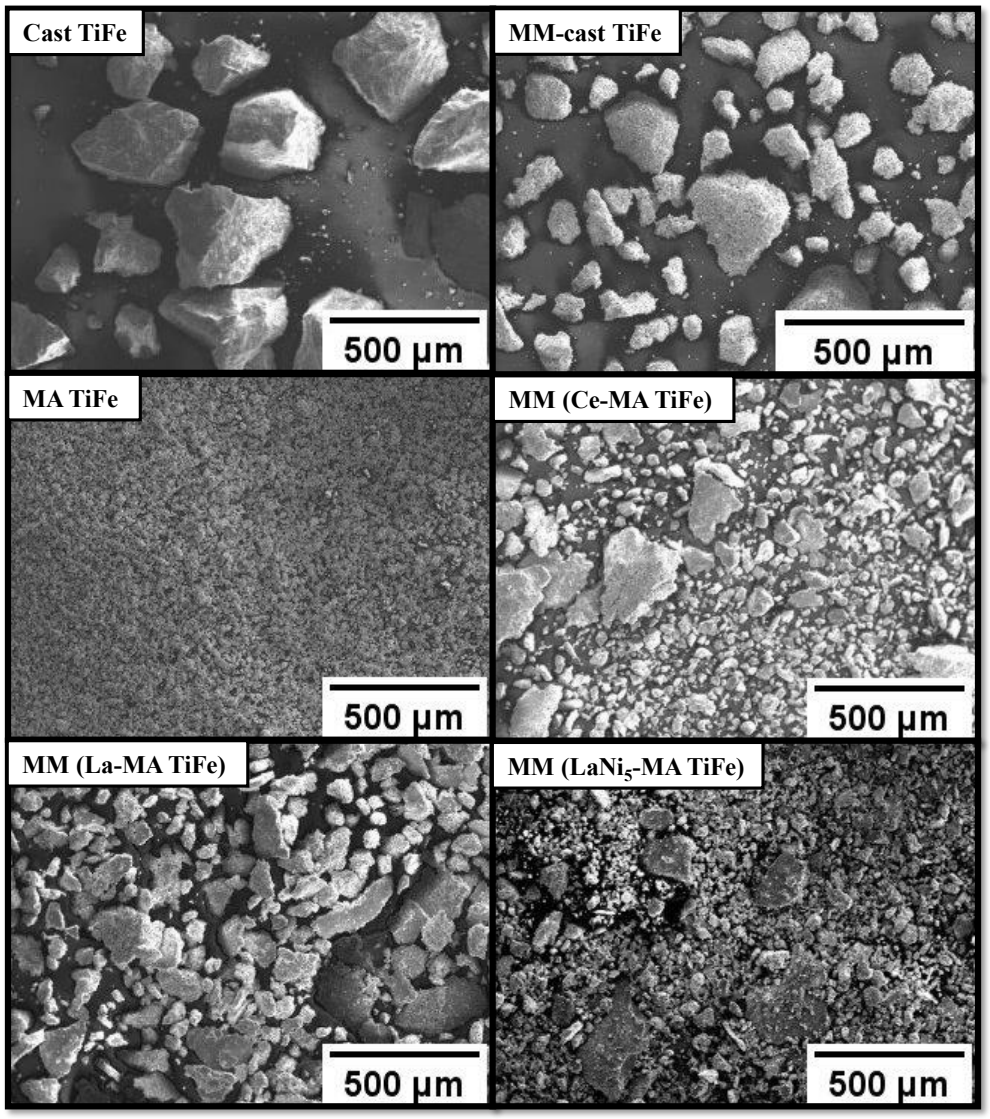

Figure 6.1: SEM morphology of pure TiFe and MA TiFe with additives in an as-synthesized state.

Table 6.1: EDX chemical composition of as-synthesized MA TiFe with additives in at%. The uncertainty on the measurement is ±1 at%.

Samples	Elements	Nominal composition	Bulk composition (Surface analysis)	Grey region (Point analysis)	Bright region (Point analysis)
MM (Ce-MA TiFe)	Ti	46.7	47.8	49.9	3.9
	Fe	46.7	47.2	49.4	2.6
	Ce	6.6	5.0	0.7	93.5
MM ($LaNi_5$-MA TiFe)	Ti	44.0	40.9	49.8	8.4
	Fe	44.0	39.1	49.2	8.4
	La	2.0	3.5	0.3	13.9
	Ni	10.2	16.5	0.7	69.3
MM (La-MA TiFe)	Ti	46.7	45.6	50.2	4.2
	Fe	46.7	44.4	49.6	2.7
	La	6.6	10.0	0.2	93.1

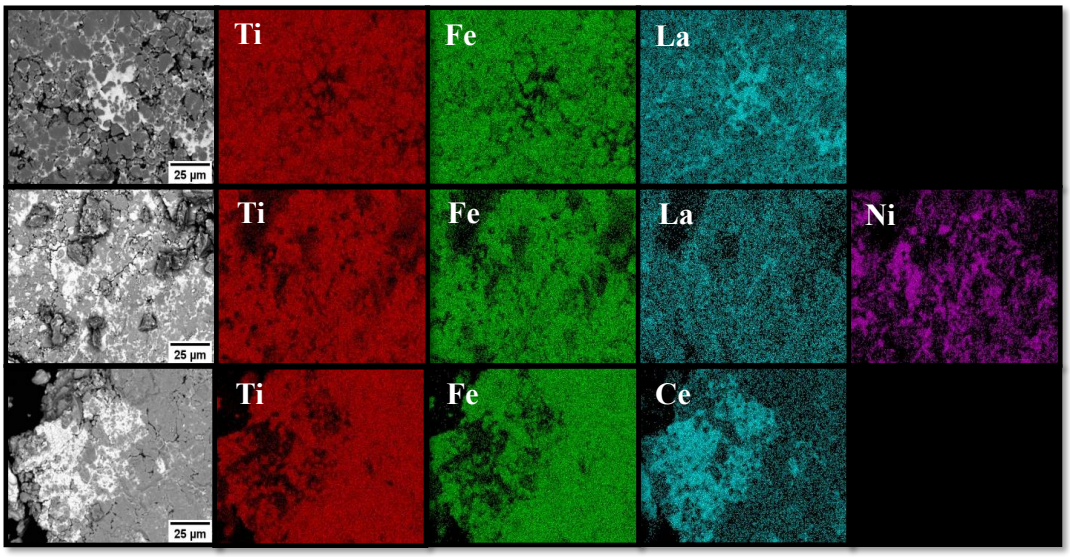

Figure 6.2: BSE images of MA TiFe alloy with additives in an as-synthesized state with EDX color mapping.

almost stoichiometric for the bulk composition. Except for the MM (Ce-MA TiFe) sample, the abundance of the additive is slightly higher. Similar to the findings in the previous chapter, where cast TiFe with additives was examined, can be extended to the investigation of mechanically alloyed (MA) TiFe with additives. Since the relative abundance of La and Ni is within the $LaNi_5$ stoichiometry, any systematic error can be ruled out, indicating that no Ti-Fe-La-Ni phase is formed, and the observed material corresponds to TiFe.

Fig. 6.3 presents the microstructure of as-synthesized TiFe with additives. The backscattered electron images depict two distinctive regions: a main matrix region in grey and a distinct bright region. This observation, along with the analysis shown in Fig. 6.2 suggests that the additives are localized rather than distributed.

The area fraction for both the bright and grey regions was quantified using ImageJ software, utilizing global thresholding via isoData. To ensure the reliability of the overall measurement, a random image with an appropriate field of view was chosen. The resulting area fraction values obtained from the analysis are reported in Table 6.2. The area fraction obtained from ImageJ deviates slightly from the nominal value, although the difference is insignificant.

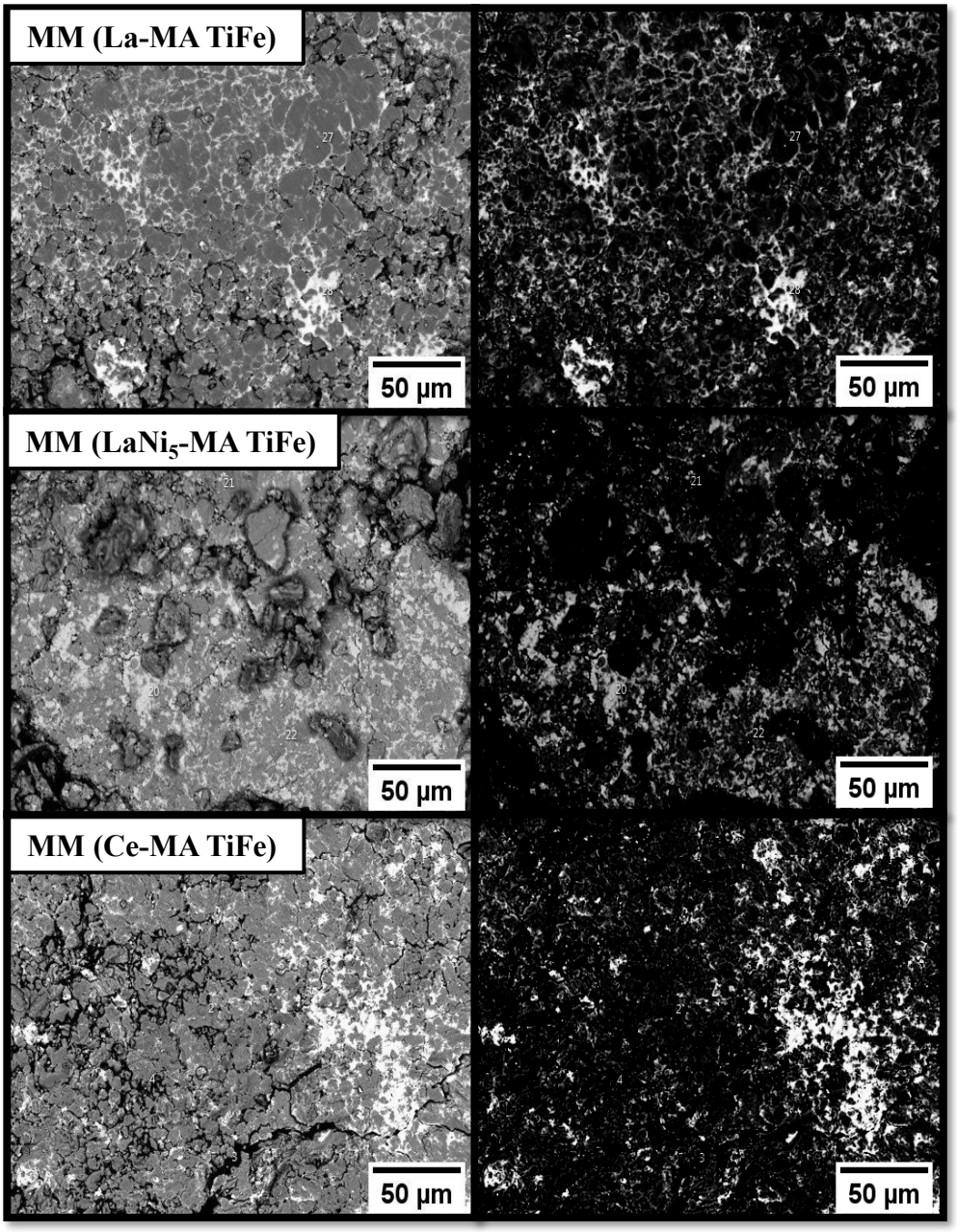

Figure 6.3: Backscattered electron images of MA TiFe alloy with additives. On the right side is the bright region marked using ImageJ software.

Table 6.2: Area fraction of TiFe as measured from ImageJ software. The uncertainty on the values is ± 1%.

Samples	**Nominal wt% of TiFe**	**Nominal area % of TiFe**	**Area % of TiFe calculated from ImageJ**
MM (Ce-MA TiFe)	84	85	87
MM ($LaNi_5$-MA TiFe)	84	87	86
MM (La-MA TiFe)	84	83	81

6.2 Crystal structure

The X-ray diffraction (XRD) patterns of the samples in the as-synthesized state are shown in Fig. 6.4. Rietveld refinement of these XRD patterns was also carried out and is presented in Table 6.3. All the samples are comprised of main TiFe phase characterized by CsCl-type structure with Pm-3m space group. Compared to the as-cast TiFe peaks, the peaks of milled TiFe with and without additive are broader. Whereas the peaks observed for the main matrix TiFe in the composites MM (Ce-MA TiFe), MM (La-MA TiFe), and MM ($LaNi_5$-MA TiFe) are broadened. The observed diffraction pattern aligns with the findings of Zaluski et al., where the oxygen content exceeded 3.0 at% [85, 93]. Our experimental approach of obtaining the MA TiFe and opening vials intermittently for the inclusion of additives to the MA TiFe is similar to the process (a) highlighted while discussing the study by Zaluski et al. in the literature section. The broadening of peaks indicates a decrease in crystallite size and/or the occurrence of microstrain. It can also be observed that the most intense Bragg peak of the TiFe phase in these composites got significantly less intense, while the higher angle peaks were almost flat and got buried in the background.

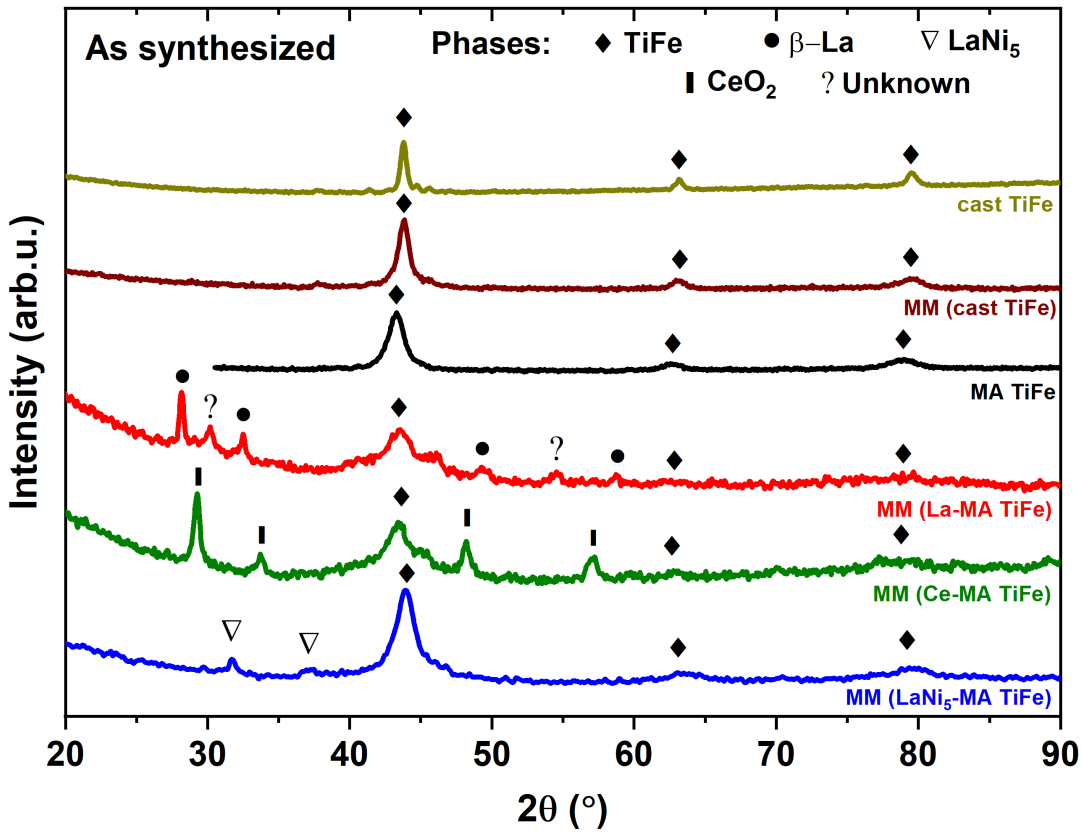

Figure 6.4: XRD of pure TiFe and MA TiFe with additives in an as-synthesized state.

Table 6.3: Crystal structure parameters of pure TiFe and MA TiFe with additives in an as-synthesized state. Numbers in parentheses represent errors on the last significant digit.

Samples	Phases	Phase Abundance (%)	Lattice parameters (Å)	Cell Volume (Å^3)	Crystallite size (nm)	Microstrain (%)
Cast TiFe	TiFe	100	2.9781(6)	26.41(1)	16.7(7)	0.32(5)
MM-cast TiFe	TiFe	100	2.9809(1)	26.49(3)	6.15(1)	0.10(3)
MA TiFe	TiFe	100	2.9839(1)	26.57(4)	5.39(1)	1.32(7)
MM (Ce-MA TiFe)	TiFe	93(2)	2.995(3)	26.87(8)	1.47(1)	-
	CeO_5	07(2)	5.424(5)	159.6(4)	13.9(1)	-
MM (La-MA TiFe)	TiFe	91.9(9)	2.997(3)	26.93(8)	1.9(2)	-
	β-La	8.1(9)	5.661(4)	181.4(4)	19(2)	-
MM ($LaNi_5$-MA TiFe)	TiFe	86.6(2)	2.989(6)	26.72(8)	2.95(1)	-
	$LaNi_5$	13.4(2)	a = 4.989(6), c = 3.983(6)	85.8(2)	11(2)	-

In the MM (La-MA TiFe) sample, the presence of β-La is noted, while CeO_2 is observed instead of elemental Ce in the MM (Ce-MA TiFe) sample. The MA TiFe with additives shows a similar phase presence to the observations made in the previous chapter when additives were introduced to cast TiFe. The diffraction pattern of the MM TiFe- $LaNi_5$ sample exhibits peaks corresponding to $LaNi_5$. Except for the $LaNi_5$ added TiFe sample, the calculated phase abundance of the secondary phase is lower than the nominal value (refer Table 6.3). The observed discrepancy can be attributed to the broadening of Bragg peaks and the strong background caused by fluorescence when Cu Kα radiation interacts with Fe, making the phase quantification difficult. Deconvoluting the phase abundance precisely is difficult also due to the small proportion of the additives. It has already been reiterated in the SEM-EDX measurement that the measured value of additives is slightly higher than the nominal value.

The ball-milled TiFe exhibits a slightly increased lattice parameter compared to its as-cast counterpart. This is within the literature provided range from 2.953 Å to 2.983 Å [69, 75]. Ball milling has the effect of reducing crystallite size. However, an interesting point is the reduction in the crystallite size of the TiFe phase observed in the cases of TiFe with additives. Such a small crystallite size is a characteristic of an amorphous-like phase, consistent with the study reported by Zaluski *et al.* [85, 93]. For the TiFe with additives patterns, the microstrain parameter was refined but the results were zero within the experimental errors. Therefore, the microstrain was not included in the final analysis.

6.3 Hydrogen sorption kinetics

Fig. 6.5 depicts the first hydrogenation of as-synthesized MA TiFe with additives along with pure TiFe. It should be noted that no repeated heat treatment or high pressure was applied. As noted earlier, the MA TiFe shows very sluggish kinetics, reaching just 0.23 wt% in 24 h, still not saturated and absorbs beyond that. The same MA TiFe readily activated when additives La, Ce, or $LaNi_5$ were incorporated into it. The activation of La-MA TiFe is relatively fast and reaches 1.28 wt% in just 3 h. The activation of the Ce-MA TiFe sample is equally fast, but the maximum hydrogen capacity reached is 1.01 wt%. It can be observed that the addition of $LaNi_5$ to TiFe shows a different behavior than that of La and Ce addition. The activation kinetics of $LaNi_5$-MA TiFe is slower than La and Ce-added MA TiFe samples, reaching a capacity of 1.0 wt% when exposed to hydrogen for a longer duration of 24 h (see inset). Pure TiFe synthesized by casting did not activate under the present experimental conditions. Interestingly, the same cast TiFe, when mechanically milled (MM-cast TiFe sample), gets activated with initial kinetics as fast as the La-MA TiFe with a maximum absorption capacity of 1.03 wt%.

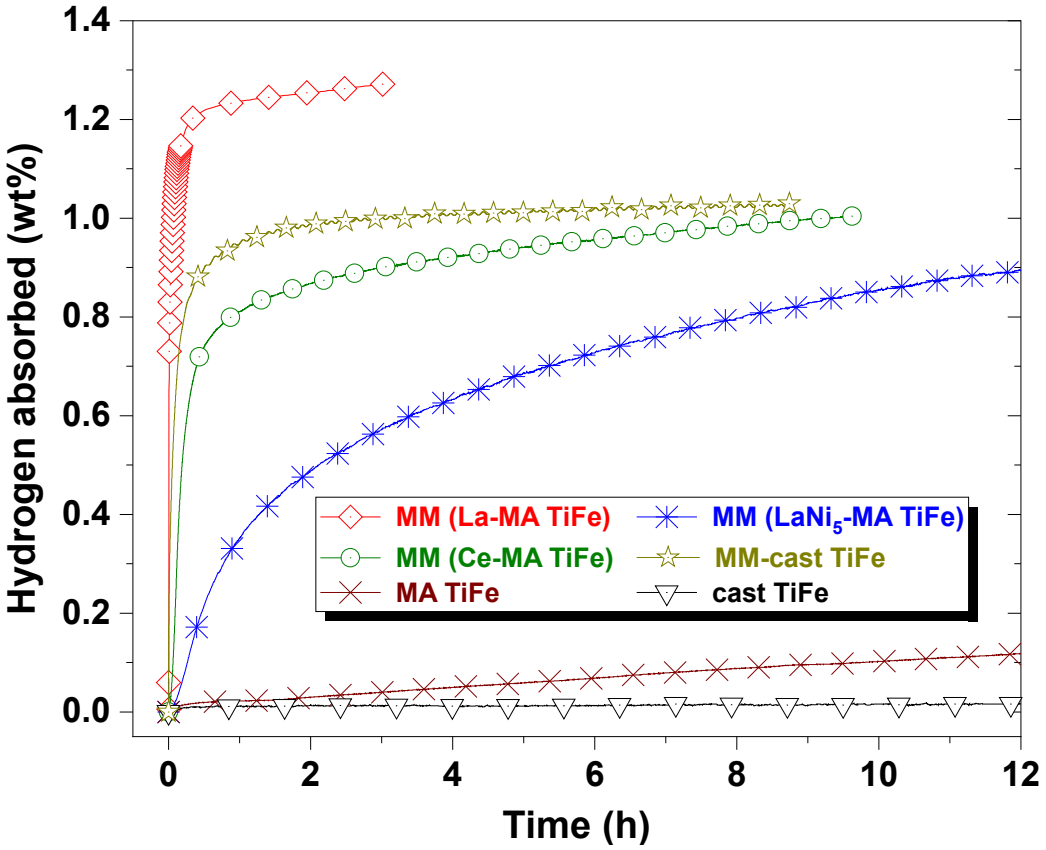

Figure 6.5: Activation of pure TiFe and MA TiFe with additives at room temperature (RT)

Fig. 6.6 depicts the desorption kinetics at room temperature with an initial hydrogen pressure of 5 kPa. Incomplete desorption was observed for all the samples. For example, MM-cast TiFe showed a maximum capacity of 1.0 wt% and desorbed 0.8 wt%. Since mechanical milling introduces new oxide-free surfaces and dislocations, micro-strain, and lattice distortions, these material defects can trap hydrogen atoms and do not allow dissociation at room temperature. In order to assess this behavior, structural characterization of the samples after de-hydrogenation was also carried out.

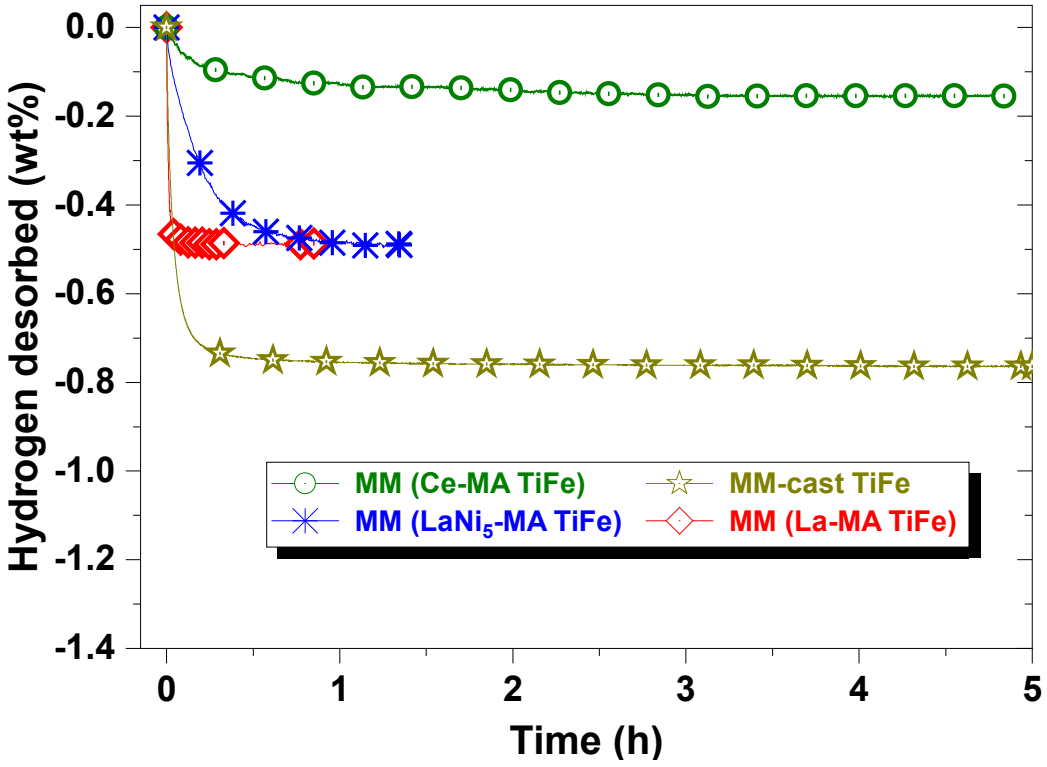

Figure 6.6: Desorption kinetics of MM-cast TiFe, MM (La-MA TiFe), MM (Ce-MA TiFe), and MM ($LaNi_5$-MA TiFe) alloys at room temperature (RT)

6.4 Crystal structure after de-hydrogenation

Fig. 6.7 depicts X-ray diffraction patterns of de-hydrided samples. The peaks of TiFe alloy are present in all the samples as TiFe hydride tends to desorb at room temperature. The Bragg peaks observed before hydrogenation and after de-hydrogenation are similar except for the La-MA TiFe sample, where the peaks are sharp. Moreover, the La-MA TiFe alloy shows peaks of LaH_3 (space group Fm-3m). It is reasonable to expect this to happen since Zhao *et al.* indicated that LaH_3 does not desorb even at 250 °C [131]. The stable nature of LaH_3 prevented its

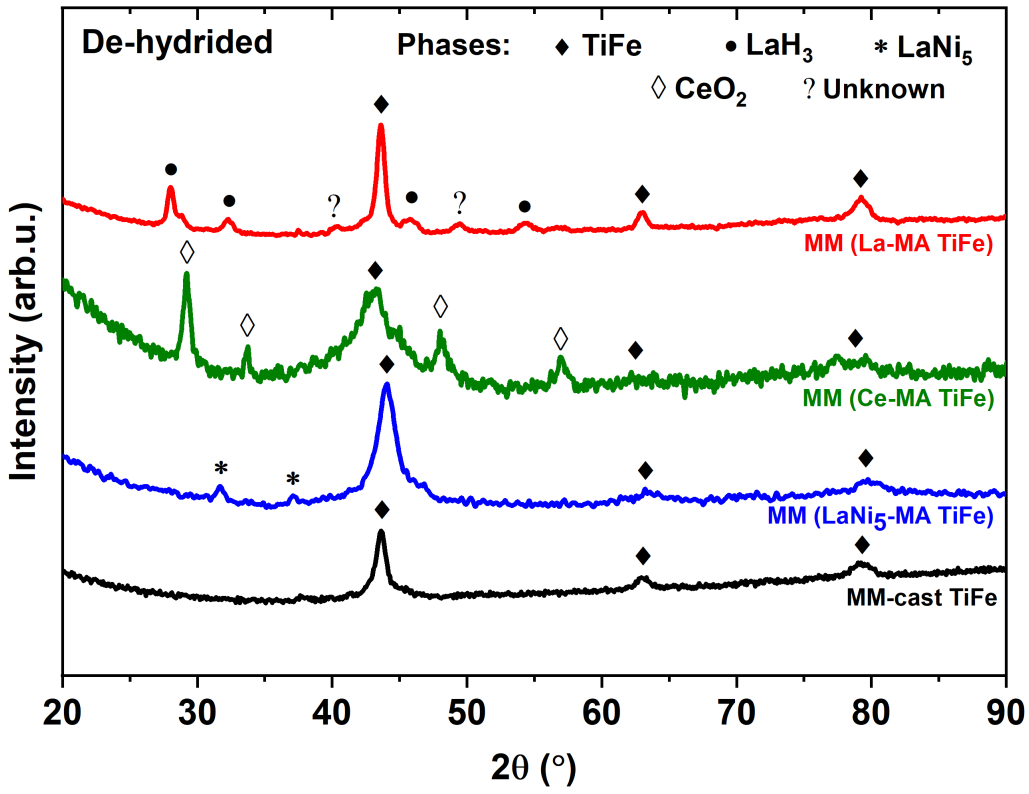

Figure 6.7: XRD of de-hydrided of MM-cast TiFe, MM (La-MA TiFe), MM (Ce-MA TiFe), and MM ($LaNi_5$-MA TiFe) alloys at room temperature (RT).

desorption under present experimental conditions. As anticipated for the $LaNi_5$-MA TiFe, peaks indicative of $LaNi_5$ are observed, not of any hydrides, as $LaNi_5$ tends to desorb at room temperature. After de-hydrogenation, the Ce-MA TiFe sample did not show any Ce-hydride or elemental Ce, but rather CeO_2, the same phase present in the as-synthesized state.

The crystal structure parameters of the de-hydrided samples were evaluated via Rietveld refinement of the diffraction patterns. They are presented in Table 6.4. Deconvoluting the phase abundance in the de-hydrided state poses similar challenges as those mentioned for the as-synthesized alloys. The abundance of the additives in the de-hydrided state is lower than the nominal value, and the trend is like the as-synthesized case. In fact, the crystal structure parameters are similar to the ones obtained for the as-synthesized alloys except for the crystallite size of the phases of La-MA TiFe alloy. After hydrogenation, the crystallite size of TiFe and LaH_3 changed significantly. The findings of the crystal structure parameters of the present situation where additives were introduced to MA TiFe are similar to when additives were incorporated into the cast TiFe, except for the crystallite size of the main matrix TiFe in Ce and $LaNi_5$-added MA TiFe samples, which are drastically smaller.

Table 6.4: Crystal structure parameters of the de-hydride samples. Numbers in parentheses represent errors on the last significant digit.

De-hydrided	Phase	Phase abundance (wt%)	Lattice parameters (Å)	Cell volume (Å^3)	Crystallite size (nm)	Microstrain (%)
MM-cast TiFe	TiFe	100	2.9861(2)	26.63(4)	5.8(2)	0.10(5)
La-MA TiFe	TiFe	89.6(9)	2.988(1)	26.83(3)	8.4(4)	-
	LaH_3	10.4(9)	5.674(3)	182.7(3)	10.0(6)	-
Ce-MA TiFe	TiFe	79(3)	3.042(1)	28.15(4)	1.03(5)	-
	CeO_2	21(3)	5.446(1)	161.56(1)	7.7(2)	-
$LaNi_5$-MA TiFe	TiFe	90.5(2)	2.982(4)	26.51(1)	3.02(1)	-
	$LaNi_5$	9.5(2)	a = 4.990(7)	85.8(3)	14(4)	-
			c = 3.981(4)			

Peng *et al.* established a correlation between the decrease in crystallite size resulting from ball milling and a corresponding reduction in capacity [88]. Moreover, they discuss the increase of grain boundaries that serve as additional pathways for hydrogen diffusion but do not serve as hydrogen storage sites. Nevertheless, the drastic reduction in the desorption capacity remains unclear, but could be due to the samples being handled and analyzed under atmospheric conditions while performing XRD. Further investigation as a future work following in-situ measurements could give a clue. It should be pointed out that the microstructure played a significant role in activating TiFe with additives, while crystal structure was pivotal in determining the hydrogen sorption capacity.

The marked enhancement in the activation of La-MA TiFe is primarily a result of nano-crystallinity, milling-induced defects, and the formation of a highly stable LaH_3 phase. The formation of LaH_3 facilitated by heterogeneous nucleation provided an excellent diffusion channel for hydrogenation. Similar observations were made by Shang *et al.* when they introduced Pr and Sm to the TiFe-based alloy, forming PrH_2 and Sm_3H_7 phases, respectively [107, 108]. The diffusion factor of LaH_3 is relatively small. However, the composition LaH_2 has a much better diffusion factor [133]. It is known that, upon dehydrogenation of another metal hydride, a certain hydride phase could change its stoichiometry to accommodate a faster diffusion. This inference is drawn based on the observation reported for the composites MgH_2+Nb and MgH_2+NbH [134, 135, 136]. The same can be said for the $LaNi_5$-MA TiFe sample, except that the $LaNi_5$-hydride is not stable and desorbs at room temperature. As stated earlier, for the Ce-MA TiFe sample, the CeO_2 phase was present in the as-synthesized and de-hydride state. The mechanism of how stable CeO_2 helped in activation is not clear at this point, but it was probably due to the role played by the phase boundaries between TiFe and CeO_2. An interesting further study would be to know how CeO_2 helped activate the Ce-MA TiFe sample. Besides, an in-situ investigation coupled with analyti-

cal characterization could provide some clues for the activation mechanism in the Ce-MA TiFe sample.

The findings of the present and previous chapters are compiled in Table 6.5 to compare among them and the literature presented in section 2.4. The activation kinetics of Ce and $LaNi_5$-added MA TiFe samples are slower compared to the study when the same additives were inducted to cast TiFe. This can be because the crystallite size of the main matrix TiFe in the Ce and $LaNi_5$-added samples is extremely low, and the samples show an amorphous-like nature. Moreover, the activation kinetics of La-MA TiFe is faster in the present investigation compared to when the additives were inducted to cast TiFe, the reason being that the La-MA TiFe is highly crystalline. Notably, the activation of La-MA TiFe is faster than the system when Zr, Y, and Mn are incorporated into TiFe [62, 69, 123] and are comparable to the Ce and Hf added TiFe synthesized by arc melting [55, 67]. The activation of Ce-MA TiFe and $LaNi_5$-MA TiFe samples share similarities with the findings of Y-added TiFe alloy synthesized by arc melting [69] and Mn-added TiFe alloy synthesized by induction melting followed by 30 min MM [123].

Table 6.5: Findings of this chapter compiled to compare with the literature-reported results and the results of previous chapter.

Synthesis process	**Samples**	**Absorption (wt%) @ RT & 20 bar**	**References**
TiFe by MA	MM (Ce-MA TiFe)	1.0 (10 h)	**This chapter**
thereafter 15 min	MM (La-MA TiFe)	1.3 (3 h)	**This chapter**
MM with additives	MM ($LaNi_5$-MA TiFe)	1.0 (24 h)	**This chapter**
15 min MM of cast TiFe	MM-cast TiFe	1.0 (3 h)	**Previous chapter**
TiFe by cast	MM (Ce-cast TiFe)	1.2 (1 h)	**Previous chapter**
thereafter 15 min	MM (La-cast TiFe)	1.0 (20 h)	**Previous chapter**
MM with additives	MM ($LaNi_5$-cast TiFe)	0.9 (6 h)	**Previous chapter**

6.5 Summary

The MA TiFe alloy was investigated for its hydrogen storage properties by adding an intermetallic $LaNi_5$ and rare earth elements La and Ce. The addition was conducted by short-term ball milling in order to maintain the composite nature of the materials. Based on the results obtained, the following conclusions can be drawn:

- Crystalline TiFe was synthesized by mechanical alloying (MA). The incorporation of additives to MA TiFe by mechanical milling (MM) leads to the transformation of crystalline TiFe to an amorphous-like nature due to the oxidation resulting from materials and the milling environment. This is consistent with the study reported by Zaluski *et al.* [85, 93].

- Morphological investigation revealed the presence of two distinct regions in the MA TiFe with additives, viz., the main matrix TiFe region and a secondary region containing the additives. A similar morphology was observed in the investigation presented in previous chapter wherein the additives were inducted to cast TiFe by MM.

- The activation was quick and more complete, reaching 1.3 wt% in 3 h when the additive was La and the formation of a stable LaH_3 phase was observed. The hydrogenation was quick, but the maximum capacity reached was 1.0 wt% when the additive was Ce. Interestingly, a similar activation behavior was observed when the cast TiFe was mechanically milled (MM-cast TiFe). The activation of $LaNi_5$ added sample was slow, reaching 1.0 wt% in 24 h. Incomplete desorption was observed for all the samples at room temperature under 5 kPa.

- Crystal-structural parameters before and after de-hydrogenation remained largely unchanged except for the sample MM (La-MA TiFe), wherein the crystallite size increased after de-hydrogenation. The crystallite size of the main matrix TiFe in the sample MM (Ce-MA TiFe) was unreasonably low; a similar trend of unreasonably low crystallite size was observed for the sample MM ($LaNi_5$-MA TiFe).

CHAPTER 7

Hydrogenation of TiFe-La & TiFe-Ce synthesized by MA only

In this chapter, we report the effect of adding rare earth element lanthanum and cerium on the hydrogen storage properties of TiFe synthesized by mechanical alloying (MA) only. Elemental powder mixtures consisting of stoichiometric TiFe were added with La in one case and Ce in another. The synthesis process is described in detail in section 3.2.4. For simplicity, the synthesized alloys are designated as MA TiFe-La and MA TiFe-Ce.

7.1 Microstructure

Fig. 7.1 shows the morphology of as-synthesized samples. The as-cast TiFe particles are characterized by sharp edges resulting from crushing in a mortar and pestle. The MM-cast TiFe particles are round, a consequence of milling. The MA TiFe has a sponge-like structure of agglomerated particles. The MA TiFe-La and MA TiFe-Ce have similar morphology with an average particle size bigger than that of MA TiFe, although all three of them were milled for the same duration.

Back-scattered electron (BSE) micrographs of the MA TiFe-La and MA TiFe-Ce samples are presented in Fig. 7.2 along with the corresponding energy dispersive x-ray spectroscopy (EDX) color mapping. The alloys appear like a single phase from BSE images because there is only one grey scale contrast. Also, there is no variation in the color mapping, indicating a uniform distribution of the elements.

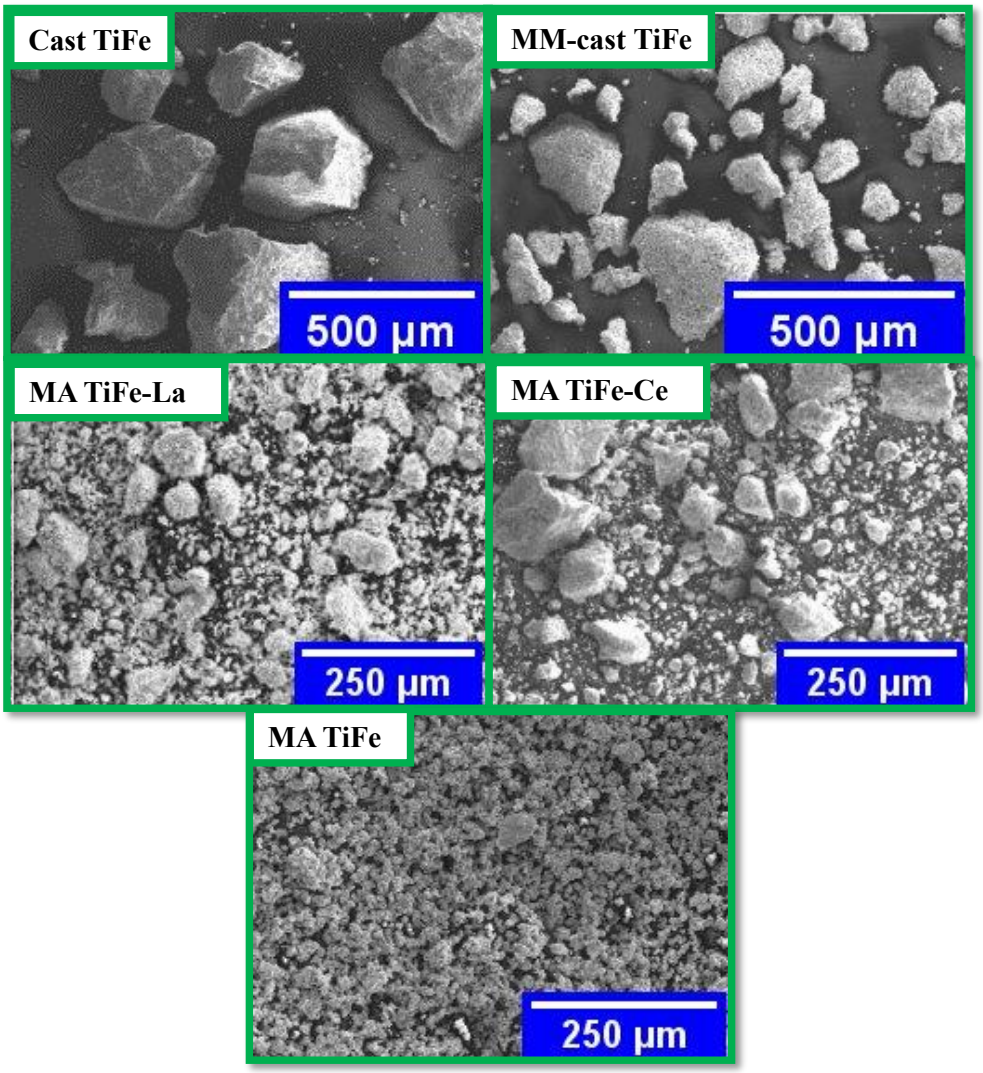

Figure 7.1: Scanning electron microscopy of cast TiFe, MM-cast TiFe, MA TiFe, MA TiFe-La, and MA TiFe-Ce samples in as-synthesized state.

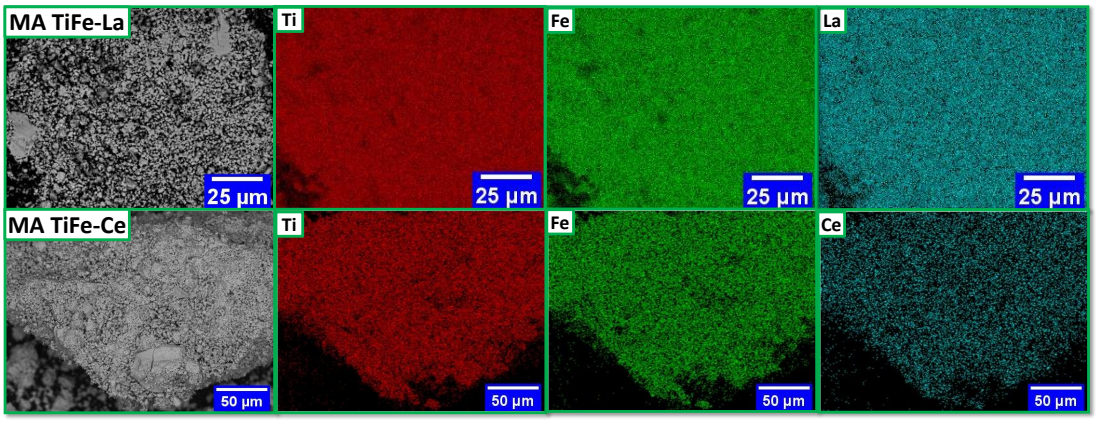

Figure 7.2: BSE images of as-synthesized MA TiFe-La and MA TiFe-Ce with the corresponding EDX color mapping.

Fig. 7.3 shows the back-scattered electron image of the MA TiFe-La sample at a higher magnification. The alloy appears single-phase since there is only one greyscale contrast in the backscattered images. Moreover, insignificant compositional variation was observed on EDX mapping at three randomly selected locations, reiterating that the constituent elements are uniformly distributed. We just indicated one set of image and magnification in order to make the reading easier. The different measurements on each phase agree within the error bar.

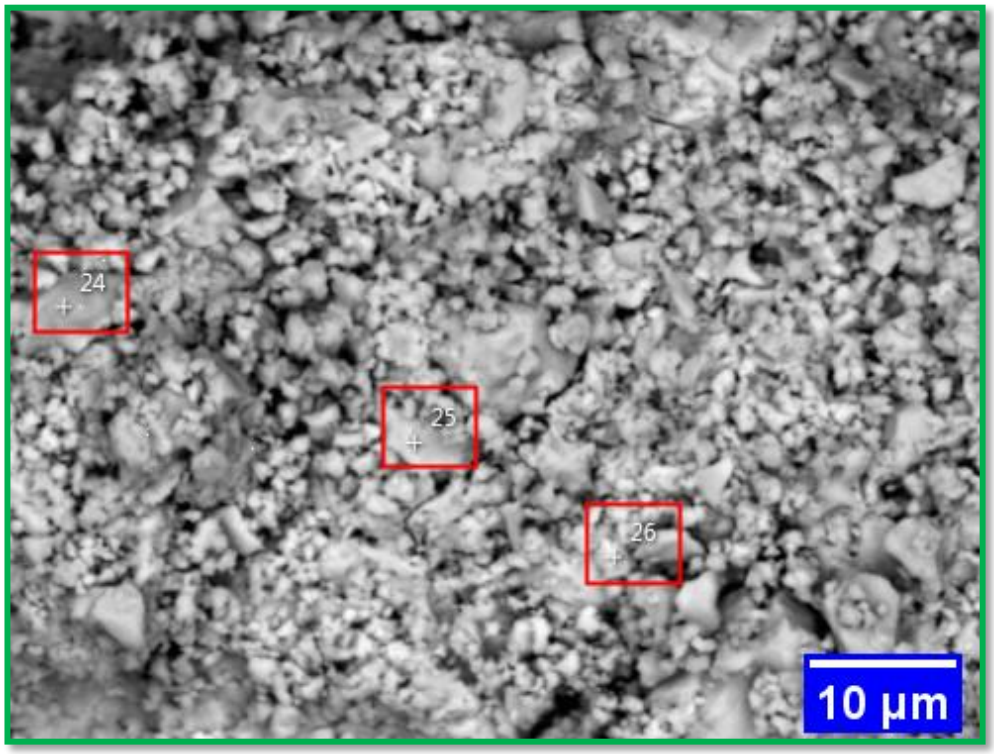

Figure 7.3: Back-scattered electron image of as-synthesized MA TiFe-La alloy.

Table 7.1 shows the elemental analysis results of all the samples by EDX. The concentration of Fe and Ti is almost equiatomic in all the alloys, and they are very close to the nominal value. The measured concentration of La and Ce is slightly lower than the nominal concentration of 6.6 at%.

Table 7.1: Elemental compositions of as-synthesized alloys measured analytically via EDX. Uncertainty on all the values is ±1 at%.

Sample	Ti (at%)	Fe (at%)	La (at%)	Ce (at%)
Cast TiFe	51.6	48.4	-	-
MM-cast TiFe	52.6	47.4	-	-
MA TiFe	49.0	51.0	-	-
MA TiFe-La	46.1	48.4	5.5	-
MA TiFe-Ce	45.9	48.3	-	5.8

7.2 Crystal structure before hydrogenation

Fig. 7.4 shows the X-ray diffraction patterns of as-synthesized cast TiFe, MM-cast TiFe, MA TiFe, MA TiFe-La and MA TiFe-Ce alloys. It can be observed that the pattern of as-cast TiFe has sharp peaks, whereas the patterns of all the other alloys that were ball milled have broad peaks. All the samples show the peaks of the main TiFe phase with a CsCl-type structure (space group Pm-3m). The as-synthesized MA TiFe-Ce sample exhibits peaks of the main matrix TiFe phase along with broad peaks of CeO_2 (cerianite, space group Fm-3m). The as-synthesized MA TiFe-La sample reveals peaks of the main matrix TiFe phase and broad peaks of the room temperature La phase (space group $P6_3/mmc$).

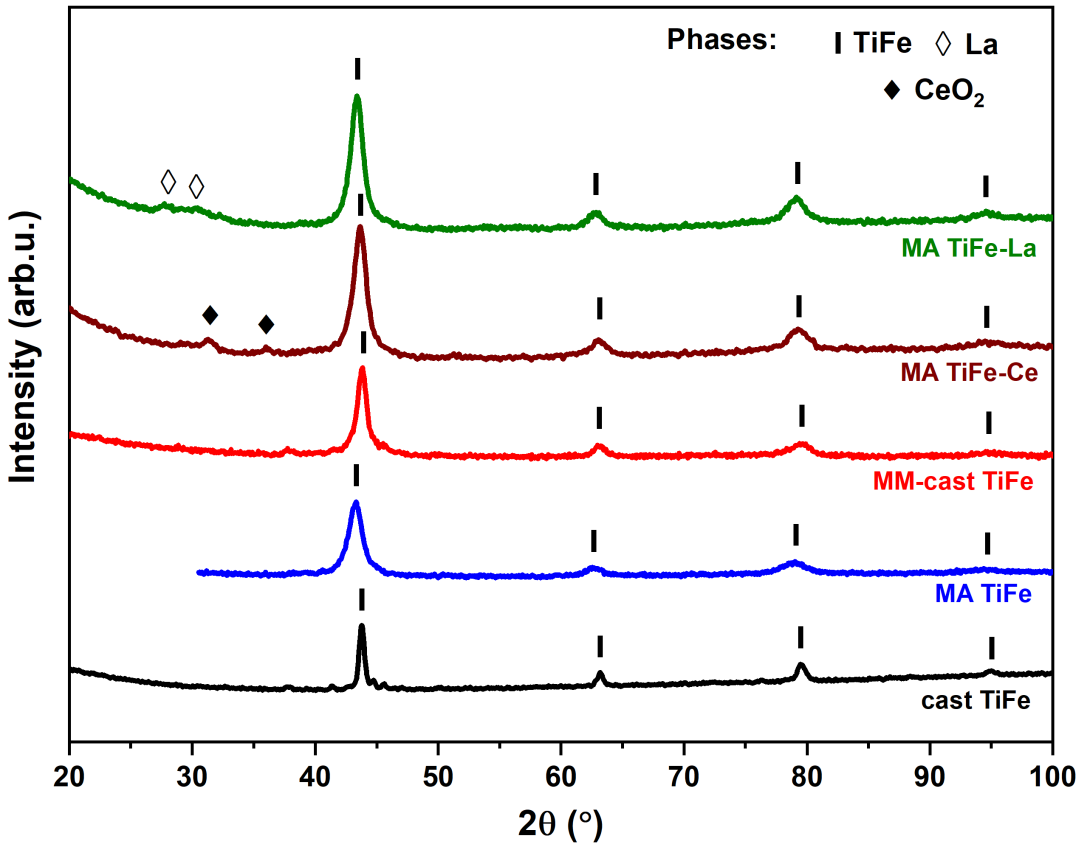

Figure 7.4: X-ray diffraction patterns of as-synthesized samples.

Rietveld refinement was performed on all the X-ray diffraction patterns to evaluate the crystal structure parameters. They are presented in Table 7.2. The abundance of La and CeO_2 is 6.8 and 0.5 %, respectively, which is too low compared to the nominal value of 16 wt%. The discrepancy in calculating the abundance of La & CeO_2 by Rietveld refinement is because of the broad peaks. And also, due to the fluorescence of iron with Cu radiation producing strong background, it could not be adequately deconvoluted. The amount of La and CeO_2 in the MA TiFe-La

and MA TiFe-Ce alloys have already been confirmed from the EDX analysis that the composition is close to the nominal value of 6.6 at% (refer to Table 7.1).

Table 7.2: Crystal structure parameters of the as-synthesized samples. Numbers in parentheses represent errors on the last significant digit.

Samples	Phases	Phase abundance (%)	Lattice parameters (Å)	Cell volume (Å^3)	Crystallite size (nm)	Microstrain (%)
Cast TiFe	TiFe	100	2.9781(6)	26.41(1)	16.7(7)	0.32(5)
MM-cast TiFe	TiFe	100	2.9809(1)	26.49(3)	6.15(1)	0.10(3)
MA TiFe	TiFe	100	2.9839(1)	26.57(4)	5.39(1)	1.32(7)
MA TiFe-Ce	TiFe	99.5(1)	2.9813(1)	26.50(4)	4.97(2)	-
	Ce	0.5(1)	5.446(1)	161.52(1)	2(3)	-
MA TiFe-La	TiFe	93.2(1)	2.9804(1)	26.47(3)	5.23(1)	0.61(1)
	La	6.8(1)	a = 3.769(1), c = 12.080(1)	148.61(1)	1.29(2)	-

The lattice parameter of TiFe is slightly higher in the ball-milled samples compared to the as-cast alloy. However, the literature values range from 2.953 Å to 2.983 Å [69, 75]. Therefore, this discrepancy may not be significant. The crystallite size of the TiFe phase is reduced by milling, but it should be noticed that the MM and MA processes produced almost the same crystallite size. It can also be seen that the crystallite size of the La and CeO_2 phases are 1.29 nm and 2 nm, respectively. Such small crystallite size produces very broad peaks that are difficult to distinguish from the background. It is probably the reason why the abundance of the elements does not agree with the abundance measured by EDX. The microstrain is more prominent for the alloys synthesized by mechanical alloying.

7.3 Hydrogen sorption kinetics

Fig. 7.5 shows the first hydrogenation of the samples at room temperature under an initial pressure of 20 bars. For the MA TiFe-La sample, activation was also carried out at 40 bars of initial hydrogen pressure. Pure TiFe alloy synthesized by mechanical alloying of elemental powders shows extremely slow kinetics and reaches just 0.1 wt% in more than 8 hours. Pure TiFe alloy synthesized by casting did not activate under the present experimental conditions. It confirms the reported studies that the activation of TiFe without additive or mechanical deformations does not occur at room temperature [51, 52, 62, 67].

Significant improvement in activation kinetics was observed with the addition of La. The MA TiFe-La sample reached a maximum hydrogen storage capacity of 1.3 wt% within 30 minutes. It can also be observed that only a slight change in initial kinetics and maximum capacity was observed at 40 bar initial hydrogen

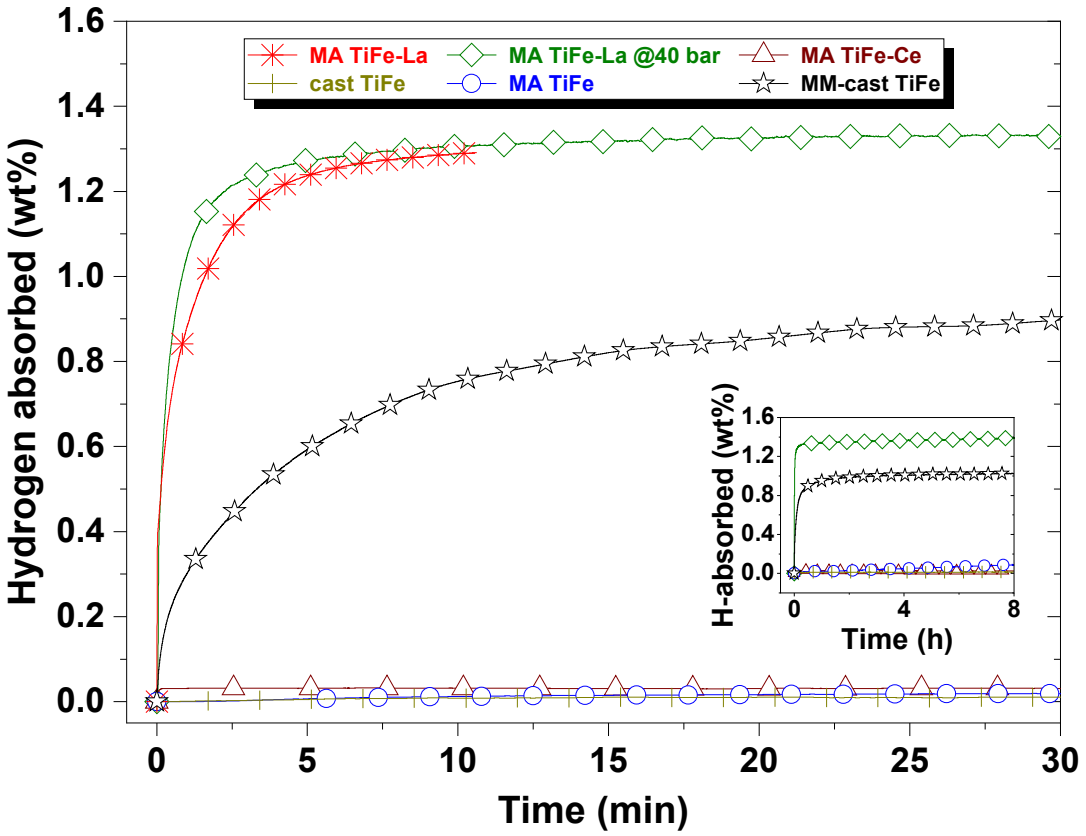

Figure 7.5: First hydrogenation (activation) kinetics at room temperature (RT) under 20 bar of hydrogen pressure of MA TiFe, cast TiFe, MM-cast TiFe, MA TiFe-Ce, and MA TiFe-La alloys. Activation under 40 bar of hydrogen for MA TiFe-La is also shown.

pressure compared to 20 bars. The improvement in activation kinetics by adding La is faster than the one with Zr_7Ni_{10} as an additive [52] and comparable with the one using Hf as an additive [67]. Interestingly, cast TiFe, when ball milled for a short duration of 15 minutes (denoted as MM-cast TiFe), also activated and reached a capacity of 1.0 wt%. The activation of MA TiFe alloy is 5 orders of magnitude slower than MA TiFe-La synthesized by following the same MA process. The MA TiFe-Ce sample is totally impermeable to hydrogen and did not show any activation. This may be due to the prolonged milling of cerium oxide observed in the diffraction pattern.

7.4 Crystal structure of de-hydrided state

Fig. 7.6 shows the X-ray diffraction patterns of the de-hydrided MM-cast TiFe and MA TiFe-La samples. The de-hydrided MA TiFe-La alloy has peaks of LaH_3 (space group Fm-3m) in addition to the main TiFe phase. This is expected as

Zhao *et al.* indicated that LaH_3 does not desorb even at 250 °C [131]. Thus, LaH_3 being stable, did not desorb under the present experimental conditions of room temperature at 5 kPa hydrogen pressure. No noticeable change in the peaks was observed between the as-synthesized and de-hydrided MM-cast TiFe samples.

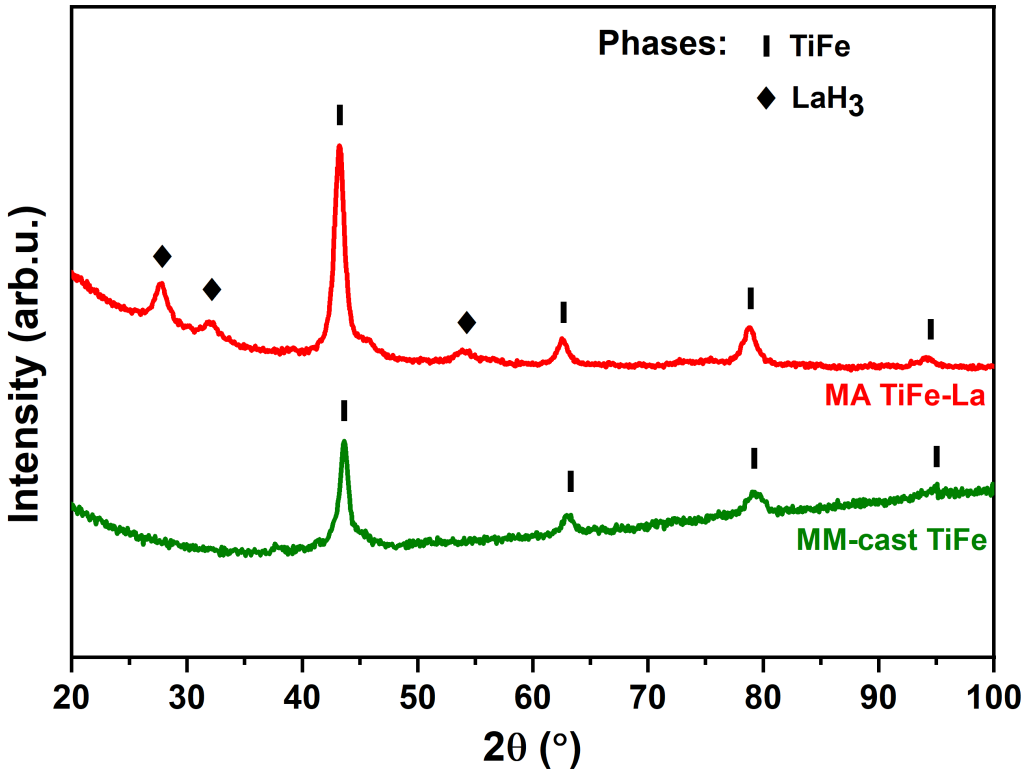

Figure 7.6: XRD patterns of the de-hydrided MM-cast TiFe and MA TiFe-La samples.

The crystal structure parameters of the de-hydrided samples were calculated by the Rietveld refinement of the diffraction patterns and are presented in Table 7.3. The phase abundance of the de-hydrided MA TiFe-La sample for the phases TiFe and LaH_3 are 86.8 wt% and 13.2 wt%, respectively, which is close to the nominal values.

The lattice parameter and hence the cell volume of the TiFe phase is slightly bigger than that of the as-cast case. This may be due to the small amount of hydrogen still in the solid solution in the TiFe phase. Assuming a hydrogen volume between 2 and 3 $Å^3$, the hydrogen in solid solution is estimated to be between 0.04 and 0.06 wt%.

The crystallite size of the TiFe phase in the as-cast and de-hydrided state is similar. However, the LaH_3 phase has a crystallite size almost three times bigger than that of the La phase in the as-synthesized alloy. This bigger crystallite size makes the Bragg's peaks sharper and easier to distinguish from the background.

Table 7.3: The crystal structure parameters of the de-hydrided MM-cast TiFe and MA TiFe-La samples. Numbers in parentheses represent errors on the last significant digit.

Samples	Phases	Phase abundance (%)	Lattice parameters (Å)	Cell volume (Å^3)	Crystallite size (nm)	Microstrain (%)
MM-cast TiFe	TiFe	100	2.9861(2)	26.63(4)	5.8(2)	0.10(5)
MA TiFe-La	TiFe	86.8(8)	2.9901(6)	26.73(2)	6.76(9)	0.70(5)
	LaH_3	13.2(8)	5.662(2)	181.5(2)	3.82(9)	-

This is the reason why the phase abundance of LaH_3 agrees well with the nominal abundance. This also indicates that La did not alloy with TiFe. Similar to the crystallite sizes, the microstrain of the de-hydrided samples are identical to the ones measured in the as-synthesized alloys.

The remarkable improvement in the activation of MM-cast TiFe can be attributed to milling, while in the case of MA TiFe-La, the improved activation results from both milling and the presence of the highly stable LaH_3 phase. The nano-crystallinity, defects resulting from milling, and the formation of LaH_3 facilitated by heterogeneous nucleation provided an excellent diffusion channel for hydrogenation. Similar observations were made by Shang et al. when they introduced Pr and Sm to the TiFe-based alloy, forming PrH_2 and Sm_3H_7 phases, respectively [107, 108].

7.5 Thermodynamics

Pressure composition isotherms (PCT) were obtained for the sample MA TiFe-La, which showed fast hydrogenation kinetics. Fig. 7.7 shows the PCT obtained at 20 °C to 80 °C temperatures. The maximum capacity reached is only 0.80 wt%, lower than the maximum capacity achieved during the first hydrogenation kinetics. The mono-hydride and di-hydride plateau pressures at room temperature for cast TiFe alloy reported in the literature are ≈5 bars and ≈15 bars [1, 24]. In the present study, the mono-hydride plateau pressure of the sample is close to the reported value, but at the same time, the di-hydride plateau is not observed. It appears to be displaced to a higher pressure.

Hotta et al. studied the activation and PCT of MA TiFe that absorbed 1.3 wt% hydrogen. Prior heat treatment at 573 K was performed before an activation at room temperature and 150 bar hydrogen pressure. PCT measurement revealed the increase of the di-hydride plateau to a very high pressure of 250 bar H_2 [89]. Abe and Kuji reported another study on MA TiFe alloy with post-annealing over 773 K for hydrogen absorption [90]. The maximum capacity reached was 1.25

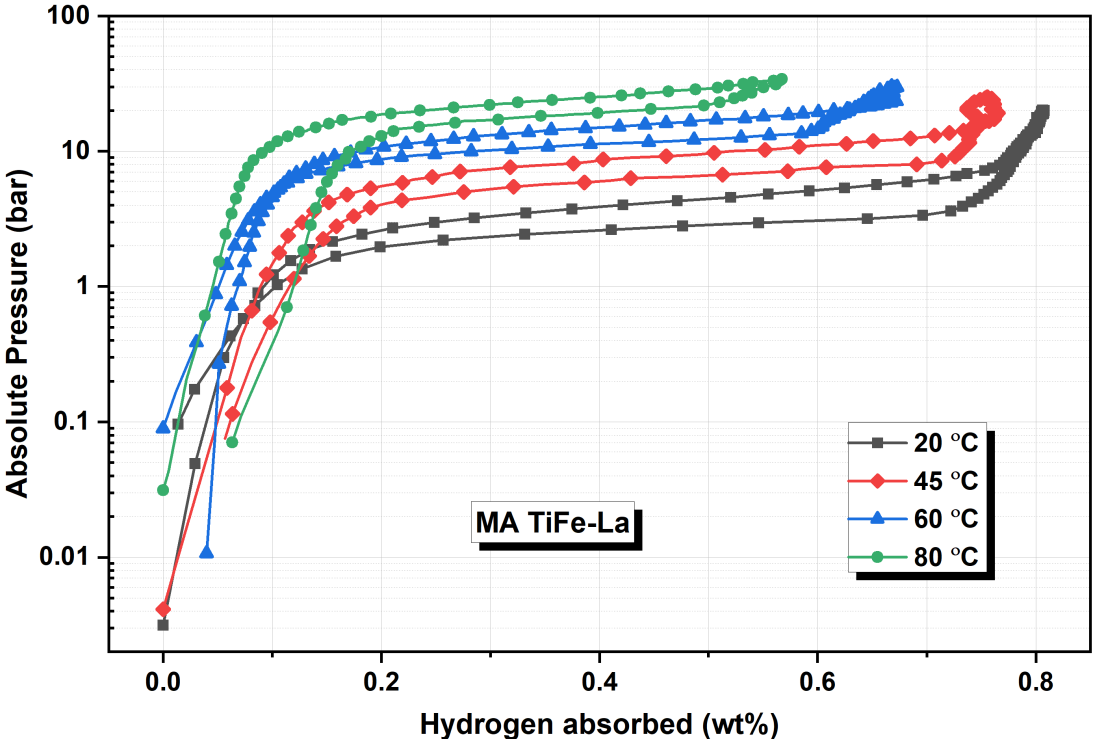

Figure 7.7: Pressure Composition Isotherms (PCTs) of mechanically alloyed TiFe-La sample.

wt% at 50 bar H_2, but the second plateau was absent at this pressure. Emami et al. milled a commercial TiFe alloy instead of synthesizing it from elemental powders [57]. The alloy absorbed 1.3 wt% hydrogen exhibiting the start of the second plateau around 100 bar H_2. Based on the above-cited literature, it could be concluded that the synthesis of TiFe through mechanical alloying has the effect of moving the second plateau to very high pressure (above 100 bar).

Since the second plateau is absent in the present experimental condition of up to 40 bar of H_2 pressure and observed only mono-hydride formation of TiFe alloy with hydrogen. The calculated theoretical absorption capacity of mono-hydride TiFe is 0.95 wt%. The MA TiFe-La alloy consists of 16 wt% of La, so the theoretical absorption capacity of TiFe would be 0.80 wt%, which was measured in PCT. It is worth noting that the isotherms have an extended and almost flat plateau for the MA TiFe-La alloy. Zaluski et al. and Abe and Kuji used high-temperature annealing in conjunction with heating to obtain a reasonably flat plateau for mechanically alloyed and mechanically milled samples [137, 90].

Fig. 7.8 shows Van't Hoff plot of the PCT curves at a capacity of 0.4 wt%, taken at mid-capacity because the plateau is almost flat. The relationship between equilibrium pressure and temperature is given by Van't Hoff equation (refer to Eq. 1.5 in chapter one).

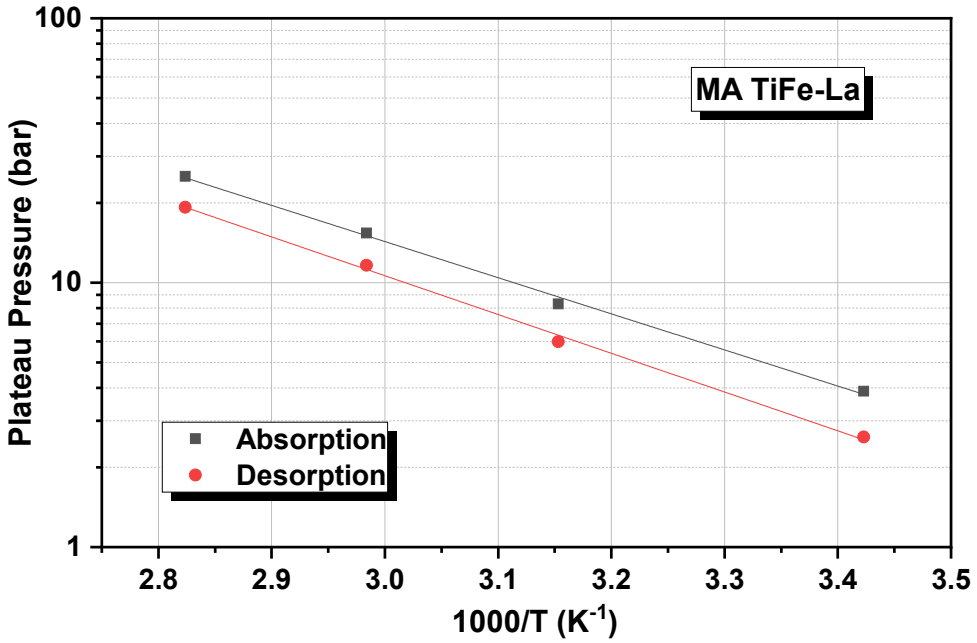

Figure 7.8: Van't Hoff plot of hydriding-dehydriding MA TiFe-La sample between 20 to 80 °C at 0.4 wt% hydrogen capacity.

The values ΔH and ΔS were obtained from the slope and intercept of the linear regression plots. The obtained values of the enthalpy and entropy of formation/dissociation of hydriding-dehydriding of MA TiFe-La are compared with the pure TiFe from the literature. They are presented in Table 7.4. It can be observed that the values for the MA TiFe-La sample studied are comparable to that of the pure TiFe alloy reported in the literature [24]. The thermodynamics of MA TiFe-La is almost the same as pure TiFe in the observed first plateau region. Thus, it can be inferred that even though EDX color mapping showed a uniform distribution of the elements, the additive La exhibited no solubility in the TiFe alloy. Adding La to TiFe by MA barely changes its thermodynamics, which is consistent with the study reported by Wang et al. on La-added TiFe synthesized by melting [54].

Table 7.4: Enthalpy and entropy of formation/dissociation for hydriding-dehydriding of MA TiFe-La alloy.

Alloy	$\Delta\mathbf{H_{abs}}$ **(kJ/molH$_2$)**	$\Delta\mathbf{S_{abs}}$ **(kJ/molH$_2$)**	$\Delta\mathbf{H_{des}}$ **(kJ/molH$_2$)**	$\Delta\mathbf{S_{des}}$ **(kJ/molH$_2$)**	**Hysteresis factor** $\ln(\mathbf{P_{abs}}/\mathbf{P_{des}})$
MA TiFe-La	-26.2 ± 0.1	-100 ± 3	28.1 ± 0.1	104 ± 3	0.40 ± 0.01
Pure TiFe [1, 24]	-	-	28.1	106	0.64

7.6 Summary

This investigation focused on the first hydrogenation of TiFe with La or Ce additive. The effect of ball milling on the cast alloy and the Ti-Fe mixture was also investigated. The key findings of this investigation can be summarized as follows:

- TiFe and TiFe with additives were successfully synthesized from elemental powder mixtures using mechanical alloying.
- The additives were uniformly distributed but immiscible with the TiFe alloy.
- The addition of La significantly improved the activation kinetics of the TiFe alloy.
- Milling of cast TiFe also resulted in activation, albeit slower than La-added TiFe.
- The remarkable enhancement in activation of milling cast TiFe can be attributed to the reduction of crystallite size and addition of defects.
- In mechanically alloyed TiFe-La, nano-crystallinity, and the highly stable LaH_3 phase contributed to the improved activation.
- Milling led to the refinement of the crystallite size of the TiFe alloy. The formation of LaH_3 facilitated through heterogeneous nucleation acted as a gateway for the hydrogenation of the TiFe phase.
- The thermodynamics of La-added TiFe were practically identical to pure TiFe.
- It was observed that the addition of Ce into TiFe did not improve activation kinetics compared to La-added TiFe. It could be due to the formation of an oxide.

CHAPTER 8

Summary and conclusion

Three systems based on the addition of La, Ce, and $LaNi_5$ to the TiFe alloy were synthesized primarily by exploring a new strategy of combining ball milling and arc melting. The hydrogenation, microstructure and crystal structure of the alloys were investigated. The overall findings of the study are summarized below:

- Crystalline TiFe was successfully synthesized by mechanical alloying (MA) and casting. TiFe-Ce and TiFe-La were also synthesized from elemental powder mixtures via MA.
- Mechanical milling (MM) of cast TiFe led to the refinement of crystallite size to nano-crytallinity and activation was successful without additives. However, MM of MA TiFe in conjunction with additives, transformed the crystalline TiFe to an amorphous like nature due to the oxidation resulting from materials and milling environment.
- In general, MM of TiFe alloy with additives facilitated the composite formation without resulting in the formation of new phases.
- Observed remarkable improvement in activation of TiFe alloy with additives as compared to pure TiFe alloy.
- Thermodynamics of MA TiFe-La barely changed and were practically identical to pure TiFe. It could be inferred that none of the additives (La, or Ce or $LaNi_5$) would change the thermodynamics of TiFe alloy due to non-inclusion into the main matrix.

8.1 Conclusion

Morphological investigations of the composites of TiFe with additives revealed the presence of two distinct regions, viz., the primary matrix TiFe region and a secondary region mainly containing the additives. The Ti and Fe composition in both the regions have the same atomic abundance, thus what was seen was the TiFe phase. For the $LaNi_5$ additive, the relative abundance of La and Ni was very close to stoichiometry in both the regions, therefore any systematic error was ruled out. This also means that the additives did not decompose, and no La-Ni-Ti-Fe phase has been formed. Therefore short milling duration facilitated the composite formation of TiFe with the additives without resulting in the formation of new phases. Whereas, the mechanical alloying of elemental powders Ti, Fe, and additives (La or Ce) evolved into a uniformly distributed composition, yet the additives remain immiscible to the TiFe matrix.

The cast TiFe synthesized by arc melting did not activate under the present experimental conditions. However, the same alloy, when mechanically milled (MM-cast TiFe), gets hydrogenated with an absorption capacity of 1.0 wt%. The first hydrogenation of the composites TiFe with additives (La, Ce, $LaNi_5$) were remarkably fast reaching between 1.0 to 1.35 wt% quickly except three composite samples, viz., MM(La-cast TiFe), MM (Ce-MA TiFe), and MM ($LaNi_5$-MA TiFe). The findings of hydrogen sorption of the present study are compiled in Table 8.1.

Table 8.1: Compilation of the activation and hydrogen desorption kinetics of the present work.

Synthesis process	**Samples**	**Absorption (wt%) @ RT & 20 bar**	**Desorption (wt%) @ RT & 5 kPa**
TiFe by arc melting followed by 15 min MM with additives	MM (La-cast TiFe)	1.0 (20 h)	0.70 (5 h)
	MM (Ce-cast TiFe)	1.2 (1 h)	0.80 (1 h)
	MM ($LaNi_5$-cast TiFe)	0.9 (6 h)	0.87 (1 h)
TiFe by arc melting followed by 15 min MM	MM-cast TiFe	1.0 (3h)	0.77 (1 h)
MA TiFe followed by 15 min MM with additives	MM (La-MA TiFe)	1.3 (3 h)	0.50 (1 h)
	MM (Ce-MA TiFe)	1.0 (10 h)	0.15 (5 h)
	MM ($LaNi_5$-MA TiFe)	1.0 (24 h)	0.50 (1 h)
Mechanical alloying	MA TiFe	0.4 (48 h)	-
Mechanical alloying	MA TiFe-La	1.35 (0.5 h)	0.80 (0.2 h)

Upon comparison with the literature reported results of Tables 2.1 and 2.2, the enhancement in the activation of the composite samples are comparable to the studies reported with Zr, Zr_7Ni_{10}, Cr and Hf as additive. The activation of the samples that appeared relatively slower, resembled the findings reported on Y

and Mn-added TiFe alloys. Incomplete desorption was observed for all the samples at room temperature under 5 kPa except for the sample MM ($LaNi_5$-cast TiFe), where there was a negligible loss in the reversible desorption capacity. In La-added TiFe samples, the loss in capacity is attributed to the formation of the stable LaH_3 phase. The formation of LaH_3 facilitated by heterogeneous nucleation acted as a gateway for hydrogenation in La-added TiFe samples. The reason for incomplete desorption in all the other samples were unclear.

Crystal structural analysis confirmed the presence of TiFe phase in all samples. High temperature β-La phase which is FCC was observed instead of room temperature α-La which is HCP when La was added by MM to pre-synyhesized TiFe alloy. To our surprise, α-La was observed in MA TiFe-La sample whose synthesis involved 5 h ball milling. The presence of CeO_2 was observed in Ce added TiFe instead of elemental Ce for as-synthesized and de-hydrided state. The milling process only induced microstrain in the $LaNi_5$-added TiFe. The crystallite size of milled TiFe samples was below 10 nm compared to 16 nm for cast sample. Besides the reduction of crystallite size, milling has the effect of reducing microstrain in pure TiFe while increasing it for TiFe with additives.

8.2 Major contributions

Our findings reveal that the process of synthesis has had a considerable impact on the properties of the primary matrix, the TiFe alloy, in comparison to the effect of additives. The introduction of additives by mechanical milling (MM) into the pre-synthesized TiFe via mechanical milling (MA) has proven to be less favorable due to its susceptibility towards oxidation. On the other hand, incorporation of additives through MM into cast TiFe turned out to give favourable hydrogen sorption properties. Therefore, incorporating additives through mechanical milling into alloys synthesized by casting may present a promising synthesis method, particularly when the melting point of the additives is much lower than that of the primary alloy.

8.3 Future scopes

- For all samples, the bulk abundance of Ti is slightly higher than the nominal value, while the Fe abundance is lower. The abundance of the additive is somewhat higher. An investigation with different milling times may provide some clues for the mechanism.

- For samples where Ce has been added to pre-synthesized TiFe via either casting and MA, the CeO_2 phase was present in the as-synthesized and de-hydride state. The mechanism of how stable CeO_2 helped in activation is not clear at this point, but it was probably due to the role played by the phase boundaries between TiFe and CeO_2. An interesting further study would be to know how CeO_2 helped in activation. With varying the amount of Ce, the role played by the said phase boundaries can be verified. Besides, an in-situ investigation coupled with analytical characterization could provide some clues for the activation mechanism involving CeO_2.

- We opted to introduce 16 wt% of additives (corresponds to 10 at% of $LaNi_5$ and 6.6 at% of La or Ce). Varying the amount of additives for an optimum concentration leading to a maximum hydrogen capacity without activation penalty can be investigated.

APPENDIX A

Appendix

A.1 Materials specification

The crystallographic data of the elements and alloys encountered during this study are presented in Table A.1.

Table A.1: Crystallographic data of the investigated elements and alloys.

Space-group	**Elements/alloys**	**Structure type**	**Space group number**
Pm-3m	TiFe	Primitive cubic	221
Im-3m	Fe	Body centred cubic	229
$P6_3/mmc$	Ti, α-La, Ce	Hexagonal closed packing	194
P6/mmm	$LaNi_5$	Hexagonal closed packing	191
Fm-3m	LaH_3, CeO_2, β-La	Face centred cubic	225

A.2 Weight percent ⇌ atomic percent

Alloy compositions are typically specified by the individual elements' weight percent (wt%) or atomic percent (at%). Attributing atomic percentages (at%) to a problem regarding the interaction of individual atoms within a given species is acceptable. This is when it affects the optical, chemical, electrical, physical, etc., properties that are being considered. For actual manufacturing, however, atomic fractions cannot be measured very easily. We must deal with weight percentages (wt%) to manufacture an alloy or composite material because weighing individual components in grams rather than atoms is much easier. Therefore, it is necessary to convert from at% to wt% or vice versa.

It is quite easy to convert atomic percent (at%) to weight percent (wt%) or vice versa by using the atomic weight of the constituents. For instance, if we have two elemental constituents, we can convert from at% to w% and w% to at% by the equations given below:

$$\text{wt\% of x} = \frac{(\text{at\% x})(\text{atomic weight of x}) \cdot 100}{(\text{at\% of x})(\text{atomic weight of x}) + (\text{at\% of y})(\text{atomic weight of y})} \tag{A.1}$$

$$\text{at\% of x} = \frac{(\text{wt\% of x})/(\text{atomic weight of x}) \cdot 100}{(\text{wt\% of x})/(\text{atomic weight of x}) + (\text{wt\% of y})/(\text{atomic weight of y})} \tag{A.2}$$

Similarly, the value for y can be calculated using the same method.

A.3 Error analysis

The error analysis considering the ideal gas behavior of hydrogen is presented below:

Suppose n is the number of moles of hydrogen absorbed,

$$n = f(P, V, T) \tag{A.3}$$

Where P, V, T stands for pressure, volume, and temperature, respectively.
Assuming that the number of moles of hydrogen present in the system at any instant is n_1 and at the equilibrium state it is n_2. Then the number of moles of hydrogen absorbed, $n = n_1 - n_2$. Where,

$$n_1 = \left(\frac{P_1 V_1}{R T_1}\right) \tag{A.4}$$

$$n_2 = \left(\frac{P_2 V_2}{R T_2}\right) \tag{A.5}$$

The effect of each parameter on the uncertainty could be determined by the partial derivative of n w.r.t to the variables P, V, T [138].

$$\frac{\partial n}{\partial P} = \left(\frac{V_1}{R T_1} - \frac{V_2}{R T_2}\right) \tag{A.6}$$

$$\frac{\partial n}{\partial V} = \left(\frac{P_1}{R T_1} - \frac{P_2}{R T_2}\right) \tag{A.7}$$

$$\frac{\partial n}{\partial T} = \left(\frac{P_1 V_1}{R} - \frac{P_2 V_2}{R}\right) \tag{A.8}$$

The cumulative uncertainty is determined by following the rule of error in summation,

$$|\Delta n|^2 = |\frac{\partial n}{\partial P}|^2 \Delta P^2 + |\frac{\partial n}{\partial V}|^2 \Delta P^2 + |\frac{\partial n}{\partial T}|^2 \Delta T^2 \tag{A.9}$$

Thus, the determination of cumulative uncertainty will require the values of the error in the measurement of pressure ΔP, volume ΔV, and temperature ΔT along with the values from the equations (A.6) (A.7), and (A.8) [27, 139].

A.4 Rietveld fitting with goodness-of-fit (GOF) parameters

Utilizing Topas software, the XRD patterns of the alloys explored in this thesis were subjected to Rietveld fitting. The resulting fitting with the GOF parameters are provided as follows (peak positions indicated as vertical colored-dashed lines corresponding to the phase name indicated in the same color):

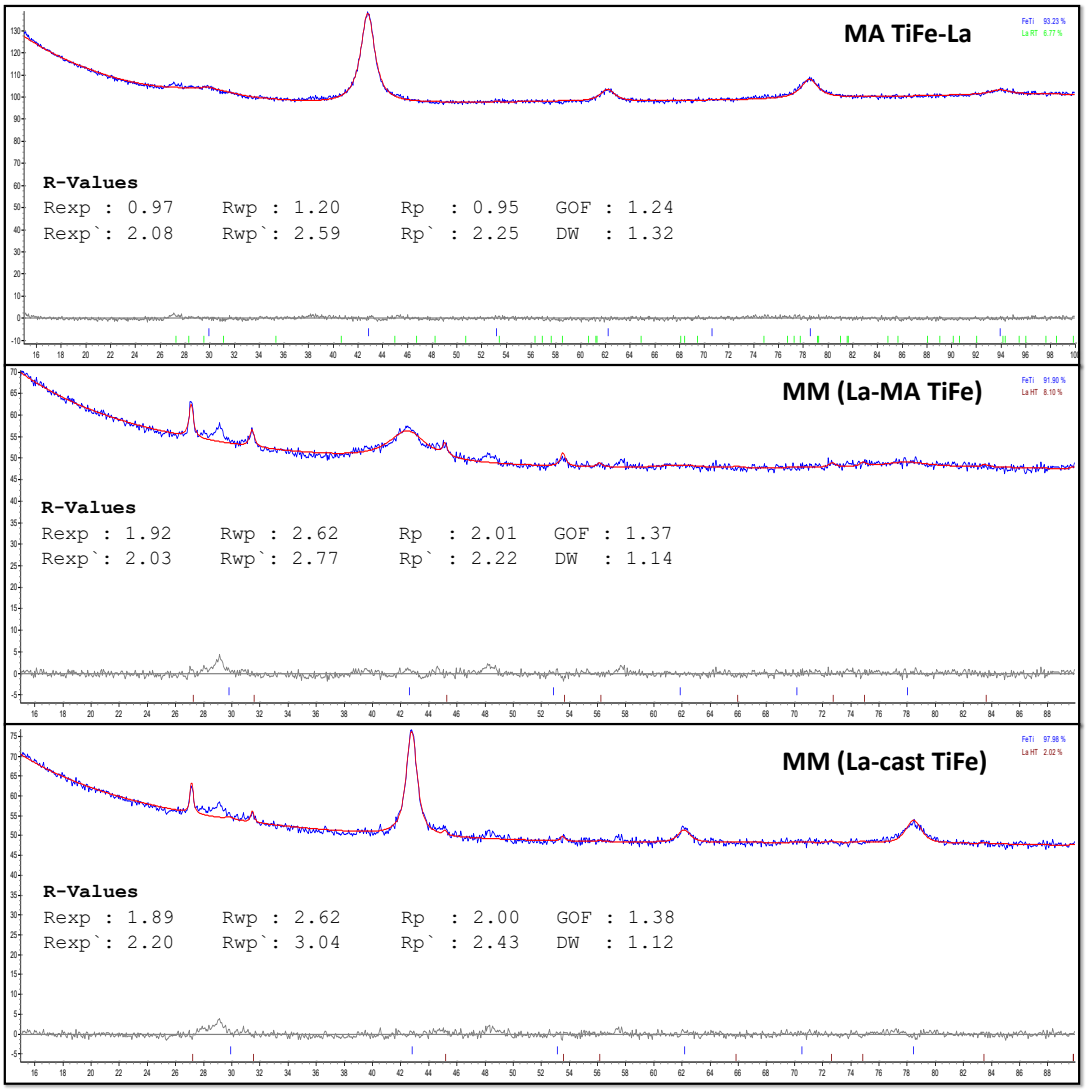

Figure A.1: Rietveld fitting with the GOF parameters of **as-synthesized** La-added TiFe alloy. (Where, La 'RT' is α-La, La 'HT' is β-La)

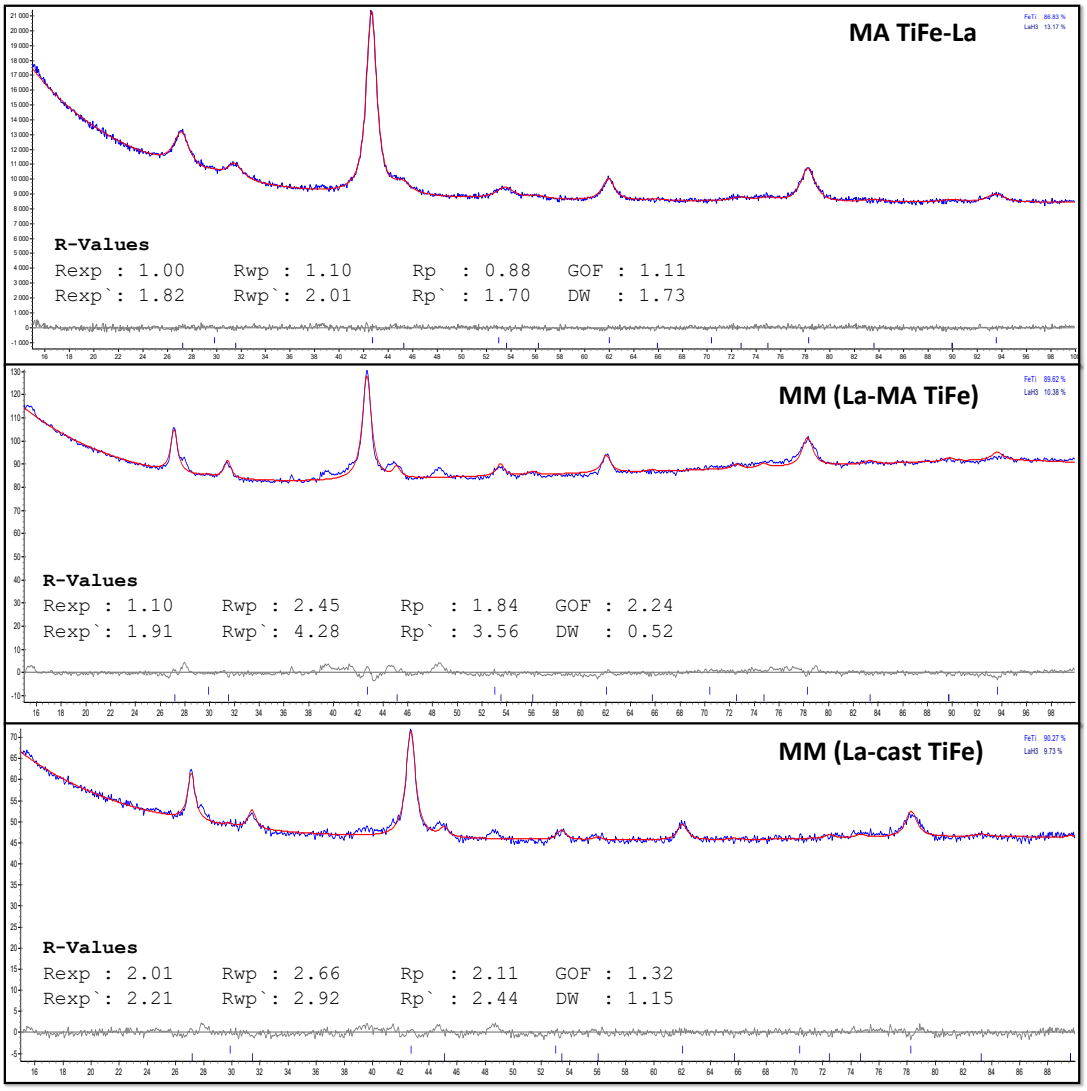

Figure A.2: Rietveld fitting with the GOF parameters of **de-hydrogenated** La-added TiFe alloy.

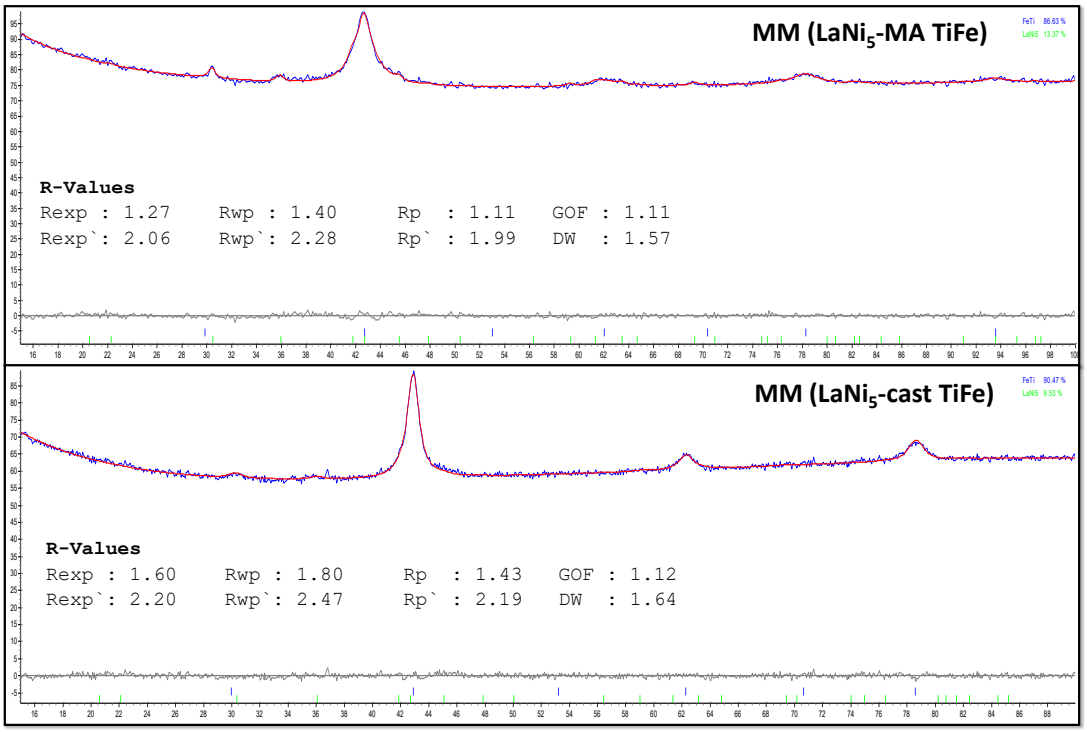

Figure A.3: Rietveld fitting with the GOF parameters of **as-synthesized** $LaNi_5$-added TiFe alloy.

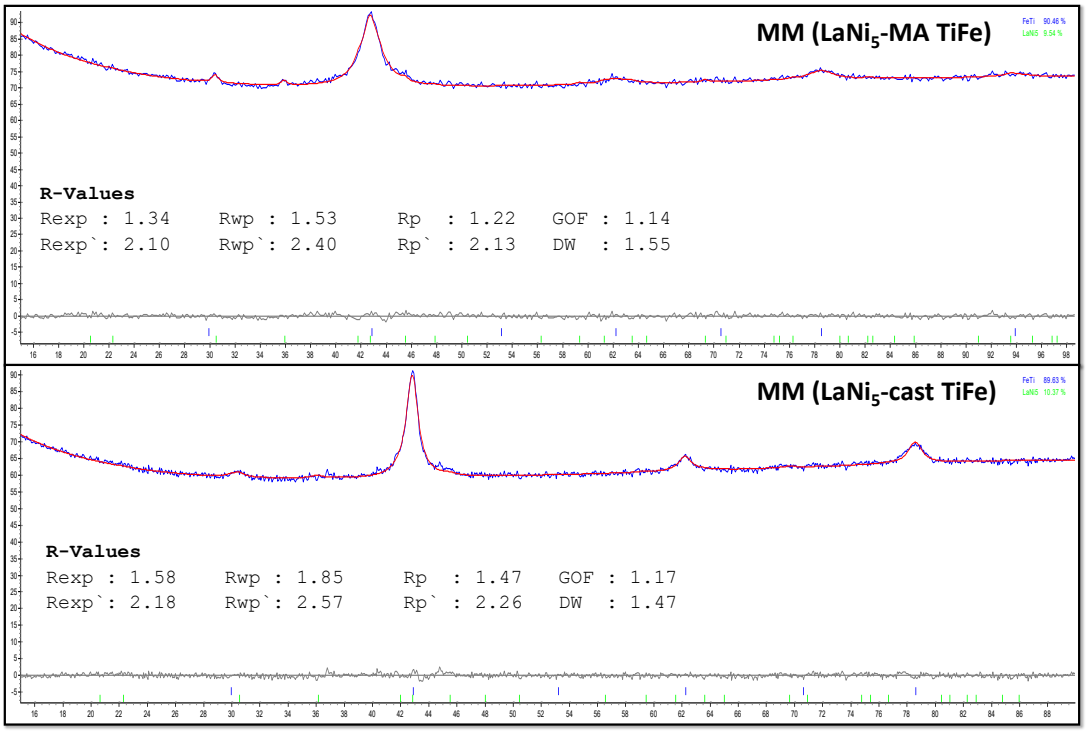

Figure A.4: Rietveld fitting with the GOF parameters of **de-hydrogenated** $LaNi_5$-added TiFe alloy.

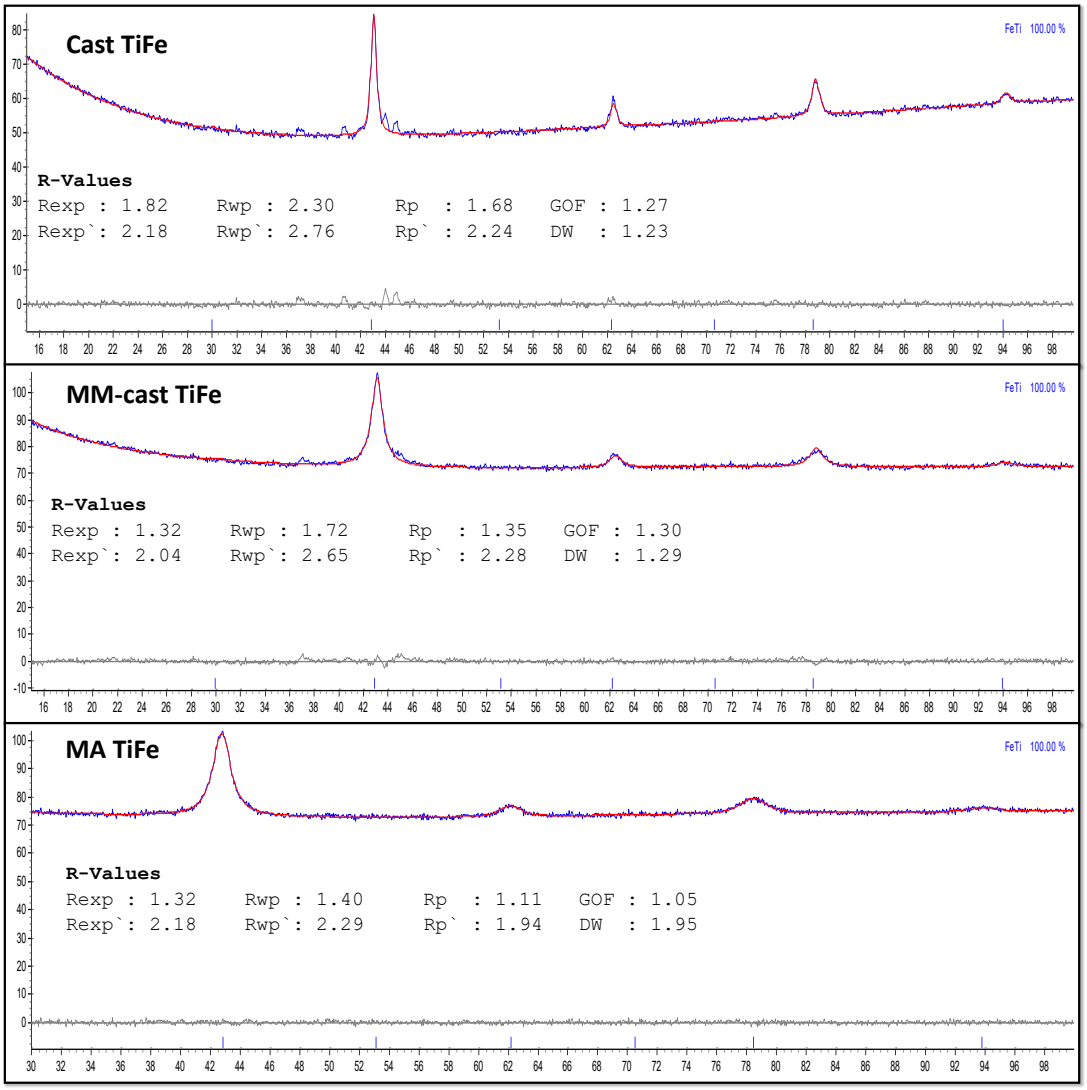

Figure A.5: Rietveld fitting with the GOF parameters of **as-synthesized** TiFe alloys.

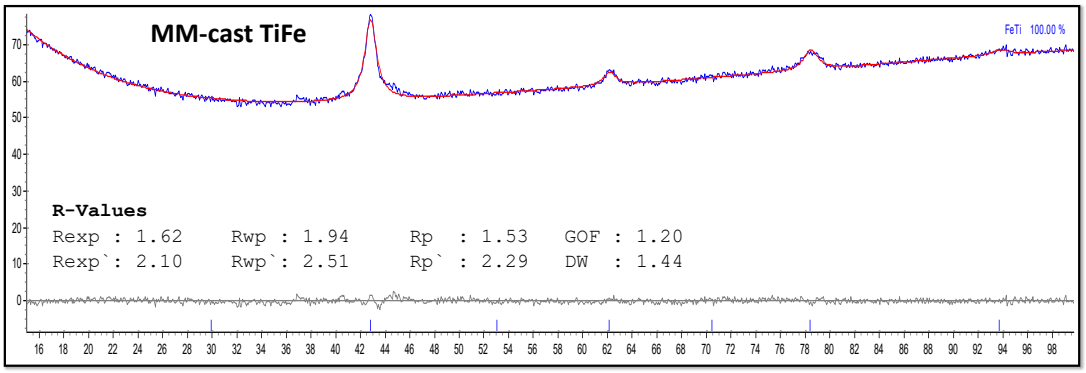

Figure A.6: Rietveld fitting with the GOF parameters of **de-hydrogenated** MM-cast TiFe alloy.

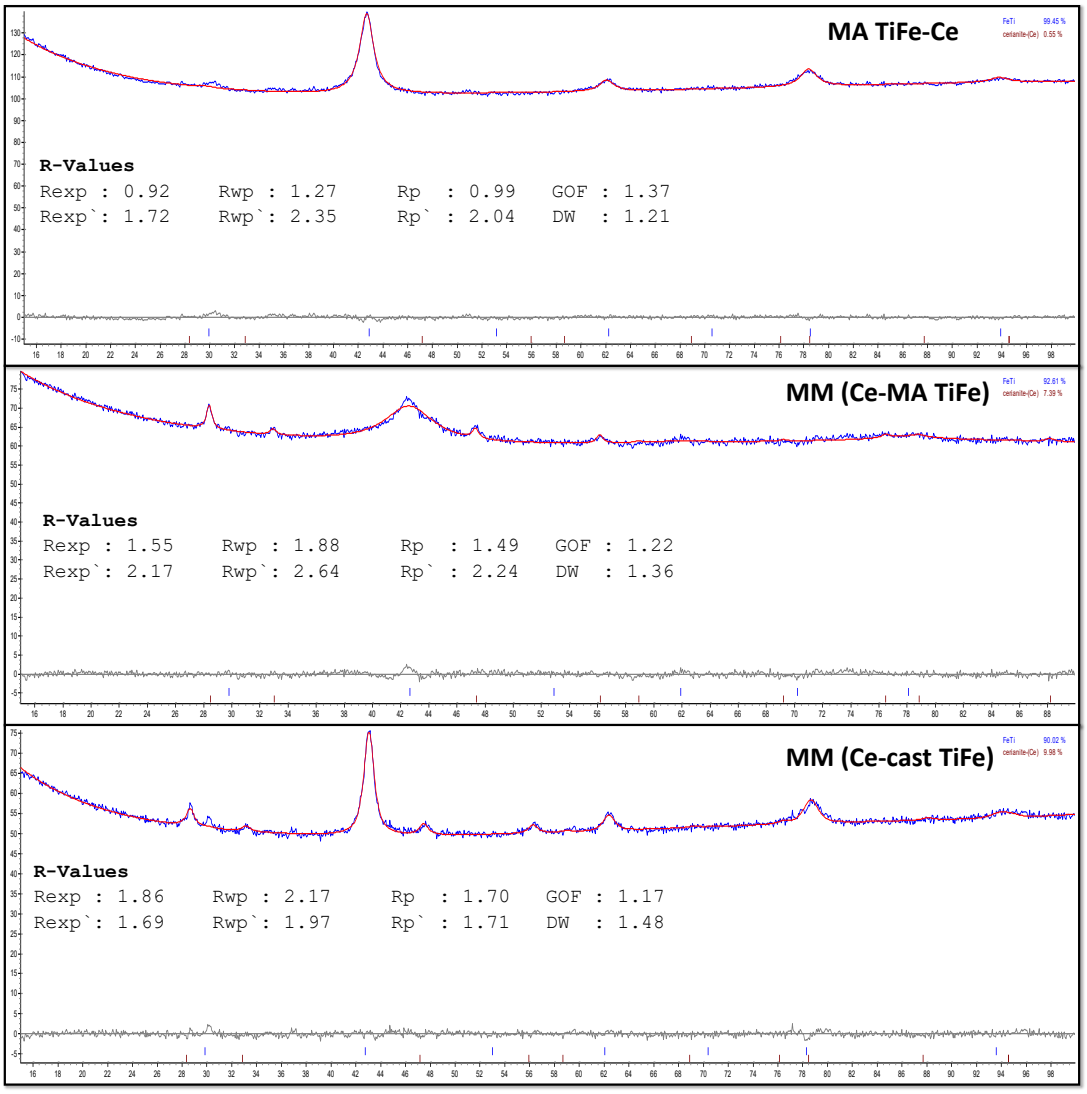

Figure A.7: Rietveld fitting with the GOF parameters of **as-synthesized** Ce-added TiFe alloy.

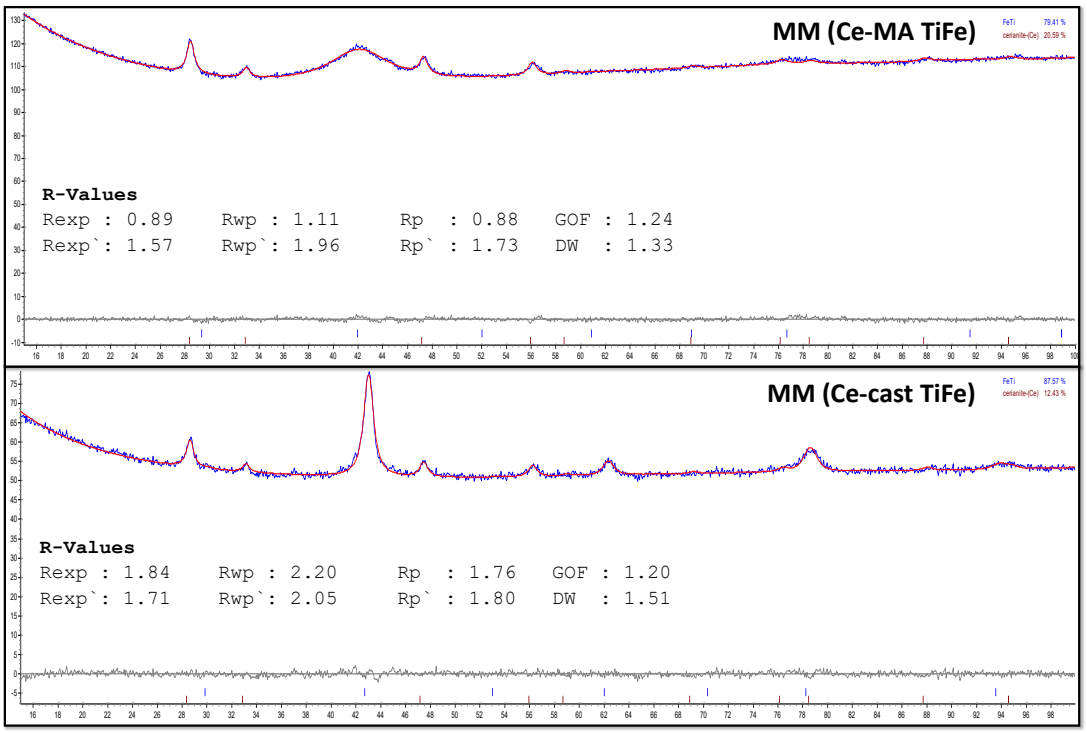

Figure A.8: Rietveld fitting with the GOF parameters of **de-hydrogenated** Ce-added TiFe alloy.

References

[1] J. Reilly and R. Wiswall Jr., "Formation and properties of iron titanium hydride," *Inorganic Chemistry*, vol. 13, no. 1, 1974.

[2] "Understanding the contributions of specific fuels and sectors to GHG emissions associated with combustion of fuels from 1971 to 2020 for over 203 countries and 42 regions," https://www.iea.org/data-and-statistics/data-tools/greenhouse-gas-emissions-from-energy-data-explorer, accessed on: 2021-11-30.

[3] R. B. Gupta, *Hydrogen Fuel: Production, Transport, and Storage*. CRC press, 2008.

[4] "International energy agency. The future of hydrogen - seizing today's opportunities. Technical report 2019," https://www.iea.org/reports/the-future-of-hydrogen, accessed on: 2021-11-30.

[5] L. W. Jones, "Toward a liquid hydrogen fuel economy. Technical report 1970."

[6] "Hydrogen council. How hydrogen empowers the energy transition. Technical report 2017."

[7] "Hydrogen council. Hydrogen- scaling up, a sustainable pathway for the global energy transition. Technical report 2017."

[8] G. Principi, F. Agresti, A. Maddalena, and S. Lo Russo, "The problem of solid state hydrogen storage," *Energy*, vol. 34, no. 12, pp. 2087–2091, 2009.

[9] M. Hirscher, A. Züttel, A. Borgschulte, and L. Schlapbach, "Handbook of hydrogen storage: New materials for future energy storage," *Ceramic Transactions*, vol. 202, 2009.

[10] A. Züttel, A. Remhof, A. Borgschulte, and O. Friedrichs, "Hydrogen: the future energy carrier," *Philosophical Transactions of the Royal Society A: Mathematical, Physical and Engineering Sciences*, vol. 368, no. 1923, pp. 3329–3342, 2010.

[11] J. Lennard-Jones, "Processes of adsorption and diffusion on solid surfaces," *Transactions of the Faraday Society*, vol. 28, pp. 333–359, 1932.

[12] V. A. Blagojević, G. Minić Dejan, J. Grbović Novaković, and M. Minic Dragica, "Hydrogen economy: modern concepts, challenges and perspectives," *Hydrogen Energy–Challenges and Perspectives*, pp. 3–28, 2012.

[13] H. Lüth, *Solid Surfaces, Interfaces and Thin Films*. Springer, 2001, vol. 4.

[14] D. Chandra, "Intermetallics for hydrogen storage," in *Solid-State Hydrogen Storage*. Elsevier, 2008, pp. 315–356.

[15] K. H. Buschow, "Materials science and technology. A comprehensive treatment, vol. 3B, Electronic and magnetic properties of metals and ceramics, pt. 2," Dec 1994.

[16] R. Swalin, *Thermodynamics of Solids*. John Wiley & Sons, New York, NY, 1962.

[17] L. Schlapbach, R. Bowman, N. Gerard, and H. K. Lotsch, *Hydrogen in Intermetallic Compounds II: Surface and Dynamic Properties, Applications*. Springer, 1992, vol. 67.

[18] Y. Fukai, *The Metal-Hydrogen System: Basic Bulk Properties*. Springer Science & Business Media, 2006, vol. 21.

[19] C. Julien, J.-P. Pereira-Ramos, and A. Momchilov, *New Trends in Intercalation Compounds for Energy Storage*. Springer Science & Business Media, 2012, vol. 61.

[20] A. F. Andresen and A. Maeland, *Hydrides for Energy Storage: Proceedings of an International Symposium Held in Geilo, Norway, 14-19 August 1977*. Elsevier, 2013.

[21] J. L. Ericksen, *Introduction to the Thermodynamics of Solids*. Springer, 1998, vol. 275.

[22] M. Hirscher and A. Borgschulte, *Handbook of Hydrogen Storage: New Materials for Future Energy Storage*, 2009.

[23] D. P. Broom, *Hydrogen Storage Materials: The Characterisation of their Storage Properties*. Springer, 2011, vol. 1.

[24] G. Sandrock, "Panoramic overview of hydrogen storage alloys from a gas reaction point of view," *Journal of Alloys and Compounds*, vol. 293, pp. 877–888, 1999.

[25] J. H. Van Vucht, F. Kuijpers, and H. C. Bruning, "Reversible room-temperature absorption of large quantities of hydrogen by intermetallic compounds," *Philips Res. Rep. 25: 133-40 (Apr 1970).*, 1970.

[26] E. M. Borzone, A. Baruj, M. V. Blanco, and G. O. Meyer, "Dynamic measurements of hydrogen reaction with $LaNi_{5-x}Sn_x$ alloys," *International Journal of Hydrogen Energy*, vol. 38, no. 18, pp. 7335–7343, 2013.

[27] V. K. Sharma and E. A. Kumar, "Effect of measurement parameters on thermodynamic properties of La-based metal hydrides," *International Journal of Hydrogen Energy*, vol. 39, no. 11, pp. 5888–5898, 2014.

[28] L. Shcherbakova, M. Spodaryk, Y. Solonin, and A. Samelyuk, "Effects of particle size and type of conductive additive on the electrode performances of gas atomized AB_5-type hydrogen storage alloy," *International Journal of Hydrogen Energy*, vol. 38, no. 27, pp. 12 133–12 139, 2013.

[29] J. Prigent, J.-M. Joubert, and M. Gupta, "Modification of the hydrogenation properties of $LaNi_5$ upon Ni substitution by Rh, Ir, Pt or Au," *Journal of alloys and compounds*, vol. 511, no. 1, pp. 95–100, 2012.

[30] K. Young, B. Chao, B. Huang, and J. Nei, "Effects of Cu-substitution on $La_{0.62}Ce_{0.38}(NiCoMnAlSiZr)_{5.3}$ metal hydride alloy," *Journal of alloys and compounds*, vol. 588, pp. 235–241, 2014.

[31] A. Fossdal, H. Brinks, M. Fichtner, and B. Hauback, "Thermal decomposition of $Mg(AlH_4)_2$ studied by in situ synchrotron X-ray diffraction," *Journal of Alloys and Compounds*, vol. 404, pp. 752–756, 2005.

[32] K. Komiya, N. Morisaku, Y. Shinzato, K. Ikeda, S. Orimo, Y. Ohki, K. Tatsumi, H. Yukawa, and M. Morinaga, "Synthesis and dehydrogenation of $M(AlH_4)_2$ (M= Mg, Ca)," *Journal of Alloys and Compounds*, vol. 446, pp. 237–241, 2007.

[33] J. Wang, A. D. Ebner, and J. A. Ritter, "On the reversibility of hydrogen storage in novel complex hydrides," *Adsorption*, vol. 11, pp. 811–816, 2005.

[34] A. Klaveness, P. Vajeeston, P. Ravindran, H. Fjellvåg, and A. Kjekshus, "Structural phase stability and bonding behavior of $BAlH_5$ (B= Mg, Ba) from first-principles calculations," *Physical Review B*, vol. 73, no. 9, p. 094122, 2006.

[35] H. C. Brown, B. Abraham, A. Bond, N. Davidson, A. Finholt, J. R. Gilbreath, H. Hoekstra, L. Horvitz, E. K. Hyde *et al.*, "New developments in the chemistry of diborane and the borohydrides. I. general summary," *Journal of the American Chemical Society*, vol. 75, no. 1, pp. 186–190, 1953.

[36] R. Varin, C. Chiu, T. Czujko, and Z. Wronski, "Mechano-chemical activation synthesis (MCAS) of nanocrystalline magnesium alanate hydride $[Mg(AlH_4)_2]$ and its hydrogen desorption properties," *Journal of Alloys and Compounds*, vol. 439, no. 1-2, pp. 302–311, 2007.

[37] M. Mintz, Z. Gavra, G. Kimmel, and Z. Hadari, "The reaction of hydrogen with magnesium alloys and magnesium intermetallic compounds," *Journal of the Less Common Metals*, vol. 74, no. 2, pp. 263–270, 1980.

[38] G. Principi, F. Agresti, A. Maddalena, and S. L. Russo, "The problem of solid state hydrogen storage," *Energy*, vol. 34, no. 12, pp. 2087–2091, 2009.

[39] F. Stein, M. Palm, and G. Sauthoff, "Structure and stability of laves phases. Part I. Critical assessment of factors controlling laves phase stability," *Intermetallics*, vol. 12, no. 7-9, pp. 713–720, 2004.

[40] Z. Gavra, Z. Hadari, and M. Mintz, "Effects of nickel and indium ternary additions on the hydrogenation of Mg-Al intermetallic compounds," *Journal of Inorganic and Nuclear Chemistry*, vol. 43, no. 8, pp. 1763–1768, 1981.

[41] L. Schlapbach and a. Züttel, "Hydrogen-storage materials for mobile applications." *Nature*, vol. 414, no. 6861, pp. 353–358, 2001.

[42] T. Maeda, T. Fuura, I. Matsumoto, Y. Kawakami, and M. Masuda, "Cyclic stability test of ab_2 type (ti, zr)(ni, mn, v, fe)$_{2.18}$ for stationary hydrogen storage in water contaminated hydrogen," *Journal of Alloys and Compounds*, vol. 580, pp. S255–S258, 2013.

[43] M. Okada, T. Kuriiwa, A. Kamegawa, and H. Takamura, "Role of intermetallics in hydrogen storage materials," *Materials Science and Engineering A*, vol. 329-331, pp. 305–312, 2002.

[44] N. Endo, H. Saitoh, A. Machida, and Y. Katayama, "Formation of BCC TiFe hydride under high hydrogen pressure," *International Journal of Hydrogen Energy*, vol. 38, no. 16, pp. 6726–6729, 2013.

[45] L. Pickering, J. Li, D. Reed, A. I. Bevan, and D. Book, "Ti–V–Mn based metal hydrides for hydrogen storage," *Journal of Alloys and Compounds*, vol. 580, pp. S233–S237, 2013.

[46] J. De Castro, S. Santos, A. Costa, A. Yavari, T. Ishikawa *et al.*, "Structural characterization and dehydrogenation behavior of Mg–5 at.% Nb nano-composite processed by reactive milling," *Journal of Alloys and Compounds*, vol. 376, no. 1-2, pp. 251–256, 2004.

[47] M. Dornheim, S. Doppiu, G. Barkhordarian, U. Boesenberg, T. Klassen, O. Gutfleisch, and R. Bormann, "Hydrogen storage in magnesium-based hydrides and hydride composites," *Scripta Materialia*, vol. 56, no. 10, pp. 841–846, 2007.

[48] G. Libowitz, "Metallic hydrides; fundamental properties and applications," *Journal of Physics and Chemistry of Solids*, vol. 55, no. 12, pp. 1461–1470, 1994.

[49] F. Schlapbach, L.; Seiler, A.; Stucki, "Surface Segregation in FeTi and its Catalytic Effect on the Hydrogenation," *Mat. Res. Bull*, vol. 13, no. 4, pp. 697–706, 1978.

[50] T. Schober and D. G. Westlake, "The activation of FeTi for hydrogen storage: A different view," *Scripta Metallurgica*, vol. 15, no. 8, pp. 913–918, 1981.

[51] P. Jain, C. Gosselin, N. Skryabina, D. Fruchart, and J. Huot, "Hydrogenation properties of TiFe with Zr_7Ni_{10} alloy as additive," *Journal of Alloys and Compounds*, vol. 636, pp. 375–380, 2015.

[52] P. Jain, C. Gosselin, and J. Huot, "Effect of Zr, Ni and Zr_7Ni_{10} alloy on hydrogen storage characteristics of TiFe alloy," in *International Journal of Hydrogen Energy*. Elsevier, 2015, pp. 16 921–16 927.

[53] S. Kumar, G. P. Tiwari, S. Sonak, U. Jain, and N. Krishnamurthy, "High performance FeTi - 3.1 mass % V alloy for on board hydrogen storage solution," *Energy*, vol. 75, pp. 520–524, 2014.

[54] X. Wang, R. Chen, C. Chen, and Q. Wang, "Hydrogen storage properties of Ti_xFe + y wt.% La and its use in metal hydride hydrogen compressor," *Journal of Alloys and Compounds*, vol. 425, no. 1-2, pp. 291–295, 2006.

[55] H. Leng, Z. Yu, J. Yin, Q. Li, Z. Wu, and K. C. Chou, "Effects of Ce on the hydrogen storage properties of $TiFe_{0.9}Mn_{0.1}$ alloy," *International Journal of Hydrogen Energy*, vol. 42, no. 37, pp. 23 731–23 736, 2017.

[56] H. Aoyagi, K. Aoki, and T. Masumoto, "Effect of ball milling on hydrogen absorption properties of FeTi, Mg_2Ni and $LaNi_5$," *Journal of Alloys and compounds*, vol. 231, no. 1-2, pp. 804–809, 1995.

[57] H. Emami, K. Edalati, J. Matsuda, E. Akiba, and Z. Horita, "Hydrogen storage performance of TiFe after processing by ball milling," *Acta Materialia*, vol. 88, pp. 190–195, 2015.

[58] K. Edalati, J. Matsuda, A. Yanagida, E. Akiba, and Z. Horita, "Activation of TiFe for hydrogen storage by plastic deformation using groove rolling and high-pressure torsion: Similarities and differences," *International Journal of Hydrogen Energy*, vol. 39, no. 28, pp. 15 589–15 594, 2014.

[59] K. Edalati, J. Matsuda, H. Iwaoka, S. Toh, E. Akiba, and Z. Horita, "High-pressure torsion of TiFe intermetallics for activation of hydrogen storage at room temperature with heterogeneous nanostructure," *International Journal of Hydrogen Energy*, vol. 38, no. 11, pp. 4622–4627, apr 2013.

[60] L. Vega, D. Leiva, R. L. Neto, W. Silva, R. Silva, T. Ishikawa, C. Kiminami, and W. Botta, "Mechanical activation of TiFe for hydrogen storage by cold rolling under inert atmosphere," *International Journal of Hydrogen Energy*, vol. 43, no. 5, pp. 2913–2918, 2018.

[61] M. Tousignant and J. Huot, "Hydrogen sorption enhancement in cold rolled $LaNi_5$," *Journal of Alloys and Compounds*, vol. 595, pp. 22–27, 2014.

[62] P. Lv and J. Huot, "Hydrogen storage properties of $Ti_{0.95}FeZr_{0.05}$, $TiFe_{0.95}Zr_{0.05}$ and $TiFeZr_{0.05}$ alloys," *International Journal of Hydrogen Energy*, vol. 41, no. 47, pp. 22 128–22 133, 2016.

[63] A. K. Patel, P. Sharma, and J. Huot, "Effect of annealing on microstructure and hydrogenation properties of TiFe + X wt% Zr (X = 4, 8)," *International Journal of Hydrogen Energy*, vol. 43, no. 12, pp. 6238–6243, 2018.

[64] A. K. Patel, B. Tougas, P. Sharma, and J. Huot, "Effect of cooling rate on the microstructure and hydrogen storage properties of TiFe with 4 wt% Zr as an additive," *Journal of Materials Research and Technology*, vol. 8, no. 6, pp. 5623–5630, 2019.

[65] A. K. Patel, A. Duguay, B. Tougas, C. Schade, P. Sharma, and J. Huot, "Microstructure and first hydrogenation properties of TiFe alloy with Zr and Mn as additives," *International Journal of Hydrogen Energy*, vol. 45, no. 1, pp. 787–797, 2020.

[66] J. Manna, B. Tougas, and J. Huot, "Mechanical activation of air exposed TiFe + 4 wt% Zr alloy for hydrogenation by cold rolling and ball milling," *International Journal of Hydrogen Energy*, vol. 43, no. 45, pp. 20 795–20 800, 2018.

[67] V. Razafindramanana, S. Gorsse, J. Huot, and J. L. Bobet, "Effect of Hafnium Addition on the Hydrogenation Process of TiFe Alloy," *Energies*, vol. 12, no. 18, p. 3477, 2019.

[68] C. Gosselin, D. Santos, and J. Huot, "First hydrogenation enhancement in TiFe alloys for hydrogen storage," *Journal of Physics D: Applied Physics*, 2017.

[69] C. Gosselin and J. Huot, "First hydrogenation enhancement in TiFe alloys for hydrogen storage doped with yttrium," *Metals*, vol. 9, no. 2, pp. 1–9, 2019.

[70] E. Berdonosova, V. Y. Zadorozhnyy, M. Y. Zadorozhnyy, K. Geodakian, M. Zheleznyi, A. Tsarkov, S. Kaloshkin, and S. Klyamkin, "Hydrogen storage properties of TiFe-based ternary mechanical alloys with cobalt and niobium. A thermochemical approach," *International Journal of Hydrogen Energy*, vol. 44, no. 55, pp. 29 159–29 165, 2019.

[71] M. Y. Zadorozhnyi, S. Kaloshkin, S. Klyamkin, O. Bermesheva, and V. Y. Zadorozhnyi, "Mechanochemical synthesis of a TiFe nanocrystalline intermetallic compound and its mechanical alloying with third component," *Metal Science and Heat Treatment*, vol. 54, pp. 461–465, 2013.

[72] V. Y. Zadorozhnyy, S. N. Klyamkin, M. Yu. Zadorozhnyy, M. V. Gorshenkov, and S. D. Kaloshkin, "Mechanical alloying of nanocrystalline intermetallic compound TiFe doped by aluminium and chromium," *Journal of Alloys and Compounds*, vol. 586, pp. S56–S60, 2014.

[73] V. Y. Zadorozhnyy, S. Klyamkin, M. Y. Zadorozhnyy, M. Gorshenkov, and S. Kaloshkin, "Mechanical alloying of nanocrystalline intermetallic compound TiFe doped with sulfur and magnesium," *Journal of Alloys and Compounds*, vol. 615, pp. S569–S572, 2014.

[74] A. Van der Kraan and K. Buschow, "The ^{57}Fe mössbauer isomer shift in intermetallic compounds of iron," *Physica B+C*, vol. 138, no. 1-2, pp. 55–62, 1986.

[75] O. Toma, M. Dzevenko, A. Oliynyk, and Y. Lomnytska, "The Ti-Fe-P system: phase equilibria and crystal structure of phases," *Open Chemistry*, vol. 11, no. 9, pp. 1518–1526, 2013.

[76] K. Takahashi and S. Isobe, "Enhancing the hydrogen storage capacity of TiFe by utilizing clusters," *Phys Chem Chem Phys*, vol. 16, no. 31, pp. 16 765–16 770, 2014.

[77] G. Sujan, Z. Pan, H. Li, D. Liang, and N. Alam, "An overview on tife intermetallic for solid-state hydrogen storage: microstructure, hydrogenation and fabrication processes," *Critical Reviews in Solid State and Materials Sciences*, vol. 45, no. 5, pp. 410–427, 2020.

[78] P. Thompson, M. Pick, F. Reidinger, L. Corliss, J. Hastings, and J. Reilly, "Neutron diffraction study of β iron titanium deuteride," *Journal of Physics F: Metal Physics*, vol. 8, no. 4, p. L75, 1978.

[79] P. Fischer, J. Schefer, K. Yvon, L. Schlapbach, and T. Riesterer, "Orthorhombic structure of γ-tifed$_2$," *Journal of the Less Common Metals*, vol. 129, pp. 39–45, 1987.

[80] K. Benyelloul, Y. Bouhadda, M. Bououdina, H. Faraoun, H. Aourag, and L. Seddik, "The effect of hydrogen on the mechanical properties of FeTi for hydrogen storage applications," *International Journal of Hydrogen Energy*, vol. 39, no. 24, pp. 12 667–12 675, 2014.

[81] G. Cacciamani, J. De Keyzer, R. Ferro, U. E. Klotz, J. Lacaze, and P. Wollants, "Critical evaluation of the Fe–Ni, Fe–Ti and Fe–Ni–Ti alloy systems," *Intermetallics*, vol. 14, no. 10-11, pp. 1312–1325, 2006.

[82] J. L. Murray, "The Fe-Ti (Iron–Titanium) system," *Bulletin of Alloy Phase Diagrams*, vol. 2, no. 3, pp. 320–334, 1981.

[83] V. Y. Zadorozhnyy, G. Milovzorov, S. Klyamkin, M. Y. Zadorozhnyy, D. Strugova, M. Gorshenkov, and S. Kaloshkin, "Preparation and hydrogen storage properties of nanocrystalline TiFe synthesized by mechanical alloying," *Progress in Natural Science: Materials International*, vol. 27, no. 1, pp. 149–155, 2017.

[84] V. Zadorozhnyy, S. Klyamkin, M. Zadorozhnyy, O. Bermesheva, and S. Kaloshkin, "Hydrogen storage nanocrystalline TiFe intermetallic compound: Synthesis by mechanical alloying and compacting," *International Journal of Hydrogen Energy*, vol. 37, no. 22, pp. 17 131–17 136, 2012.

[85] L. Zaluski, P. Tessier, D. H. Ryan, C. B. Doner, A. Zaluska, M. L. Ström-Olsen, J. O. Trudeau, and R. Schulz, "Amorphous and nanocrisystalline Fe-Ti prepared by ball milling," *Journal of Materials Research*, vol. 8, no. 12, pp. 3059–3068, 1993.

[86] P. Tessier, L. Zaluski, M. L. Trudeau, and R. Schulz, "Transformations and hydrogen storage in ball-milled iron-titanium," *Mat. Res. Soc. Symp. Proc.*, vol. 286, pp. 209–214, 1993.

[87] L. Zaluski, A. Zaluska, P. Tessier, J. Ström-Olsen, and R. Schulz, "Effects of relaxation on hydrogen absorption in Fe-Ti produced by ball-milling," *Journal of Alloys and Compounds*, vol. 227, no. 1, pp. 53–57, aug 1995.

[88] P. Lv, M. N. Guzik, S. Sartori, and J. Huot, "Effect of ball milling and cryomilling on the microstructure and first hydrogenation properties of TiFe+4 wt.% Zr alloy," *Journal of Materials Research and Technology*, vol. 8, no. 2, pp. 1828–1834, 2019.

[89] H. Hotta, M. Abe, T. Kuji, and H. Uchida, "Synthesis of Ti–Fe alloys by mechanical alloying," *Journal of Alloys and Compounds*, vol. 439, no. 1-2, pp. 221–226, jul 2007.

[90] M. Abe and T. Kuji, "Hydrogen absorption of TiFe alloy synthesized by ball milling and post-annealing," *Journal of Alloys and Compounds*, vol. 446, no. 447, pp. 200–203, 2007.

[91] K. Edalati, J. Matsuda, M. Arita, T. Daio, E. Akiba, and Z. Horita, "Mechanism of activation of TiFe intermetallics for hydrogen storage by severe plastic deformation using high-pressure torsion," *Applied Physics Letters*, vol. 103, no. 14, 2013.

[92] L. Zaluski, a. Zaluska, P. Tessier, J. Ström-Olsen, and R. Schulz, "Investigation of structural relaxation by hydrogen absorption in ball-milled alloys," *Materials Science Forum*, vol. 225-227, pp. 875–880, 1996.

[93] L. Zaluski, S. Hosatte, P. Tessier, D. Ryan, J. Ström-Olsen, M. Trudeau, and R. Schulz, "Hydrogen absorption in amorphous and nano-crystalline FeTi," *Zeitschrift für Physikalische Chemie*, vol. 183, no. 1-2, pp. 45–49, 1994.

[94] P. Tessier, L. Zaluski, a. Zaluska, J. Ström-Olsen, and R. Schulz, "Effect of Compositional Variations on Hydrogen Storage in Ball-Milled Fe-Ti," *Materials Science Forum*, vol. 225-227, pp. 869–874, 1996.

[95] M. Trudeau, L. Dignard-Bailey, R. Schulz, P. Tessier, L. Zaluski, D. Ryan, and J. Strom-Olsen, "The oxidation of nanocrystalline FeTi hydrogen storage compounds," *Nanostructured Materials*, vol. 1, no. 6, pp. 457–464, nov 1992.

[96] M. H. Mintz, S. Vaknin, S. Biderman, and Z. Hadari, "Hydrides of ternary $TiFe_xM_{1-x}$(M = Cr, Mn, Co, Ni) intermetallics," *Journal of Applied Physics*, vol. 52, no. 1, pp. 463–467, 1981.

[97] S. M. Lee and T. P. Perng, "Microstructural correlations with the hydrogenation kinetics of $FeTi_{1+x}$ alloys," *Journal of Alloys and Compounds*, vol. 177, no. 1, pp. 107–118, 1991.

[98] A. K. Patel, A. Duguay, B. Tougas, B. Neumann, C. Schade, P. Sharma, and J. Huot, "Study of the microstructural and first hydrogenation properties of TiFe alloy with Zr, Mn and V as additives," *Processes*, vol. 9, no. 7, 2021.

[99] P. Lv and J. Huot, "Hydrogenation improvement of TiFe by adding $ZrMn_2$," *Energy*, vol. 138, pp. 375–382, 2017.

[100] L. L. Jewell and B. H. Davis, "Review of absorption and adsorption in the hydrogen-palladium system," *Applied Catalysis A: General*, vol. 310, no. 1-2, pp. 1–15, 2006.

[101] M. Bououdina, D. Fruchart, S. Jacquet, L. Pontonnier, and J. L. Soubeyroux, "Effect of nickel alloying by using ball milling on the hydrogen absorption properties of TiFe," *International Journal of Hydrogen Energy*, vol. 24, pp. 885–890, 1999.

[102] S. Lim and L. Jai-Young, "The effects of the addition of aluminium on the kinetic properties of the intermetallic compound TiFe," *Journal of the Less Common Metals*, vol. 97, pp. 59–64, 1984.

[103] G. Bruzzone, G. Costa, M. Ferretti, and G. Olcese, "Hydrogen storage in aluminium-substituted TiFe compounds," *International Journal of Hydrogen Energy*, vol. 6, no. 2, pp. 181–184, 1981.

[104] J. Ma, H. Pan, X. Wang, C. Chen, and Q. Wang, "Hydrogen storage properties of $FeTi_{1.3}$ + x wt% Mm (x = 0.0, 1.5, 3.0, 4.5, 6.0) hydrogen storage alloys," *International Journal of Hydrogen Energy*, vol. 25, no. 8, pp. 779–782, 2000.

[105] Z. Han, Z. Yuan, T. Zhai, D. Feng, H. Sun, and Y. Zhang, "Effect of yttrium content on microstructure and hydrogen storage properties of TiFe-based alloy," *International Journal of Hydrogen Energy*, vol. 48, no. 2, pp. 676–695, 2023.

[106] C. Li, Y. Lan, X. Wei, W. Zhang, B. Liu, X. Gao, and Z. Yuan, "Improvement of hydrogen absorption and desorption properties of TiFe-based alloys by adding yttrium," *Journal of Alloys and Compounds*, vol. 927, p. 166992, 2022.

[107] H. Shang, Y. Zhang, Y. Li, J. Gao, W. Zhang, X. Wei, Z. Yuan, and L. Ju, "Effect of Pr content on activation capability and hydrogen storage performances of TiFe alloy," *Journal of Alloys and Compounds*, vol. 890, p. 161785, 2022.

[108] Y. Zhang, H. Shang, J. Gao, W. Zhang, X. Wei, and Z. Yuan, "Effect of Sm content on activation capability and hydrogen storage performances of TiFe alloy," *International Journal of Hydrogen Energy*, vol. 46, no. 48, pp. 24 517–24 530, 2021.

[109] T. Yang, P. Wang, C. Xia, N. Liu, C. Liang, F. Yin, and Q. Li, "Effect of chromium, manganese and yttrium on microstructure and hydrogen storage properties of TiFe-based alloy," *International Journal of Hydrogen Energy*, vol. 45, no. 21, pp. 12 071–12 081, 2020.

[110] W. Ali, Z. Hao, Z. Li, G. Chen, Z. Wu, X. Lu, and C. Li, "Effects of Cu and Y substitution on hydrogen storage performance of $TiFe_{0.86}Mn_{0.1}Y_{0.1\text{-}x}Cu_x$," *International Journal of Hydrogen Energy*, vol. 42, no. 26, pp. 16 620–16 631, 2017.

[111] W. Ali, M. Li, P. Gao, C. Wu, Q. Li, X. Lu, and C. Li, "Hydrogenation properties of Ti-Fe-Mn alloy with Cu and Y as additives," *International Journal of Hydrogen Energy*, vol. 42, no. 4, pp. 2229–2238, 2017.

[112] V. Bronca, P. Bergman, V. Ghaemmaghami, D. Khatamian, and F. Manchester, "Hydrogen absorption characteristics of an FeTi + misch metal alloy," *Journal of the Less Common Metals*, vol. 108, no. 2, pp. 313–325, 1985.

[113] T. Zhai, Z. Wei, Z. Yuan, Z. Han, D. Feng, H. Wang, and Y. Zhang, "Influences of la addition on the hydrogen storage performances of TiFe-base alloy," *Journal of Physics and Chemistry of Solids*, vol. 157, p. 110176, 2021.

[114] T. Bratanich, S. Solonin, and V. Skorokhod, "Hydrogen sorption peculiarities of mechanically activated intermetallic TiFe and TiFe-$MmNi_5$ ($LaNi_5$) mixtures," *International Journal of Hydrogen Energy*, vol. 21, no. 11-12, pp. 1049–1051, 1996.

[115] H. Zhang, M. Lu, and W. Li, "Activation of TiFe-$LaNi_5$ compound particles," *Acta Metallurgica Sinica (English Letters)*, vol. 10, no. 2, pp. 131–133, 1997.

[116] H. Shang, Y. Zhang, J. Gao, W. Zhang, X. Wei, Z. Yuan, and Y. Li, "Characteristics of electrochemical hydrogen storage using Ti–Fe based alloys prepared by ball milling," *International Journal of Hydrogen Energy*, vol. 47, no. 2, pp. 1036–1047, 2022.

[117] H. Shang, P. Sheng, J. Li, W. Zhang, X. Zhang, S. Guo, Y. Li, and Y. Zhang, "Characteristics of hydrogen storage of as-milled TiFe–based alloys," *International Journal of Hydrogen Energy*, 2023.

[118] Z. Han, T. Zhai, Z. Yuan, F. Liu, D. Feng, H. Sun, and Y. Zhang, "Characteristics of electrochemical hydrogen storage of TiFe based alloys with Ni composite by mechanical milling," *Materials Today Communications*, vol. 35, p. 105613, 2023.

[119] B. Singh, A. Singh, and O. Srivastava, "Improved hydrogen sorption characteristics in $FeTi_{1+\ x}Mm$ material," *International Journal of Hydrogen Energy*, vol. 21, no. 2, pp. 111–117, 1996.

[120] H. Suzuki, Y. Osumi, A. Kato, K. Oguro, and M. Nakane, "Hydrogen absorption-desorption characteristics of Ti-Co-Fe alloys," *Journal of the Less Common Metals*, vol. 80, no. 2, pp. 179–185, 1981.

[121] A. Guéguen and M. Latroche, "Influence of the addition of vanadium on the hydrogenation properties of the compounds $TiFe_{0.9}V_x$ and $TiFe_{0.8}Mn_{0.1}V_x$ ($x = 0$, 0.05 and 0.1)," *Journal of Alloys and Compounds*, vol. 509, no. 18, pp. 5562–5566, 2011.

[122] E. M. Dematteis, D. M. Dreistadt, G. Capurso, J. Jepsen, F. Cuevas, and M. Latroche, "Fundamental hydrogen storage properties of TiFe-alloy with partial substitution of Fe by Ti and Mn," *Journal of Alloys and Compounds*, vol. 874, p. 159925, 2021.

[123] A. Zeaiter, D. Chapelle, F. Cuevas, A. Maynadier, and M. Latroche, "Milling effect on the microstructural and hydrogenation properties of $TiFe_{0.9}Mn_{0.1}$ alloy," *Powder technology*, vol. 339, pp. 903–910, 2018.

[124] "Specifications of spex 8000m/8000d high-energy ball mill," https://www.spexsampleprep.com/8000M-mixermill, accessed on: 2021-11-30.

[125] M. S. El-Eskandarany, *Mechanical Alloying: Nanotechnology, Materials Science and Powder Metallurgy*. Elsevier, 2015.

[126] J. Huot and M. Tousignant, "Hydrogen sorption enhancement in cold-rolled and ball-milled $CaNi_5$," *Journal of Materials Science*, vol. 52, no. 20, pp. 11 911–11 918, 2017.

[127] "Interaction volume of electron beam," https://fakultaeten.hu-berlin.de/en/mnf/forschung_internationales/grs/salsa/p-a-labs/application-lab/instrumentation/a-labs-sem, accessed on: 2021-11-30.

[128] "Schematic of a scanning electron microscopy," https://fakultaeten.hu-berlin.de/en/mnf/forschung_internationales/grs/salsa/p-a-labs/application-lab/instrumentation/a-labs-sem, accessed on: 2021-12-30.

[129] R. Cheary, A. Coelho, and J. Cline, "Fundamental parameters line profile fitting in laboratory diffractometers," *Journal of Research of the National Institute of Standards and Technology*, vol. 109, no. 1, p. 1, 2004.

[130] C. Suryanarayana, "Mechanical alloying and milling," *Progress in Materials Science*, vol. 46, no. 1-2, pp. 1–184, 2001.

[131] X. Zhao, S. Han, X. Zhu, B. Liu, and Y. Liu, "Investigations on hydrogen storage properties of Mg_2Ni+x wt% $LaMg_2Ni$ (x = 0, 10, 20, 30) composites," *Journal of Solid State Chemistry*, vol. 190, pp. 68–72, 2012.

[132] X. Zhu, L. Pei, Z. Zhao, B. Liu, S. Han, and R. Wang, "The catalysis mechanism of La hydrides on hydrogen storage properties of MgH_2 in MgH_2 + x wt.% LaH_3 (x = 0, 10, 20, and 30) composites," *Journal of Alloys and Compounds*, vol. 577, pp. 64–69, 2013.

[133] D. Khatamian and F. Manchester, "The H-La (hydrogen-lanthanum) system," *Bulletin of Alloy Phase Diagrams*, vol. 11, no. 1, pp. 90–99, 1990.

[134] J. Huot, J. Pelletier, L. Lurio, M. Sutton, and R. Schulz, "Investigation of dehydrogenation mechanism of MgH_2–Nb nanocomposites," *Journal of Alloys and Compounds*, vol. 348, no. 1-2, pp. 319–324, 2003.

[135] J. Pelletier, J. Huot, M. Sutton, R. Schulz, A. Sandy, L. Lurio, and S. Mochrie, "Hydrogen desorption mechanism in MgH_2–Nb nanocomposites," *Physical review B*, vol. 63, no. 5, p. 052103, 2001.

[136] A. Yavari, J. De Castro, G. Vaughan, and G. Heunen, "Structural evolution and metastable phase detection in MgH_2–5% NbH nanocomposite during in-situ H-desorption in a synchrotron beam," *Journal of Alloys and Compounds*, vol. 353, no. 1-2, pp. 246–251, 2003.

[137] L. Zaluski, A. Zaluska, and J. Ström-Olsen, "Nanocrystalline metal hydrides," *Journal of Alloys and Compounds*, vol. 253-254, pp. 70–79, may 1997.

[138] A. Qajar, M. Peer, R. Rajagopalan, and H. C. Foley, "High pressure hydrogen adsorption apparatus: Design and error analysis," *International journal of hydrogen energy*, vol. 37, no. 11, pp. 9123–9136, 2012.

[139] V. K. Sharma and E. A. Kumar, "Measurement and analysis of reaction kinetics of La–based hydride pairs suitable for metal hydride–based cooling systems," *International Journal of Hydrogen Energy*, vol. 39, no. 33, pp. 19 156–19 168, 2014.

List of publications

List of publications included in the thesis

1. **M. M. Alam**, P. Sharma, J. Huot, "On the hydrogen storage properties of cast TiFe alloy mechanically milled with an intermetallic $LaNi_5$ and rare-earth elements La and Ce," Int J Hydrogen Energy 2023. `https://doi.org/10.1016/j.ijhydene.2023.08.100`.

2. **M. M. Alam**, P. Sharma, J. Huot, "Effect of addition of rare earth element La on the hydrogens torage properties of TiFe alloy synthesized by mechanical alloying," Int J Hydrogen Energy 2023. `https://doi.org/10.1016/j.ijhydene.2023.07.049`.

3. **M. Meraj Alam**, Pratibha Sharma, Jacques Huot, "On the hydrogen storage properties of mechanically alloyed TiFe milled with an intermetallic $LaNi_5$ and rare-earth elements La and Ce." (In process)

Other scholarly works not included in the thesis

1. Dharmendra K. Panchariya, **M. Meraj Alam**, Ankita Bishnoi, Pratibha Sharma, "Structural, first hydrogenation, and cyclability investigation of $Ti_{0.30}V_{0.30}Cr_{0.30}Zr_{0.05}Ni_{0.05}$ high entropy alloy." (In process)

2. Dharmendra K. Panchariya, **M. Meraj Alam**, Ankita Bishnoi, Pratibha Sharma, "Structural and hydrogen storage properties of high entropy alloy $Ti_{0.35}V_{0.30}Cr_{0.25}Zr_{0.05}Ni_{0.05}$." (An article originally presented at a conference has been extended an invitation for publication in the Int J Hydrogen Energy- **Submitted and is under review**)

3. Ankita Bishnoi, **M. Meraj Alam**, Pratibha Sharma, "Effect of AB_5-type intermetallic on the first hydrogenation properties of V-rich BCC solid-solution alloy." (An article originally presented at a conference has been extended an invitation for publication in the Int J Hydrogen Energy- **Submitted and is under review**)

Conference Presentations

1. **Md Meraj Alam**, Pratibha Sharma, Jacques Huot, "Effect of Addition of Lanthanum on the Hydrogen Storage Properties of TiFe alloy," *Canadian Association of Physicists Congress (CAP Congress-2018)*, Dalhousie University, Halifax, Nova Scotia, Canada, pp 125 (only abstract), June 11-15, 2018. (**Best Poster Presentation Award**)

2. **Md Meraj Alam**, Pratibha Sharma, Jacques Huot, "Effect of Addition of Ce on the Hydrogen Storage Properties of TiFe alloy," *Symposium Annuel de Chemie Inorganic du Québec (SACIQ-2018)*, Université du Québec à Trois-Rivières, Trois-Rivières, Québec, Canada, August 03, 2018. (**Best Poster**)

3. **Md Meraj Alam**, Pratibha Sharma, Jacques Huot, "Effect of Addition of Rare Earths on the Hydrogen Storage Properties of TiFe alloy," *Hydrogen-Metal Systems, Gordon Research Conference (GRC on MH-2019)*, Rey Don Jaime Grand Hotel, Avinguda de l'Hotel Castelldefels, Barcelona, Spain, June 30-July 05, 2019. (**Poster presentation**)

4. Pre-conference "International Workshop on Hydrogen Storage," under the aegis of DST-IIT Bombay Energy Storage Platform on Hydrogen, *7th International Conference on Advances in Energy Research (ICAER-2019)*, IIT Bombay, Mumbai, India, December 09-12, 2019. (**Organizing committee member of the workshop and volunteer in the conference**)

5. **M. Meraj Alam**, "The Scottish Government and International Association for Hydrogen Safety (IA HySafe) invite to attend the virtual conference as entrée gratuite," *International Conference on Hydrogen Safety (ICHS-2021)*, themed on "Safe Hydrogen for Net Zero," **Edinburgh, Scotland**, 21-24 December 2021. (**Attendee**)

6. Ankita Bishnoi, **M. Meraj Alam**, Pratibha Sharma, "Effect of AB_5-type intermetallic on the first hydrogenation properties of V-rich BCC solid-solution alloy," *7th International Hydrogen Technologies Congress (IHTEC-2023)*, Firat University, Elazığ, Türkiye, May 10-12, 2023. (**Oral presentation**)

7. Dharmendra K. Panchariya, **M. Meraj Alam**, Ankita Bishnoi, Pratibha Sharma, "Structural and hydrogen storage properties of high entropy alloy $Ti_{0.35}V_{0.30}Cr_{0.25}Zr_{0.05}Ni_{0.05}$, *7th International Hydrogen Technologies Congress (IHTEC-2023)*, Firat University, Elazığ, Türkiye, May 10-12, 2023. (**Oral presentation**)

Author's Biography

Md Meraj Alam is a cotutelle PhD candidate in energy and material sciences leading to a joint doctorate from IIT Bombay (India) and Université du Québec à Trois-Rivières (UQTR, Canada). The cotutelle obligates fulfilling the courses and credits requirement of both the IIT Bombay and the UQTR with a single thesis. As part of the cotutelle obligation he spent a year and half as a Queen Elizabeth Scholar at UQTR with a Canadian Queen Elizabeth II Diamond Jubilee Scholarship and had the opportunity to work at the hydrogen research institute (IRH). His academic focus, rooted in mechanical engineering, centers on sustainable processes, nanomaterials, and solid-gas interactions particularly in hydrogen storage. Proficient in advanced characterization techniques, he excels in designing and analyzing new materials as an experimentalist. His core strengths lie in fault identification, troubleshooting and quality control management.

Education

Doctor of Philosophy (PhD), Dissertation title: Effect of adding the intermetallic $LaNi_5$ and rare earth elements La and Ce on the hydrogen storage properties of TiFe alloy.
Master of Technology (M.Tech), Mechanical Engineering, Aligarh Muslim University, Aligarh, India (CPI: 9.313/10) (1^{st} Rank- University medal).
Bachelor of Technology (B.Tech), Mechanical Engineering, Aligarh Muslim University, Aligarh, India (CPI: 8.214/10).
Email: `md.meraj.alam@uqtr.ca`

Awards & Honours

Bourses d'excellence à l'admission– Scholarship of excellence among newly admitted students of the program Doctorate in Energy and Materials Sciences (1732) at Université du Québec à Trois-Rivières for the session 2017-2018. **A certificate and a cash prize of C$ 7000 (approx. 3.5 lac INR)**.